Improvement of Mechanical Properties of Polymeric Composites

Benjamin H. Rutz

A dissertation

submitted in partial fulfillment of the

requirements for the degree of

Doctor of Philosophy

University of Washington

2014

Reading Committee:

John Berg, Chair

Brian Hayes

Felix Nguyen

Program Authorized to Offer Degree:

Department of Chemical Engineering

University of Washington

Abstract

Improvement of Mechanical Properties of Polymeric Composites

Benjamin H. Rutz

Chair of the Supervisory Committee:
Professor John C. Berg
Department of Chemical Engineering

The use of reinforced polymer-matrix composite materials is growing rapidly. Their low weight, high strength and stiffness and resistance to corrosion make them particularly well suited for aerospace applications. The next generation of aircraft, including the Boeing 787 and the Airbus A350, are made largely out of continuous fiber reinforced plastics, reducing fuel consumption and improving range. The continued growth of the market is dependent not only on improving manufacturability and reducing cost, but also on the continuous improvement of material properties, necessitating the development of new materials and an improved understanding of the chemistry and mechanics of composites. Composite properties are dependent on many factors including the properties of the constituent phases, their relative volume fraction, their spatial orientation and arrangement, and the adhesion between them. It is recognized that good composite mechanical properties are dependent on a strong and tough adhesive bond between the polymer and the reinforcement, necessitating the development of novel techniques to improve the adhesion. Additionally, with the weight sensitive applications

of polymeric composites, a reduction in the material weight, without adversely affecting mechanical properties, is desired.

In the current study, the adhesion in both continuous fiber and particulate reinforced plastics is investigated, as is the synthesis of a nano-void lightened resin. More specifically, the applied stress necessary to cause adhesive failure in a particulate composite, as a function of interparticle separation and surface functionalization is determined with *in situ* transmitted light optical microscopy. A simple model is developed for the system, based on the superposition of stress concentrations, determined with an analytical solution, and a critical local tensile stress failure criterion. For continuous fiber reinforced plastics, the use of electrostatically deposited poly(ethyleneimine) functionalized silica nanoparticles as a means to improve the interfacial shear strength is investigated. The use of these topological surface modifiers, in contrast to the typical chemical modification of the interface, provides an increase in surface area and mechanical interlock, improving the adhesion, as measured by the single fiber fragmentation test. The particle size is optimized, as very small particles, <26 nm, do not appreciably increase the surface roughness, while large particles, ≥ 71 nm, are too large, and do not improve the adhesion.

A method for reducing the density of a thermosetting resin is discussed. From a literature review, it is established that the most promising means for the incorporation of nano-voids into a thermoset is with *blowing agent wells*, self-assembled block copolymer micelles that solubilize blowing agent. A number of potential block copolymers are studied, and blowing agent wells are successfully made with the commercially available block copolymer epoxy-toughener Dow Fortegra®, which are used to solubilize heptane. The method for controlled vaporization of the blowing agent to make a low density material is still under development.

Table of Contents

LIST OF FIGURES

LIST OF TABLES

Acknowledgements

First and foremost, I would like to thank Professor John Berg for all he has done. His guidance, instruction, and patience were invaluable.

I would also like to thank the undergraduate researchers that I had the pleasure of working with over the years, Melissa Dao, Eric Ravet, Joseph Crowell, and Danny Bauer. The other members of the Berg research group, Dr. Saran Poovarodom, Dr. Prasad Bhosale, Matt Gacek, Ed Michor, and Kyle Caldwell, who have all contributed significantly to my research. I would also like to thank Jeff Richards, Dr. Felix Nguyen, and Dr. Brian Hayes for many insightful conversations and help with innumerable technical challenges. Arne Biermans was incredibly helpful with the fabrication and repair of many instruments and apparatus.

Lastly, I would like to thank Toray Composites (America) for financial support.

Chapter 1 – Introduction

1.1 Research motivation

A composite is any material made with two or more constituents with distinct properties, creating a material with properties significantly different from those constituent phases. This definition encompasses a large number of diverse materials including concrete, engineered wood products (e.g. oriented strand board), metal matrix composites, ceramic matrix composites and many others. One of the most important and fastest growing types is polymer matrix composites which consist of a polymeric continuous phase and a second phase of short fibers, platelets, nano-tubes, nano-wires or most notably, continuous fibers to give continuous fiber reinforced plastics (CFRPs). Polymeric composites can have very high strength and stiffness while maintaining low weight, making them desirable materials for a number of applications, but are hindered by economic and manufacturing considerations and some material properties in certain applications, including brittle failure and poor electrical conductivity. CFRPs were previously only utilized on military aircraft, small structures on civilian aircraft and other specialized applications but they are pushing into new markets such as sporting goods (e.g. bikes and tennis rackets), the automotive industry (e.g. BWM i3 and i8) and are seeing significantly increased utilization in the next generation of civilian aircraft, including the Boeing 787 and Airbus A350. The widespread utilization for relatively low performance applications, namely automotive, is dependent on cost and manufacturability, but the continuous advancement demanded by high performance applications necessitates improvements in material properties.

The properties of polymeric composites depend on many factors, including the properties of both the polymer and the reinforcements, the volume fraction of the reinforcements and their

geometric shape and arrangement relative to the stresses to which the composite is exposed. The polymer, or resin, itself may consist of multiple phases, as when gas inclusions are present for purposes of reducing weight or when rubbery inclusions are present to improve fracture toughness [1,2]. Beyond this, composite properties depend critically on the level and nature of the adhesion between the reinforcement surfaces and the bulk polymer because it is through this agency that stresses are transmitted to the reinforcements [3,4]. Practical adhesion requires intimate contact between the adhesive (the polymer) and the adherend (reinforcement surface), and is believed to occur via one or a combination of mechanisms. What is termed "contact adhesion" results from the direct molecular interaction between molecules in the adhesive and adherend across a molecularly sharp interface between them, including van der Waals and acid-base effects. Molecular inter-diffusion and entanglements provide a second mechanism, while mechanical interlock provides a third. Electrostatic interactions are generally believed to be negligible.

More often than not, a single clearly defined two dimensional molecular interface between resin and reinforcement cannot be identified, and instead, a finite interlayer or *interphase* is created, often with a thickness from a few nanometers to a few microns. The composition and properties of the interphase vary across its thickness [5].

The mechanical performance of a composite material is also dependent on the nature of mechanical forces on both a macro and micro level. In a CFRP structure a large volume fraction of fibers are typically made to be aligned in the direction of anticipated load. When a tensile stress is applied to a CFRP in the direction of the fibers a shear stress develops at the fiber-matrix interface, due to the miss-match of the *Young's modulus*, or tensile stiffness, of the fiber and matrix. This necessitates good interfacial shear strength (IFSS), which is dependent on the

properties of the interphase. In addition to shear stress, the interphase may experience tensile stress if the composite is subject to transverse tensile load, or compressive stress from applied loads, or from residual thermal stress, cure shrinkage and the *Poisson effect*, the phenomenon where a material subjected to tensile stress in one direction tends to contract in the other directions.

To achieve a good IFSS, and good mechanical properties in a CFRP, the interphase must meet a number of criteria. First, the interphase must be in contact adhesion with the fibers which necessitates good wetting of the fiber by the resin, that is, the contact angle of the liquid resin on the fiber surface must be near zero. The surfaces of carbon fibers are often oxidized [6], increasing the number of surface functional groups, increasing the surface energy, reducing the contact angle and promoting wetting [7]. Oxidative surface treatments can be either wet processes where the fiber is treated with solutions of nitric acid, hydrogen peroxide, and potassium persulfate, for example, or with electrochemical oxidation in aqueous systems or dry processes such as plasma oxidation where a low pressure gas such as air, O_2 or CO_2 are exposed to high voltage AC or DC potentials, radio frequency radiation or microwave radiation generating ions and free radicals that can functionalize, and etch, the fiber surface. Depending on the oxidative medium, various surface chemistries can be introduced, such as hydroxyl, carboxyl, carbonyl, and phenolic functional groups [8]. These reactive groups may covalently bond to the resin, promoting good molecular interaction and thus adhesion [9].

Covalent bonding between glass fibers and the matrix is improved with coupling agents, often silanes [10–12], which are typically comprised of a tetra-functional organosilane with hydrolysable alkoxy groups that can covalently bond with the hydroxyl groups on the fiber surface via a condensation reaction and an organic group with amino or epoxy functionality that

can covalently bond with the resin. Silane coupling agents can become partially cross-linked at the fiber surface, with sufficient free volume to permit the inter-diffusion of the resin and silane, affording another adhesion mechanism [13].

Depending on the aggressiveness of oxidative surface treatment on carbon fibers, the outer layers can be removed, increasing the fiber surface roughness and surface area [14]. This can provide an increase in adhesion via mechanical interlock. However, excessive oxidative treatments can significantly reduce the fiber diameter [6]. Glass fibers are typically smoother, and oxidative surface treatments do not increase the surface roughness as the fiber chemistry is more homogeneous. Recently, and in the work presented here, researchers have been working to improve the surface roughness of glass and carbon fibers with the deposition or growth topological interfacial surface modifiers such as whiskers [15–17], nanotubes [5,18–20] and nanoparticles [21–23], increasing the fiber surface roughness and surface area. These methods can increase the surface roughness beyond what is achievable with oxidation of carbon fibers. By increasing the surface area, there is more opportunity for adhesion mechanism such as covalent bonding and inter-diffusion to take place on a per unit length of fiber basis. The mechanical interlock provides an additional mechanism of adhesion, not found of smooth fibers, improving the interfacial adhesion. These topological modifiers can also improve the friction between the fiber and matrix, an important attribute if adhesion is otherwise poor and for increasing the composite toughness. Fiber bridging occurs if a crack propagates transverse to the fiber direction through the matrix, without causing the fibers to fail. As the crack opens behind the crack tip the fibers pull out, and the energy necessary to cause the crack to propagate is partially dependent on the friction between the fiber and matrix. This toughening mechanism is typically seen in ceramic-ceramic composites with weak interfaces [24].

The interphase should theoretically have a relatively high modulus, between that of the bulk polymer and the fiber. This would generate a *graded modulus* where there is a gradual transition from the stiff fiber to soft matrix, preventing modulus discontinuities that lead to shear stress concentrations and subsequent premature failure of the interphase . A graded modulus also maximizes the transfer of stress to the fiber [25,26]. However, increasing the modulus of the interphase can reduce the fracture toughness. In practice, to maximize the fracture toughness and impact resistance of a composite, the interphase modulus is optimized to balance strength and toughness. Ideally, the interphase would have good fracture toughness and a high modulus, a common goal in material science.

With continuing consideration of the above example, a unidirectional CFRP in tension, the matrix serves to protect to fibers from environmental damage, and transfers stress to the fibers, but does not carry the majority of the stress. Thus, in many applications, the volume fraction of fibers is maximized. However, there is an upper limit, typically around 60 vol% fibers to maximize properties [27]. When the volume fraction is increased further, the fiber tows are not saturated with the resin, leaving dry fibers in the interior of the tow that do not carry any significant load, and act as stress concentrators. If nano-sized voids were incorporated into the resin, it would be possible to reduce the resin volume fraction, while still maintaining intimate contact between the fiber and resin. In other words, it may be possible to incorporate voids or gas filled bubbles that are small enough so they do not interfere with the fiber-matrix interaction, generating a lightweight, effectively homogeneous resin. It is postulated that reducing the density of a resin with nano-voids would lead to a decrease in the absolute strength and stiffness, as there is less material to carry load, but the *specific*, or per unit mass, strength and stiffness would remain constant. The material may have an increased fracture toughness, K_{IC}, the ability

for a material to resist the growth of a crack, and an increased energy release rate, $G_{IC,}$ the energy dissipated during fracture [28]. An increase in matrix fracture toughness would be beneficial to CFRP material properties.

In a particulate composite, much like in a CFRP, the local microscopic stresses can be very different from the applied macroscopic stresses. Again, thermal stress, cure shrinkage, and the Poisson effect influence internal stress fields, as does the proximity of the particulates to each other. If the local tensile stress reaches a sufficient level, micro-damage may occur, in the case of relatively large particulates (> 1 μm) embedded in an elastomeric matrix debonding is a common failure mechanism [29]. From a structures design standpoint, it is important to know how the overlap of interparticle stress fields influence these micro-damage events, and how to improve adhesion, to limit damage and increase the material properties. Often, local internal stresses of complicated materials such as particulate composites are determined with finite element analysis (FEA). This technique, though very useful, tends to be very computationally expensive.

1.2 Research objectives

The field of reinforced polymer matrix composites is broad and multifaceted, offering many opportunities for improvement in understanding and material properties, a notion that is reflected in the work presented here. The work is focused on adhesion, albeit in two very different systems. First, a particulate composite, subjected to tensile stress is considered. As the stress level is increased an increasing number of particulates undergo adhesive failure with the matrix. A number of factors control the adhesive failure including applied stress, the stress concentration caused by neighboring particles, and the strength of the adhesive bond and are addressed here. A simple, semi-predictive computer model is developed for estimating for the

level of debonding, as a function of applied stress. The model assumes a critical local stress required to cause debonding, which is determined experimentally, then calculates the stress concentration at potential debonding locations by superimposing the stress fields from all neighboring particles. The use of an analytical solution for the stress concentration around a sphere significantly reduces the computational expense when compared to FEA.

The interfacial adhesion between a continuous fiber and a continuous thermosetting resin subjected to shear force is also considered, with the focus on improving the stress transfer across the interface. This is done by electrostatically depositing poly(ethyleneimine) functionalized silica nanoparticles on to the fiber surface to increase the surface area and mechanical interlock and potentially increasing the toughness and modulus of the interphase. The efficacy of nanoparticles on the interface at increasing the interfacial shear strength is determined with the single fiber fragmentation test. Various particle sizes and functionalities are explored.

The second major objective of this investigation is on producing low density thermosetting resins using nano-voids made with *blowing agent wells*, which are micelle-like self-assembled nano-structures made of block copolymers with a resin miscible segment and a resin immiscible segment which can solubilize blowing agents. This objective is comprised of three sequential goals: first, the generation and characterization of the blowing agent wells, second, the incorporation of a blowing agent into the interior, and third, generating a gas from the solubilized blowing agent with careful control of the visco-elastic properties of the resin, to prevent coalescence.

1.3 Document layout

Chapter 2 investigates the effect of interparticle stress concentrations, applied stress, and surface chemistry on the level of debonding in a particulate composite made with 650 μm glass beads with a poly(vinyl butyral) (PVB) matrix. Additionally, a semi-predictive computer model was developed based on the superposition of the stress fields of a single particle case.

Chapter 3 discusses the methods and technologies currently available for the generation of a nano-void lightened thermoset with a summary of a review paper written on the subject, including a discussion on homogeneous gas nucleation and the formation of block copolymer micelles in thermosets. The current work on the creation of micelles in thermosets, as well as the incorporation of possible blowing agents is discussed.

Chapter 4 explores the use of poly(ethyleneimine) functionalized silica nanoparticles electrostatically deposited on to the surface of E-glass fibers, in order to increase the interfacial shear strength (IFSS) as measured by the single fiber fragmentation method (SFFT). The pH and ionic strength of the aqueous suspensions were controlled to achieve optimal surface coverage. A short summary of the advantages and disadvantages of common micromechanical interfacial adhesion testing procedures is also presented.

Chapter 5 provides conclusions and recommendations for the work presented in Chapters 2-4.

Appendix A provides the computer code, written for Matlab used to model the debonding in particulate composites. Appendix B discusses seven other methods used in an attempt to improve the IFSS using particles deposited on fiber interfaces.

References

[1] Hsieh TH, Kinloch AJ, Masania K, Sohn Lee J, Taylor AC, Sprenger S. The toughness of epoxy polymers and fibre composites modified with rubber microparticles and silica nanoparticles. J Mater Sci 2009;45:1193–210.

[2] Nguyen FN, Berg JC. Novel core-shell (dendrimer) epoxy tougheners: Processing and hot-wet performance. Compos Part -Appl Sci Manuf 2008;39:1007–11.

[3] Weitzsacker CL, Xie M, Drzal LT. Using XPS to investigate fiber matrix chemical interactions in carbon-fiber-reinforced composites. Surf Interface Anal 1997;25:53–63.

[4] Drzal LT, Rich MJ, Camping JD, Park WJ. Interfacial shear strength and failure mechanisms in graphite fiber composites, 1980, p. 20C.

[5] Drzal LT. The role of the fiber-matrix interphase on composite properties. Vacuum 1990;41:1615–8.

[6] Chand S. Review carbon fibers for composites. J Mater Sci 2000;35:1303–13.

[7] Hoecker F, Karger-Kocsis J. Surface energetics of carbon fibers and its effects on the mechanical performance of CF/EP composites. J Appl Polym Sci 1996;59:139–53.

[8] Bradley RH, Ling X, Sutherland I. An investigation of carbon fibre surface chemistry and reactivity based on XPS and surface free energy. Carbon 1993;31:1115–20.

[9] Kim J-K, Mai YW. Engineered interfaces in fiber reinforced composites. Amsterdam; New York: Elsevier Sciences; 1998.

[10] Plueddemann EP. Silane Coupling Agents. Springer; 1982.

[11] Harding PH, Berg JC. The adhesion promotion mechanism of organofunctional silanes. J Appl Polym Sci 1998;67:1025–33.

[12] Miller AC, Berg JC. Unexpected behavior between polystyrene and untreated and silane-treated glass beads in filled polymeric composites. J Appl Polym Sci 2003;89:521–6.

[13] Miller AC, Berg JC. Effect of silane coupling agent adsorbate structure on adhesion performance with a polymeric matrix. Compos Part -Appl Sci Manuf 2003;34:327–32.

[14] Marshall P, Price J. Topography of carbon fibre surfaces. Composites 1991;22:388–93.

[15] Lin Y, Ehlert G, Sodano HA. Increased Interface Strength in Carbon Fiber Composites through a ZnO Nanowire Interphase. Adv Funct Mater 2009;19:2654–60.

[16] Galan U, Lin Y, Ehlert GJ, Sodano HA. Effect of ZnO nanowire morphology on the interfacial strength of nanowire coated carbon fibers. Compos Sci Technol 2011;71:946–54.

[17] Ehlert GJ, Sodano HA. Zinc Oxide Nanowire Interphase for Enhanced Interfacial Strength in Lightweight Polymer Fiber Composites. Acs Appl Mater Interfaces 2009;1:1827–33.

[18] Thostenson ET, Li WZ, Wang DZ, Ren ZF, Chou TW. Carbon nanotube/carbon fiber hybrid multiscale composites. J Appl Phys 2002;91:6034–7.

[19] Zhao ZG, Ci LJ, Cheng HM, Bai JB. The growth of multi-walled carbon nanotubes with different morphologies on carbon fibers. Carbon 2005;43:663–5.

[20] Zhang F-H, Wang R-G, He X-D, Wang C, Ren L-N. Interfacial shearing strength and reinforcing mechanisms of an epoxy composite reinforced using a carbon nanotube/carbon fiber hybrid. J Mater Sci 2009;44:3574–7.

[21] Gao X, Jensen RE, Li W, Deitzel J, McKnight SH, Gillespie JW. Effect of fiber surface texture created from silane blends on the strength and energy absorption of the glass fiber/epoxy interphase. J Compos Mater 2008;42:513–34.

[22] Gao X, Jensen RE, McKnight SH, Gillespie JW. Effect of colloidal silica on the strength and energy absorption of glass fiber/epoxy interphases. Compos Part -Appl Sci Manuf 2011;42:1738–47.
[23] Leonard GC, Hosseinpour D, Berg JC. Modulus-Graded Interphase Modifiers in E-Glass Fiber/Thermoplastic Composites. J Adhes Sci Technol 2009;23:2031–46.
[24] Anderson TL. Fracture mechanics: fundamentals and applications. Boca Raton, FL: Taylor & Francis; 2005.
[25] Ho H, Drzal LT. Non-linear numerical study of the single-fiber fragmentation test. Part I: Test mechanics. Compos Eng 1995;5:1231–44.
[26] Ho H, Drzal LT. Non-linear numerical study of the single-fiber fragmentation test. Part II: A parametric study. Compos Eng 1995;5:1245–59.
[27] Ramanathan T, Muthumanickam MA, Subramanian K. Study on the effect of loading rate on flexural strength of glass/polyester composites as a function of span-to-depth ratio and fiber volume fraction. Mater Manuf Process 2000;15:845–52.
[28] Huang Y, Kinloch AJ. The toughness of epoxy polymers containing microvoids. Polymer 1992;33:1330–2.
[29] Gent AN. Detachment of an elastic matrix from a rigid spherical inclusion. J Mater Sci 1980;15:2884–8.

Chapter 2 – Debonding in particulate composites

cf. Rutz B.H., and Berg J.C., "The Effect of Interparticle Stresses on Debonding in Spherical Silica Particle-Filled Composites with a Poly(vinyl butyral) Matrix," *Journal of Adhesion Science and Technology*. **25**, 2629-2640 (2011).

Summary

Particulate composites are surprisingly prevalent, mainly in the form of metal matrix composites with ceramic particulates used to improve wear characteristics and as polymer matrix particulate composites, found in consumer products for their increased rigidity, compared to the virgin polymer. A common failure mechanism is debonding of the matrix from the particulate, which depends on the material properties of both phases, the adhesion between the phases, mode of loading, and the volume fraction of the particulates. Increasing the volume fraction of particulates decreases the interparticle separation, leading to higher stress concentration, causing debonding, or other failure modes, at relatively low applied stresses. The goal of this work was to investigate the influence of particle volume fraction and adhesion on debonding in particulate composites, which may lead to the manufacture of particulate composites with better mechanical properties.

The effect of varying the volume fraction on the level of particle-matrix debonding at a given applied tensile stress was studied using a model system of 650 μm soda-lime glass spherical particles in a poly(vinyl butyral) (PVB) matrix was investigated. The effect of improving the adhesion was studied by modifying the particles with the adhesion promoter 3-aminopropyltriethoxysilane (APS). The volume fraction of particles was varied from 1 to 15 vol% to change the average interparticle distance. The use of an adhesion promoter increased

the maximum stress required to cause debonding, but had no effect on the interparticle stress fields, so the same trends, at higher applied stress, were observed. A model was developed to predict the observed behavior, based on Goodier's analytical solution for the stress concentration developed by a single sphere in an infinite matrix and the superposition of these calculate stress concentrations. The model, although quite simple, showed good agreement with the experimental results for the dependence of the particle-matrix debonding behavior on the volume fraction of beads.

2.1 Introduction

High modulus fillers, such as mineral oxides, are often added to plastics to improve stiffness and fire retardance, among other properties, generally at the expense of ultimate and fatigue strength [1]. This reduction in strength, especially in tensile and flexural loading, is caused by the filler particles acting as stress concentrators, and if the adhesion is poor they debond at stresses well below the strength of the continuous phase. As the filler volume fraction is increased, the average interparticle spacing is decreased, leading to a superposition of the stress fields, greatly increasing the local stresses. These elevated local stresses lead to microscopic failure, in the form of particle-matrix debonding [2–5], cracking [6], yield [7], and cavitation [5] at applied stresses lower than observed for single particle cases. This reduction in strength isn't necessarily critical; many materials made with particulate fillers are used in applications where low mechanical strength is permissible. However, knowing the relationship between filler fraction and microscopic damage at a given applied stress would be very useful in the design of structures made with particulate composites.

Generally, three methods are used when investigating failure modes in particulate composites: one, sufficient load is applied to cause the specimen to break followed by

microscopy of the fracture surface, two, by using a microphone to detect acoustic emissions of failure events while load is applied to the specimen, or three, if the sample is transparent, by *in situ* optical microscopy while load is applied to the specimen. *Ex situ* microscopy can often permit inference of pre-critical failure modes and toughening mechanisms, and if techniques such as scanning electron microscopy (SEM) are used, information on the nano-scale can be obtained [8], but it is inherently limited, as it provides information on only one temporal point. Acoustic emissions are generated in particulate composites subjected to increasing loads as the particulates debond and/or the matrix cracks. These emissions can then be correlated to the applied stress, to determine the strength of the matrix/particulate bond [9–11]. Although this technique has been used successfully, correlating specific acoustic emissions to the corresponding micro-failure events is difficult because of acoustic reflection in the sample, signal variation for one type of event and overlapping signals from nearly simultaneous events [3,10]. Using *in situ* optical microscopy allows for continuous observation as the applied load is increased, without the need to deconvelute a complicated acoustic signal. The major limitations are resolution, using visible light the minimum resolution is about 500 nm, and the need for optically transparent materials.

In the current study, the level of debonding between 650 μm glass particles and poly(vinyl butyral) (PVB) was determined as a function of applied tensile stress, filler volume fraction and surface functionalization. As the filler volume fraction is increased, the average interparticle spacing is decreased, leading to overlap of the stress concentration fields surrounding the particles. This leads to elevated local stress, causing the particles to debond at comparatively low applied stress. This phenomenon was modeled by generating a virtual composite, calculating the stress concentration around each virtual particle using the analytical

solution for a sphere in an infinite matrix, superimposing the stress concentrations to determine the local stress at the pole of each particle, then assuming a normal stress at the pole is the failure criterion, the level of debonding at a given applied stress was determined for the model system.

2.2 Methods

2.2.1 Sample preparation

The particulates used were 650 μm diameter smooth soda-lime glass spheres (Cataphote Inc., Jackson, MS), which were washed in NoChromix glass cleaner (Godax Laboratories, Cabin John, MD) and sulfuric acid, then rinsed with deionized water (DI H_2O) until the rinse was pH neutral, and dried at 150°C for 24 hours. One system type consisted of beads with clean, untreated surfaces, another system used beads treated with 0.5 vol% 3-aminopropyltriethoxysilane (APS) (Gelest Inc., Morrisville, PA) in deionized water for 90 min. The chemical structure of APS is given in Fig. 2.1. The polymer matrix in all cases was poly(vinyl butyral) (PVB), (Mowital B60H, Kuraray America, Houston, TX). PVB is a copolymer consisting mainly of vinyl butyral groups with varying proportions of vinyl alcohol groups and residual vinyl acetate groups, the chemical structure is given in Fig. 2.2. Properties of the grade of PVB used are given in Table 2.1 [12,13]. PVB has very good optical properties and is elastomeric. An elastomer was used because high strain to plastic yield was necessary to ensure that debonding was the sole initial failure mechanism.

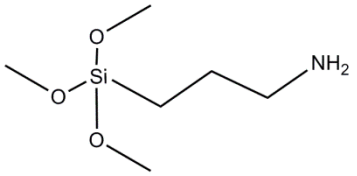

Figure 2.1. The structure of aminopropyltriethoxysilane (APS)

To prepare the test specimens, the glass beads and powdered PVB were dry mixed in the appropriate ratios and poured into a 15 cm diameter circular steel mold. The mold was then placed into a Tetrahedron MTS-14 automated hot press (Tetrahedron Associates, Inc., San Diego, CA) and heated to 115°C under 1.5 MPa pressure for 10 min. The temperature was reduced to 75°C and held for another 10 min, after which the pressure was released and the mold was allowed to cool to room temperature. From the sample disks, rectangular specimens, with a length, width and thickness of 75 mm, 10 mm, and 3 mm respectively, were cut with a laser cutter (Universal Laser System, Scottsdale, AZ). The laser did not cut through the glass beads, so the cut was finished with a hand saw, and finally the edges were sanded with progressively finer sandpaper, to ensure a smooth finish.

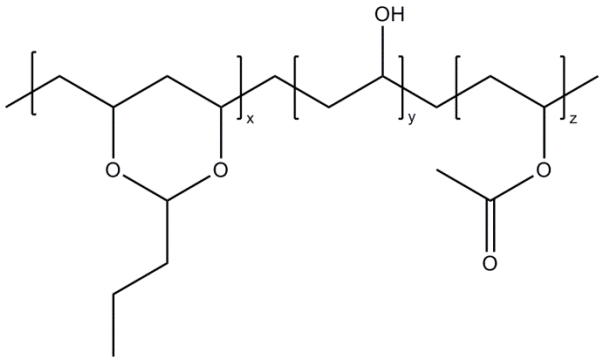

Figure 2.2. The structure of commercially produced PVB a ternary copolymer of vinyl butyral (the *x* segment), vinyl alcohol (the *y* segment), and vinyl acetate (the *z* segment)

Table 2.1. Properties of Mowital B60H PVB

VOH (wt%)	VAc (wt%)	Tg (°C)	Purity (%)	Avg. MW (g/mol)	Young's Modulus (MPa)	Bulk Modulus (GPa)	Poisson's Ratio
18.8	1.6	70	98.9	90,000	2.0	0.714	0.4

2.2.2 Mechanical Testing

The samples were subjected to a constant tensile displacement rate of 1 mm/min until the sample yielded plastically in a Satec T-1000 mechanical tester (Satec Systems, Grove City, PA). The specimens were video recorded using a CCD camera (4915-2000 Series High-Performance Monochrome CCD, Coho, San Diego, CA) with a macroscope, (Wild Makroskop M420, Wild Heerbrugg, Heerbrugg, Switzerland). This experimental setup is shown in Fig. 2.3. When a debonding event occurred, the video time stamp was noted, and used to determine the applied stress from the time stamp on the stress and strain data generated from the Satec mechanical tester. A still taken from the video captured during testing of a 10 vol% glass bead specimen is shown in Fig. 2.4. The black caps on some glass beads are the debonded regions. To normalize for variations between similarly prepared specimens and varying volume fraction of beads, the number of debonding events was divided by the total number of *possible* debonding events, taken to be the number of hemispheres visible in the video for the entirety of the test, giving the *fraction debonded*.

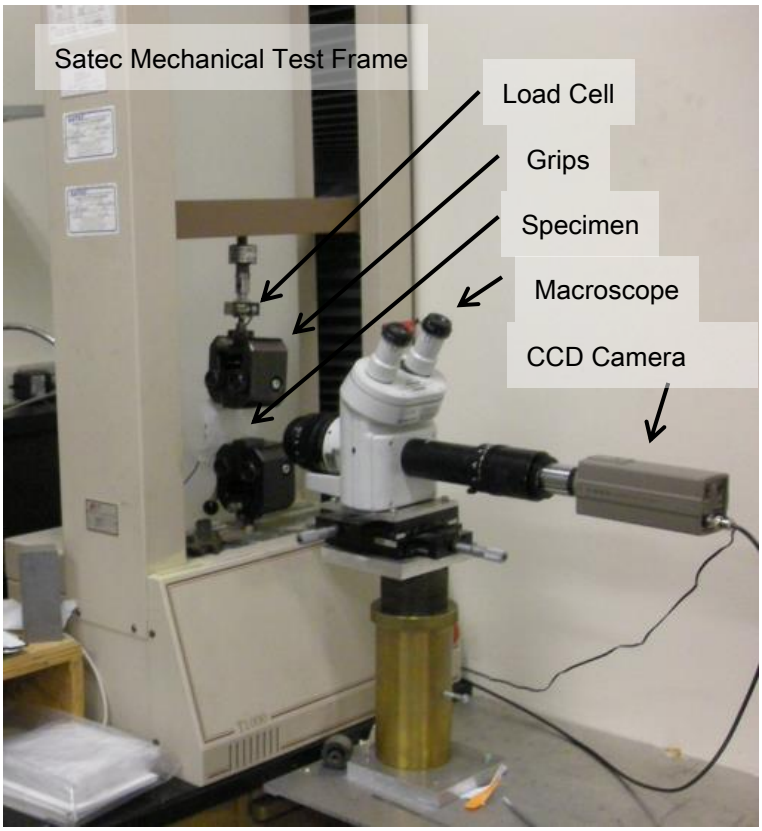

Figure 2.3. A photograph of the experimental setup for applying tensile stress to the specimens, while observing with a "macroscope" *in situ*

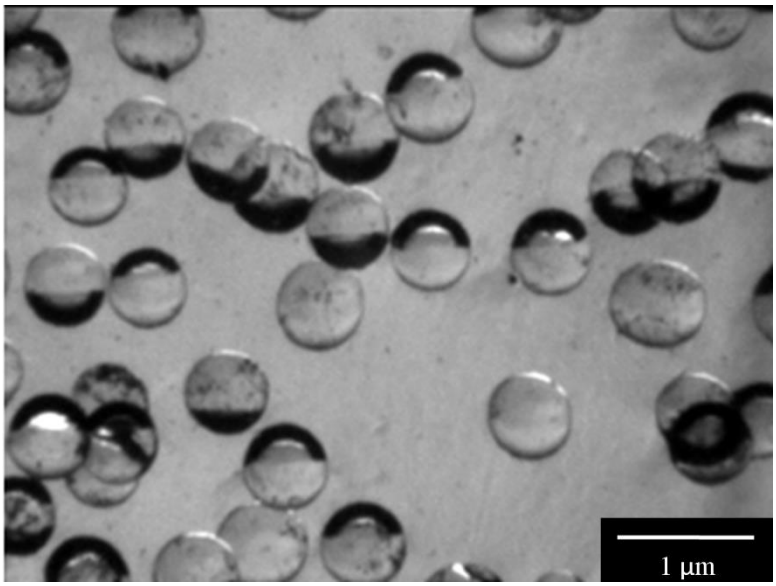

Figure 2.4. A bright field micrograph of a 10 vol% particulate composite subject to tensile strain, showing debonded regions on some particulates and the random spatial distribution

2.2.3 Modeling

The model was implemented with Matlab (Mathworks Inc, Natick, MA), first by generating a virtual composite by defining a "specimen" with dimensions equal to the real specimens tested. The virtual particulates were placed randomly within the bounds of the specimen, and were checked for overlap with already placed particulates. If there was overlap, the particulate was deleted and placed in another random location. The location of each pole, that is, the point on the particulate with its normal in the direction of applied stress, was determined, then using Goodier's solution for the stress concentration around a sphere [14], the stress concentration in the direction of applied stress from every neighboring particulate was calculated and summed, thus giving the total stress concentration at a pole. This was repeated for each pole in the virtual composite.

Goodier's solution in spherical coordinates for displacement around a sphere in a continuous isotropic matrix is given in Eqn. 2.1 – 2.2 and the stresses, are given in Eqn. 2.3-2.6 where *u* is displacement, *r* is distance from the center of the inclusion, *v* is Poisson's ratio, *E* is Young's modulus, *a* is the radius of the inclusion, *T* is the applied stress, the subscript *1* and *2* refers to the matrix and inclusion properties, respectively. The spherical coordinate system is defined in Fig. 2.5a.

$$u_r = -\frac{A}{r^2} - \frac{3B}{r^4} + \left(\frac{5-4\nu}{1-2\nu}\frac{C}{r^2} - 9\frac{B}{r^4}\right)\cos 2\theta \tag{2.1}$$

$$u_\theta = -\left(\frac{2C}{r^2} + 6\frac{B}{r^4}\right)\sin 2\theta \tag{2.2}$$

$$\sigma_{rr} = 2E\left[\frac{2A}{r^3} - \frac{2\nu}{1-2\nu}\frac{C}{r^3} + 12\frac{B}{r^5} + \left(\frac{2(5-\nu)}{1-2\nu}\frac{C}{r^3} + 36\frac{B}{r^5}\right)\cos 2\theta\right] \tag{2.3}$$

$$\sigma_{\theta\theta} = 2E\left[-\frac{A}{r^3} - \frac{2\nu}{1-2\nu}\frac{C}{r^3} - 3\frac{B}{r^5} + \left(\frac{C}{r^3} - 21\frac{B}{r^5}\right)\cos 2\theta\right] \tag{2.4}$$

$$\sigma_{\psi\psi} = 2E\left[-\frac{A}{r^3} - \frac{2(1-\nu)}{1-2\nu}\frac{C}{r^3} - 9\frac{B}{r^5} + \left(\frac{C}{r^3} - 15\frac{B}{r^5}\right)\cos 2\theta\right] \quad (2.5)$$

$$\sigma_{r\theta} = 2E\left[-\frac{2(1+\nu)}{1-2\nu}\frac{C}{r^3} + 24\frac{B}{r^5}\right]\sin 2\theta \quad (2.6)$$

Where:

$$A = a^3\left[\begin{array}{c} -\frac{T}{8E_1}\frac{E_1-E_2}{(7-5\nu_1)E_1+(8-10\nu_1)E_2} \times \\ \frac{2E_1(1-2\nu_2)(6-5\nu_1)+E_2(3+19\nu_2-20\nu_1\nu_2)}{2E_1(1-2\nu_2)+E_2(1+\nu_2)} + \frac{T}{4E_1}\frac{E_2\left((1-\nu_1)\frac{1+\nu_2}{1+\nu_1}-\nu_2\right)-E_1(1-2\nu_2)}{2E_1(1-2\nu_2)+E_2(1+\nu_2)} \end{array}\right]$$

$$B = a^5\left[\frac{T}{8E_1}\frac{E_1-E_2}{(7-5\nu_1)E_1+(8-10\nu_1)E_2}\right]$$

$$C = a^3\left[\frac{T}{8E_1}\frac{5(1-2\nu_1)(E_1-E_2)}{(7-5\nu_1)E_1+(8-10\nu_1)E_2}\right]$$

The distribution of local stress necessary to cause debonding, without the effect of overlapping stress concentrations, was found experimentally. From this distribution a random value was assigned as the strength of the particle-matrix bond (as there is no way directly measure the value) and it was divided by the calculated total stress concentration acting in that direction, giving a critical applied stress necessary to cause debonding. Because this simulation generates a random dispersion of spheres, there was variability in the calculated fraction debonded in each measurement. Therefore, the simulation was run five times for each condition and the results were averaged.

2.3 Results and Discussion

2.3.1 Stress concentration around a sphere

From the analytical solution, the stress concentration around a sphere was found to be a function of location (with reference to Fig. 2.5a expressed in terms of *r*, the radial distance, θ, the

polar angle, and ϕ, the azimuthal angle), the Poisson's ratio, ν, and the shear modulus, G of both the inclusion and matrix. Plots of the stress concentrations, assuming uniform tensile stress in the y direction computed using the material constants for glass and PVB, are shown in Fig. 2.5b-d. Fig. 2.5b shows the radial stress concentration to have a value of approximately 2.3 at the pole. Fig. 2.5c shows the tangential stress concentration (in the θ direction). It is tensile with a value of approximately 0.3 at the pole, and compressive at the equator, with a value of approximately 0.8. Fig. 2.5d shows the stress concentration in the φ direction to be tensile, with a value of approximately 1.0. Although it is clear that the stress concentrations decrease rapidly with distance from the inclusion, in a highly filled particulate composite these stress fields overlap, leading to elevated local stresses.

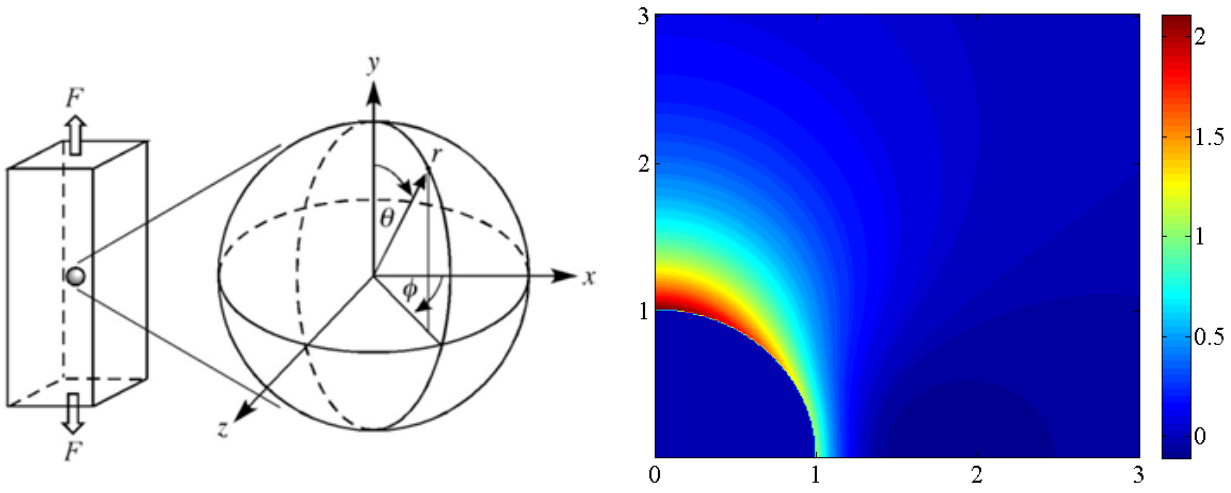

(a) (b)

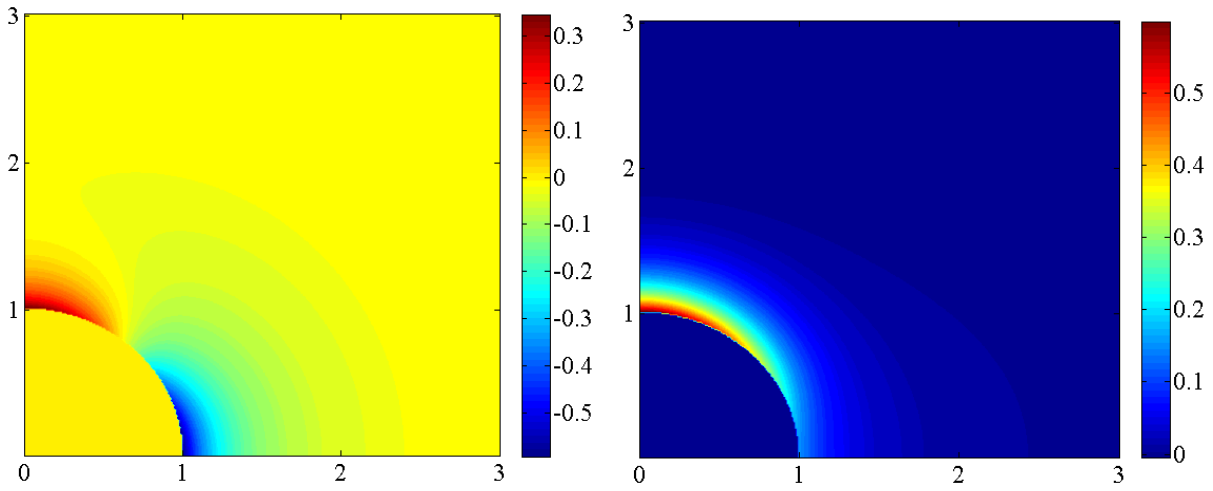

(c) (d)

Figure 2.5. a) A representation of the single sphere in an infinite matrix subjected to unidirectional tensile force and the coordinate system used. The stress concentration fields surrounding a rigid spherical inclusion in a soft matrix subjected to a uniform tensile stress, generated from Goodier's analytical solution, in the b) *r*-direction, c) θ-direction, and the d) ϕ-direction.

As the volume fraction of particles, φ, is increased, the average interparticle distance, <*r*>, in terms of radii of separation, is decreased. Assuming random packing, <*r*> can be calculated by Eqn. 2.7 [15]

$$< r >= \left[\left(\frac{0.637}{\varphi}\right)^{1/3} - 1\right] \qquad (2.7)$$

For the volume fractions of glass beads studied, 1, 5, 10 and 15 vol%, <*r*> is approximately 3.0, 1.3, 0.85 and 0.62, respectively. Although the range of stress concentration is small, at the higher volume fractions tested, the stress concentration overlap becomes significant. This is illustrated in Fig. 2.6, a heat map of the total stress concentration in the tensile direction in a cross section of the model composite, with 1 and 10 vol% particles. At 1 vol% the particle stress fields are non-interacting and debonding would occur at stresses similar to a single particulate

composite. At 10 vol% the overlap of the stress fields becomes significant, leading to unevenly distributed regions of high local stress.

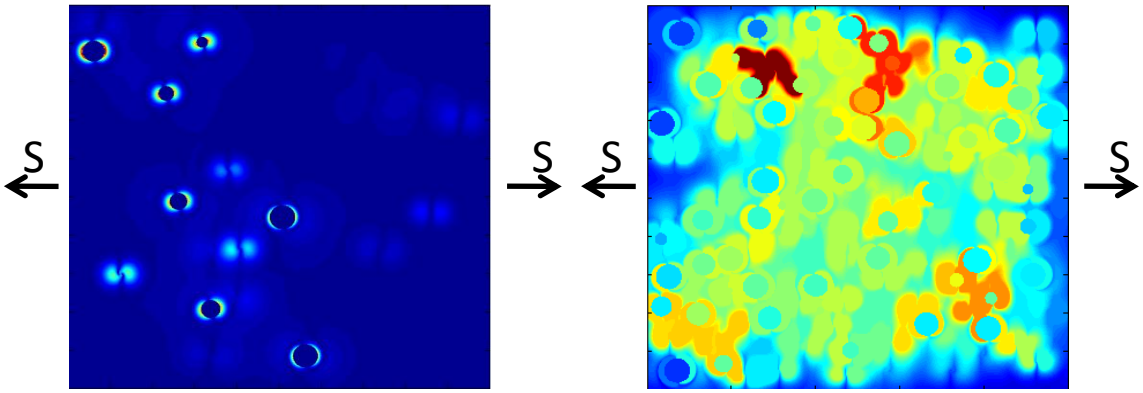

(a) (b)

Figure 2.6. A heat map showing the mid-plane cross-section of tensile stress concentration in the horizontal direction at a) 1 vol% and b) 10 vol% particles

2.3.2 Particulate-matrix adhesion

When tensile stress is applied, strain energy is stored in the specimen. When the strain energy stored in the volume of matrix near the pole of a particle is equal to the work of adhesion, W_A, the thermodynamic fracture energy per unit area, the particle-matrix interface will debond [16]. Thus, with knowledge of the Young's Modulus, E, of the matrix, W_A can be related to the local stress necessary to cause debonding, $S_{loc,crit}$, by Eqn. 2.8 [17]:

$$W_A = \frac{Rsin2\theta}{4E} S_{loc,crit}^2 \tag{2.8}$$

where, R is the radius of the particle, θ is the polar initial debonded angle. There was a distribution of $S_{loc,crit}$ values for a given particle surface chemistry because of chemical heterogeneity on the particle surface and θ is variable and unknown.

The applied stress necessary to cause debonding was determined from the 1 vol% particulate samples. The 1 vol% had an average interparticle separation of three radii, far enough to prevent interparticle effects. As the level of applied stress increased, the cumulative probability of debonding increased, until the matrix plastically yielded, preventing the application of higher stress. This distribution of applied stress necessary to cause debonding, $S_{loc,crit}$, was fit using the Weibull distribution. The Weibull distribution is often used in determination of failure rate proportional to time, use cycles, or strength. The cumulative Weibull distribution function is given in Eqn. 2.9:

$$F(S) = 1 - \exp\left(-\left({}^{S}/_{\lambda}\right)^{k}\right) \tag{2.9}$$

where, $F(S)$ is the fraction debonded at stress S, λ is the scale parameter and k is the shape parameter. The values for λ and k can be found by fitting a linear trend line with least squares regression analysis to the linear form of Eqn. 2.9, given in Eqn. 2.10:

$$\ln(-\ln(1 - F(S)) = k\, ln(S) - k \ln(\lambda) \tag{2.10}$$

The Weibull mean, was calculated with Eqn. 2.11:

$$Weibull\ mean = \lambda\Gamma(1 + {}^{1}/_{k}) \tag{2.11}$$

where, Γ, is the gamma function, given in Eqn. 2.12.

$$\Gamma(n) = \int_0^\infty x^{n-1}e^{-x}dx \tag{2.12}$$

Using Eqn. 2.10 the shape and scale parameters were found, and using Eqn. 2.11 the Weibull mean was found for both the untreated and aminosilane treated systems; these values are given in Table 2.2.

Table 2.2 The scale and shape parameters and Weibull means for the adhesive strength of bare and aminosilane treated glass beads in PVB

	Scale parameter [MPa]	Shape parameter	Weibull mean [MPa]
Untreated	38.3	6.83	35.7
Aminosilane	49.9	6.61	47.4

The slightly smaller shape parameter for the aminosilane treated system is indicative of a broader distribution of stress necessary to cause debonding. This was caused by the non-uniform surface modification during the silanization. The aminosilane treatment increased the Weibull mean stress necessary to cause debonding 33%. Aminopropyltriethoxysilane has been shown to improve the adhesion between glass and PVB by Lifshitz-van der Waals interactions, acid-base interactions between the basic amino groups and the acidic vinyl alcohol groups [18,19], and interdigitation of the PVB into the partially crosslinked APS layer on the glass surface [20].

In this system, as in most heterogeneous systems containing materials with different coefficients of thermal expansion that are processed at a temperature above which they are used, there is residual thermal stress [13,21,22]. PVB, like most polymers, has a significantly higher coefficient of thermal expansion than glass, and thus a compressive stress field forms around all inclusions when cooled. However, the critical local stress (the stress at the pole of a particle necessary to cause debonding) is a summation of the adhesion strength and the compressive residual thermal stress [13,20]. Thus, the distribution of experimentally determined critical local stresses, as described above, takes into account the residual thermal stress. It is assumed that the interparticle effects in composites with a moderate volume fraction of beads (up to 15 vol%) has no influence on the residual thermal stress. This assumption would be valid as long as there is a sufficient region of matrix surrounding the bead. If the amount of matrix between neighboring beads was very small, an equivalent thermal stress field would not develop.

2.3.3 Debonding in particulate composites

The effects of the distribution of adhesive strength, the use of an adhesion promoter, and the overlapping stress fields were seen experimentally. The graphs of the fraction debonded versus the applied stress for varying volume fraction of particles and surface treatment are shown in Fig. 2.7. APS surface treatment led to a decrease in debonding at a given applied stress, but the effect of particle volume fraction was proportionally the same.

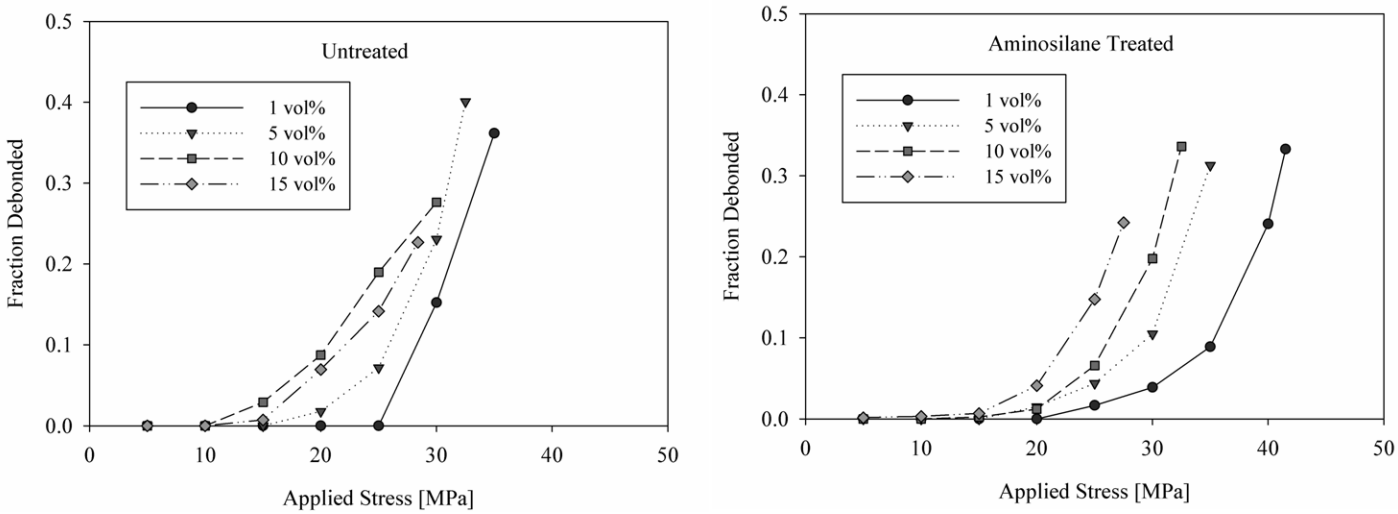

Figure 2.7. Graphs of the binned and averaged fraction debonded versus applied stress for both untreated and APS treated particulates

Increasing the number of particles decreased the interparticle distance, increasing the amount of interparticle stress concentration overlap. This led to higher levels of debonding at lower applied stress because the local stresses were still high enough to cause debonding. The dispersion of particulates in the matrix was not uniform, which can be seen in Fig. 2.4, this generated a distribution of local stress, creating a wider distribution of stress necessary to cause debonding at higher particle concentrations. The total fraction debonded particles was lower for higher particle concentrations because the tests were terminated when the specimen began to

plastically yield, which occurred in systems with higher particle concentrations due to stress concentrations in the matrix.

2.3.4 Modeling

The simulation was based on a virtual representation of the real system. A virtual composite with dimensions equal to the real composite was defined, then the number of spheres necessary to achieve the required volume fraction was calculated. Virtual spheres were then "placed" randomly within the bounds of the composite and checked for overlap with pre-placed spheres. This was problematic for the 15 vol% samples as the likelihood of randomly placing a sphere in an unoccupied space was very low, leading to long run times. Moreover, this did not generate dispersions that accurately represented the real systems, which had a wider distribution of interparticle spacing. An illustration of the virtual composite with 15 vol% particulates is shown in Fig. 2.8.

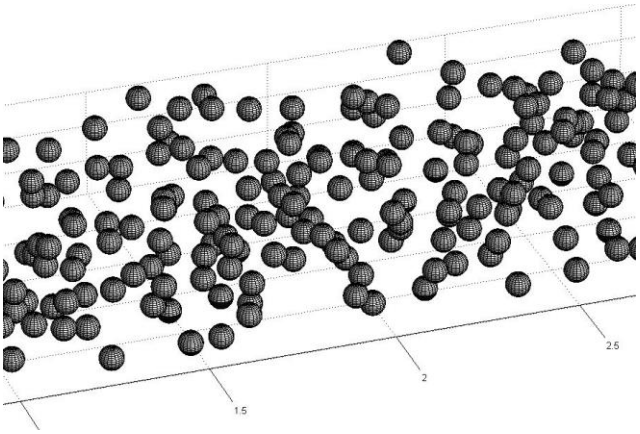

Figure 2.8. A drawing of the virtual composite with 15 vol% generated for the simulation

Next, the locations of the poles were determined. One pole at a time, the stress concentration normal to the pole caused by every sphere in the composite was calculated and

summed. In other words, a point in space corresponding to a pole was considered individually, then a single neighboring sphere was considered and the stress concentration caused by that sphere was calculated. This was repeated for each sphere in the composite, then the calculated stress concentrations were summed giving a total stress concentration. This was then repeated for each pole. Only the stress concentration at the pole was considered because it was observed experimentally that it was the origin of the debond. This method is simplistic, as it is just a summation of the single particle solutions at a point but it does not consider how the particles transfer stress differently than the matrix. However, the range of the stress concentrations is very short, so only the nearest neighbors would contribute to the local stress significantly.

A random value from the experimentally determined Weibull distribution of stress needed to cause a debond was assigned to each pole. Finally, this value was divided by the stress concentration. For example, if the local stress is twice the applied stress (a stress concentration of two), the particle will debond at half the applied stress necessary to cause debonding for the single particle case. This was repeated for each pole, generating a fraction debonded versus applied stress curve similar to the experimental values.

There were a number of explicit and implicit assumptions in this model. It was explicitly assumed that there was a random dispersion of spheres, that debonding occurred at the poles, that there was a Weibull distribution of critical stresses, that debonding at one pole prevented it from occurring at another, and that the stress normal to the pole determined failure. It was assumed implicitly that the glass beads and the matrix transfer stress in the same manner, that the matrix was linear elastic, that no other stress release mechanisms (e.g. plastic yield) were relevant, and that the finite dimensions of the composite did not lead to an increase in local stress.

The calculated fraction debonded as a function of applied stress for a given volume fraction particles is plotted with the experimental data in Fig. 2.9 for bare particles and Fig. 2.10 for APS treated particles. Given the relatively good fit between the calculated and experimental values, it can be concluded that the debonding was largely controlled by the distribution of overlapping stress concentrations and thus the distribution of local stresses. However, at higher stresses in the 10 and 15 vol% APS treated systems, the model under predicted the level of debonding. This may be caused by a non-linear elastic response of the matrix, such as local yielding, which becomes the dominant microscopic failure mechanism in particulate composites having good adhesion, stiff particles and a soft matrix [23].

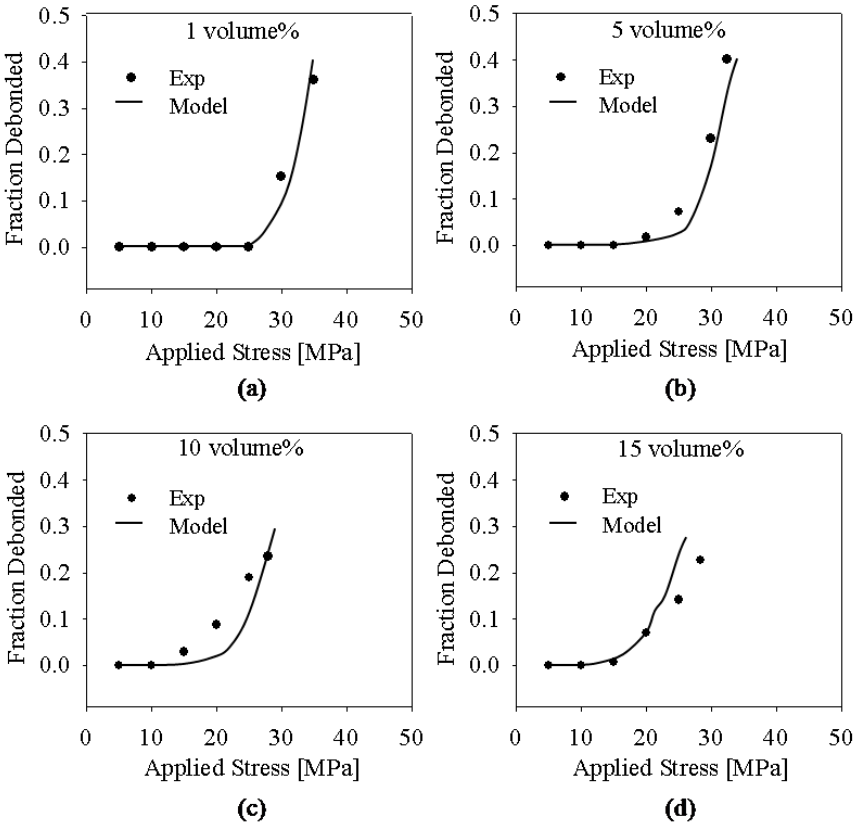

Figure 2.9. Comparison of the model (smooth line) against the experimental data (circles) for the fraction of debonded spheres versus applied stress at a) 1 vol%, b) 5 vol%, c) 10 vol%, and d) 15 vol% glass beads with no surface treatment

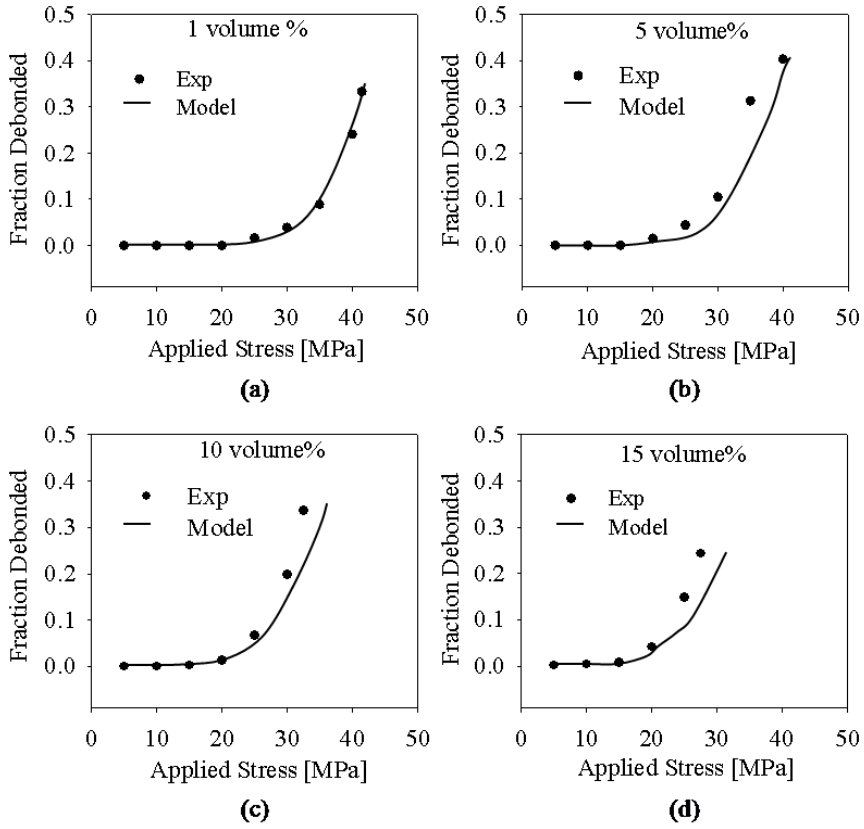

Figure 2.10. Comparison of the model (smooth line) against the experimental data (circles) for the fraction of debonded spheres versus applied stress at a) 1 vol%, b) 5 vol%, c) 10 vol%, and d) 15 vol% glass beads with the APS adhesion promoter

2.4 Conclusions

As the volume fraction of spherical glass beads in filled poly(vinyl butyral) PVB composites increased, the fraction of inclusions that were debonded at a given applied stress increased because of an increase in the overlap of the stress fields caused by a reduced average interparticle separation of the inclusions. If the glass beads were treated with an APS, which improved the adhesion, the level of debonding at a given stress and filler concentration was less than that of the system with no surface treatment at all applied stresses. A simple model that assumed superposition of the stress fields from neighboring spheres predicted the dependence of

the fraction of debonded particles on particle volume fraction (up to 15 vol%) at any applied stress level below that required to cause macroscopic plastic failure of the specimen.

References

[1] Plastics and Rubber Institute, British Plastics Federation, editors. Fillers: proceedings of the joint conference of the Plastics and Rubber Institute and the British Plastics Federation, March 1986. London, England; New York, NY, USA: Plastics and Rubber Institute ; Elsevier Science Pub. Co.; 1986.

[2] Sjögren BA, Berglund LA. Failure mechanisms in polypropylene with glass beads. Polym Compos 1997;18:1–8.

[3] Renner K, Yang MS, Móczó J, Choi HJ, Pukánszky B. Analysis of the debonding process in polypropylene model composites. Eur Polym J 2005;41:2520–9.

[4] Gent AN. Detachment of an elastic matrix from a rigid spherical inclusion. J Mater Sci 1980;15:2884–8.

[5] Gent A, Park B. Failure Processes in Elastomers at or Near a Rigid Spherical Inclusion. J Mater Sci 1984;19:1947–56.

[6] Hutchinson JW. Crack tip shielding by micro-cracking in brittle solids. Acta Metall 1987;35:1605–19.

[7] International Conference on Composite Interfaces I, Hatsuo, Koenig JL, editors. Composite interfaces: proceedings of the First International Conference on Composite Interfaces (ICCI-I) held May 27-30, 1986, in Cleveland, Ohio, U.S.A. New York: North-Holland; 1986.

[8] Lee J, Yee AF. Fracture of glass bead/epoxy composites: on micro-mechanical deformations. Polymer 2000;41:8363–73.

[9] Kraus R, Wilke W, Zhuk A, Luzinov I, Minko S, Voronov A. Investigation of debonding processes in particle-filled polymer materials by acoustic emission: Part I Acoustic emission and debonding stress. J Mater Sci 1997;32:4397–403.

[10] Nguyen FN, Berg JC. Use of an Optical–Mechanical Test Combined with Acoustic-Emission Techniques to Study Adhesion in Filled Polymeric Composites. J Adhes 2005;81:823–41.

[11] Miller AC, Minko S, Berg JC. Application of acoustic emission measurements to investigate adhesion in filled polymeric composites. J Adhes 2001;75:257–66.

[12] Nguyen FN, Berg JC. The effect of vinyl alcohol content on adhesion performance in poly (vinyl butyral)/glass systems. J Adhes Sci Technol 2004;18:1011–26.

[13] Harding PH, Page SA, Manson J a. E, Berg JC. Measurement of residual stress effects by means of single-particle composite tests. J Adhes Sci Technol 1998;12:497–506.

[14] Goodier J. Concentration of stress around spherical and cylindrical inclusions and flaws. J Appl Mech 1933;55:39–44.

[15] Cosgrove T. Colloid science principles, methods and applications. Oxford, UK; Ames, Iowa: Blackwell Pub.; 2005.

[16] Griffith AA. The Phenomena of Rupture and Flow in Solids. Philos Trans R Soc Lond Ser Contain Pap Math Phys Character 1921;221:163–98.

[17] Mossakovskii V., Rybka M. Generalization of the grippith-sneddon criterion for the case of a nonhomogeneous body. J Appl Math Mech 1964;28:1277–86.

[18] Miller AC, Berg JC. Unexpected behavior between polystyrene and untreated and silane-treated glass beads in filled polymeric composites. J Appl Polym Sci 2003;89:521–6.
[19] Fowkes FM. Role of acid-base interfacial bonding in adhesion. J Adhes Sci Technol 1987;1:7–27.
[20] Miller AC, Berg JC. Effect of silane coupling agent adsorbate structure on adhesion performance with a polymeric matrix. Compos Part -Appl Sci Manuf 2003;34:327–32.
[21] Beck R, Gratch S, Newman S, Rusch K. Yield Behavior of Polyblends. J Polym Sci Part B-Polym Lett 1968;6:707–&.
[22] Asp LE, Sjogren BA, Berglund LA. Prediction of failure initiation in polypropylene with glass beads. Polym Compos 1997;18:9–15.
[23] Pukanszky B, Voros G. Stress distribution around inclusions, interaction, and mechanical properties of particulate-filled composites. Polym Compos 1996;17:384–92.

Chapter 3 – Nano-voids in thermosets

cf. Rutz B.H., and Berg J.C., "A Review of the Feasibility of Lightening Structural Polymeric Composites with Voids without Compromising Mechanical Properties," *Advances in Colloid and Interface Science.* **160**, 56-75 (2010).

Summary

One of the most important attributes to composite materials is their relatively low weight; it follows that reducing the weight further would be advantageous. Introducing voids into the thermoset, continuous phase of a composite with dimensions small enough to generate an effectively homogeneous, lightweight material is one way to reduce the composite weight. However, producing nano-sized voids in a thermoset is a difficult, multistep process that could potentially be accomplished via many different means. A literature review was conducted to determine possible methods, and challenges. It was concluded that using block copolymer micelle blowing agent wells was the best potential method. The use of hollow micro or nano-particles was considered, but the potential weight reduction was minimal. Initially a fluorinated block copolymer was used in an attempt to make micelles, but underwent chemically induced phase separation. Fortegra 102 (Dow Chemical Company, Midland, MI), which is believed to be poly(butyl oxide)-*block*-poly(ethylene oxide) (PBO-PEO), self-assembled into micelles, which were swollen with heptane, achieving two important milestones in generating the proposed material. Poly(ethylene)-*block*-poly(ethylene oxide) also generated micelles, which were swollen with pentane. A number of intermediate steps necessary to create a nano-void lightened thermoset were accomplished; to date, the goal material has not been produced.

3.1 Introduction

Continuous fiber reinforced plastics (CFRPs) are a class of materials generally made with high strength, high stiffness fibers made from materials such as ceramics, carbon, and poly(p-phenylene teraphthalamide) (Kevlar) embedded into a continuous polymer matrix, often a thermoset. CFRPs can have extraordinarily high strength and stiffness, and low densities, giving them very good mechanical properties per unit mass, or *specific* mechanical properties. A well designed composite structure would have the major loads applied in the direction of the fibers, as the fibers are best suited to carry load, while the matrix protects fibers from environmental damage, and transfers load between fibers, and around fiber ends [1]. It follows that CFRPs are manufactured with high volume fractions of fibers, often 55 – 65 vol%. Higher fiber volume fractions lead to insufficient resin penetration of the fiber tows, and significantly reduced properties [2]. To further increase the ratio of fibers to matrix it may be possible to incorporate nano-sized voids into the matrix that would occupy the interstitial space between fibers. In other words, one could make a resin with voids small enough to create an effectively homogenous, low density resin. The material generated would be a *kugelschaum,* a solid with spherical, separate voids, distinct from most foams which have large, closely packed polyhedral cells.

There are three common methods used for adding gas-filled voids to polymers: the incorporation of bubbles by "whipping" or sparging gas into the polymer, the addition of hollow spherical particles, called microballoons, and gas nucleation (by either precipitation or generation from chemical blowing agents) [3]. The addition of microballoons can be considered, in part, an attempt to compensate for the inherent weakness caused by the introduction of voids by reinforcing the void with a wall. However, the effectiveness of the reinforcement from the microballoon wall is dependent on the type of applied load, adhesion [4–6], wall thickness [7–

11], volume fraction [11–16], and size [6,12,17]. In gas precipitation, a physical blowing agent that has been dissolved in the matrix is precipitated into a separate phase by either an increase in temperature or a decrease in pressure, decreasing the solubility, until the formation of a gas phase highly thermodynamically favorable. The creation of sub-micron and nano-sized voids by gas precipitation is generally difficult to control, but a number of methods to create *blowing agent wells* have been developed, which could improve control over the morphology. In gas formation, a blowing agent undergoes decomposition to form a gas, with the reaction generally induced by an increase in temperature. It may be possible to partition chemical blowing agents into micelles, allowing for control of the size and number density that would not otherwise be possible. In this work, micelles, or self-assembled spherical aggregates of amphiphiles with a radius roughly equal to the length of the amphiphile molecule, would be made with block copolymers with a continuous phase miscible and a continuous phase immiscible block. They are discussed in detail in section 3.2.3.

Initially a literature review was conducted to determine possible methods for generating a kugelschaum in a thermoset, with the goal of reducing the density without significantly reducing the specific mechanical properties. The findings are summarized in the next section. From the review, it was concluded that the using block-copolymer micelle blowing agent wells was the most promising means to make these materials. Next, Zonyl FSN and Zonyl FSO, perfluorinated alkane-*block*-poly(ethylene oxide) (PEO) oligomers, were investigated as potential blowing agent well formers, because their fluorinated chemistry would allow for significant partitioning of a perfluorinated blowing agent if they self-assembled into micelles. It was found that as the thermoset cured, the solubility of the PEO block was reduced, causing bulk phase separation. The use of poly(ethylene)-*block*-poly(ethylene oxide) PE-PEO to make micelles in a thermoset

was investigated, but in most cases, it formed worm like micelles or bulk phase separated, depending on reaction conditions because the PEO volume fraction of the block copolymer segment was not large enough. Fortegra 102, poly(butyl oxide)-block-poly(ethylene oxide) (PBO-PEO) is a commercially available block copolymer that forms micelles in many epoxy matrices. It was found that slow, room temperature curing generated a thermoset with micelles that were present after the cure. When heptane was added to the system, it would partition to the interior of the micelles, causing them to swell to 25 nm in diameter. This material could be used to make a nano-bubble lightened thermoset.

3.2 Review summary

In order to better understand the opportunities and challenges associated with making nano-sized discrete spherical voids in a thermoset the literature was surveyed, and the findings were published as a review paper. A summary of the review is given here.

3.2.1 Microballoons

Microballoons are a hollow spheres usually made from glass or phenolic resin, with diameters between 30 to 80 μm and wall thicknesses between 0.5 and 2 μm. They can be mixed with thermoplastics or thermosets to create a lightweight material called *syntactic foam*, which has applications as core material in sandwich structures [18,19], buoyancy aids, as lightweight fillers, and high performance thermal insulation [20]. A micrograph of the fracture surface of a syntactic foam is shown in Fig. 3.1. In the application considered here, lightening continuous fiber composites with voids, microballoons have a marked advantage over traditional polymer foaming techniques where gas is formed into bubbles by precipitation or chemical decomposition. In those cases the fibers could act as heterogeneous nucleation sites, generating bubbles on the surface of the fibers, reducing the ability of the matrix to transfer load to the fiber,

reducing the mechanical properties of the composite. With microballoons, because the gas pockets are enclosed by a wall and physically mixed, there is no nucleation the surface of the reinforcements. Additionally, their size is fixed, prior to incorporation into a matrix, potentially reducing the complexity of processing.

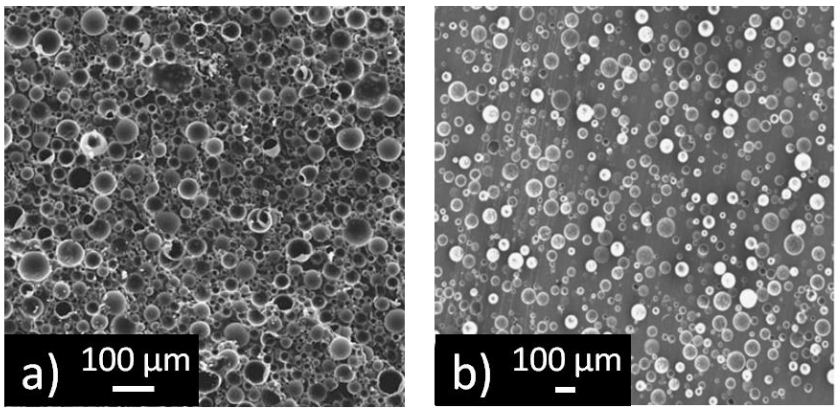

Figure 3.1. Scanning electron microscope (SEM) image of syntactic foam made with a) 60 vol% glass microballoons, b) 30 vol% glass microballoons [21]

Typical, commercially available microballoons are too large to be incorporated into continuous fiber composites. It is possible to generate hollow spheres with sub 100 nm diameters, and carefully tailored wall thicknesses. Most of these are made with latex [22–25], micelle [26], mineral nanoparticle [27] or emulsion templates; a review of these techniques was given by Lou, Archer and Yang [28]. In these processes, the template is coated with silane, boron, carbon or polymer by reaction from a dissolved precursor or by deposition of nanoparticles. After the shell is formed the template is removed by pyrolysis, dissolution, or selective etching (*e.g.*, removing a silica template with HF) leaving a hollow core. For example, hollow carbon spheres were made from the pyrolysis of polystyrene-polyacrylonitrile blend nanoparticles [29], and silica spheres were made by the condensation of tetraethoxysilane at the interfaces in an oil-in-water emulsion [30].

Commercially available microballoons are two orders of magnitude too large to be incorporated in CFRPs, however, syntactic foams made with microballoons and nano-composites made with solid particulates, are considered here in lieu of any published literature on syntactic foams made with hollow *nano*-spheres. The mechanical properties of syntactic foams can vary widely depending on composition, but in general, they have good compressive strength, but poor tensile and shear strength due to interfacial or microballoon failure. The most important parameters are materials selection, wall thickness, balloon volume fraction, size, and adhesion between the microballoons and the continuous phase.

Increasing the wall thickness increases the wall thickness increases the modulus; for glass microballoons, if the ratio of inner to outer radius is roughly less than 0.96 the addition of microballoons would lead to an increase in modulus [10]. The compressive strength of the syntactic foam increases with increasing wall thickness [10,31]. The tensile strength is typically limited by the microballoon-matrix adhesion, so wall thickness has little influence. However, if there were strong adhesion, increasing the wall thickness would increase the tensile strength, as long as the failure mechanism was microballoon failure.

In particulate composites, with spherical fillers larger than 1 μm, varying the size often has no impact on mechanical properties [32]. However, using nano-sized particulates can improve the strength [17,32,33] and modulus [33,34]. In stiff polymers, the toughness, and fracture toughness can also be increased with decrease particle size. The increase in fracture toughness is typically attributed to energy absorbing mechanisms including, microcracking [35] (small, discontinuous cracks that are formed ahead of the main crack), shear yielding [36] (local regions of plastically deformed matrix ahead of the crack tip near the fillers), and crack bowing [7,37,38] (or crack pinning, where the crack front is halted by well bonded inclusions, but

continues in the regions between them). Additionally, nanoparticles can lead to an increase in surface area of the fracture surface, increasing the energy needed to propagate a crack.

The mechanism for increased strength with decreasing size is still under debate. One possible reason is smaller particles have smaller regions of poor initial adhesion between the particle and the matrix [39]. If it was assumed that a debonding event *could* occur if the strain energy in the vicinity of the particle were greater than the energy required to create a new surface, and that the initial debond was small, it was determined using the Griffith energy balance that the stress for debonding a poorly adhered particulate is [40]:

$$s^2 = \frac{4\pi G_a E}{3a} \tag{3.1}$$

where G_a is the bond fracture energy per unit area of bonded surface, E is Young's modulus of the matrix, and a is the radius of initial debond. Equation 3.1 assumes that there is initially a region of incomplete bonding, but there is no way to know the exact size of that region. However, the size of the debond would decrease with decreasing particle size, explaining the improvement found in experiments. Another possible reason for the increased strength is simply from the increase in fracture toughness. All materials have intrinsic flaws, and in the case of many thermosets, these flaws can cause brittle failure at stresses well below the theoretical maximum. By decreasing the particle size, the fracture toughness is increased and the effect of these flaws is mitigated, leading to higher applied stress necessary to cause failure.

There are few reported attempts to improve the adhesive bond in syntactic foams. In one experiment the effects of a silane coupling agent, and thus adhesion, on a three-phase syntactic foam was investigated [4]. A three-phase syntactic foam contains voids outside the microballoons, in the matrix. It was found that under compressive stress a syntactic foam made

with A16 microballoons, which are made of glass and have a density of 0.16 g/cm^3 had nearly the same strength, both with and without a silane coating, implying that interfacial strength played a minor role under compressive loading. Under flexural load, however, the interfacial strength was much more significant. The syntactic foam made with uncoated A16 microballoons exhibited nearly twice the flexural strength of the syntactic foam made with silane coated A16 microballoons and about 25% higher strength than syntactic foam made with untreated B38 microballoons, even though the B38 microballoons had an isostatic crush pressure eight times that of the A16 microballoons, thus showing the significance of interfacial strength under flexural loading.

The above example is for a three-phase syntactic foam which contains a very small volume fraction of resin, and only one type of unspecified coupling agent was tested, limiting the conclusions that can be drawn. However, there is an extensive literature on the influence of adhesion on the mechanical properties and failure mechanisms of solid particulate composites. In general a coupling agent improves the adhesion and thus the mechanical properties under tensile and flexural stress. Similarly, if the failure mechanism were debonding in syntactic foam there would be an improvement in the tensile and flexural mechanical properties with increasing adhesion.

It may be possible to make nano hollow spheres out of a variety of materials, and then incorporate them into a polymer matrix. This material could have improvements in strength, fracture toughness and modulus, while reducing weight. There are a number of challenges with making these materials including the manufacture of spherical, uniform, and disperse particulates remains a challenge. Moreover, the total weight reduction would be modest, given the need to make the bubble walls thick enough to survive processing.

3.2.2 Micro/nano-cellular foams

The second major strategy for the creation of gas voids within a resin matrix is foaming, where gas bubbles are nucleated physically or chemically within the polymer when it is in liquid form. When cured or solidified, the result is generally a polyhedral cellular structure in which the gas phase volume fraction is in excess of 50%, and is referred to as a *foam*. While such materials show extremely large weight reductions relative to the neat resin, their strength and moduli are drastically reduced. If mechanical properties are to be retained to any degree, the type of foam must be one of separate, spherical bubbles, a *kugelschaum*, i.e., "spherical foam."

It is possible to make foams out of a number of materials with a wide range of techniques. With the exception of polyurethane, most foams are made from thermoplastics either by solubilizing a gas, typically at elevated pressures, then reducing the pressure or increasing the temperature to cause nucleation of the gas phase, or with chemical blowing agents, which are chemicals that generate gas via thermal decomposition. These foams have a wide variety of uses, but are not typically used for structural applications. The large amounts of gas that must be dissolved to obtain sufficient supersaturation to nucleate bubbles cause the bubbles to rapidly grow large. Chemical blowing agents are typically powders with micron sized particles and they generate a gas bubble much larger than the particulate size. The size depends on local pressure, chemical used, and particulate size. Alternatively, if the chemical blowing agent is solubilized, sufficient gas must be generated to create a supersaturation condition, similar to the use of physical blowing agents.

Typical foaming techniques generate cells that are several microns up to several millimeters in diameter, and would be too large to fit in the interstitial space between fibers of a CFRP. Additionally, if the bubbles are not perfectly spherical, which is often the case in real

systems due to constraints on the flow of the resin during foaming from reinforcements, neighboring bubbles, and/or the mold, the stress concentration would depend on the bubble size. This has led a number of researchers to postulate that incorporating bubbles smaller than the flaws inherently present in a matrix would not significantly reduce the specific mechanical properties [41,42]. It is generally impossible to know the size of an intrinsic flaw, though it varies depending on the system and specimen preparation, it follows that bubbles should be as small as feasible.

The change in energy associated with the homogeneous nucleation and growth of a gas bubble in a polymer matrix is dependent on the energetic cost of generating new surfaces and the volume free energy. Given that the bubble will nucleate as a sphere to minimize the free energy, the Gibbs free energy, ΔG, associated with homogeneously generating a bubble of radius r is [43–45]:

$$\Delta G = -\left({}^{4}/_{3}\right)\pi r^{3}\Delta P + 4\pi r^{2}\sigma \tag{3.2}$$

where ΔP is the difference in pressure inside the bubble and in the continuous phase, often approximated to be the pressure of gas used to saturate the polymer, assuming the dissolved gas behaves as an ideal gas [43] and σ is the surface tension between the bubble and polymer. This is illustrated in Fig. 3.2.

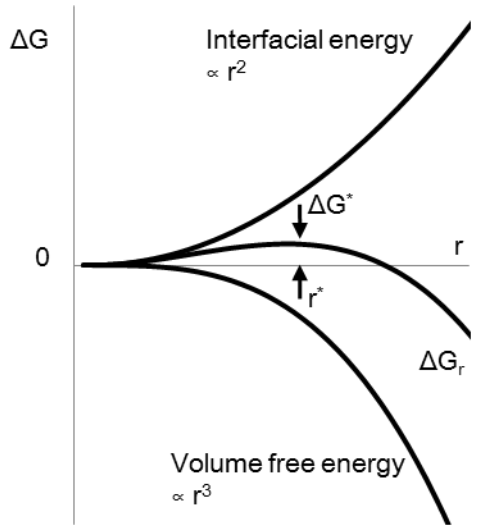

Figure 3.2. The change in Gibbs free energy associated with the homogeneous nucleation of a bubble

From Fig. 3.2, it can be seen that there is an energy barrier, ΔG^*, and a critical radius, r^*, associated with the nucleation of a new bubble. A bubble with a radius of r^* would be unstable, and would either dissolve back into the polymer, or grow. Values for ΔG^* and r^* can be calculated by differentiating Eqn. 3.2, yielding:

$$r^* = 2\sigma/\Delta P \tag{3.3}$$

$$\Delta G^* = \frac{16\pi\sigma^3}{3\Delta P^2} \tag{3.4}$$

In the classical Becker-Döring model for homogeneous nucleation [45], the rate, N_0, is the rate of formation of bubbles of critical size in a polymer melt. N_0 is given by an Arrhenius expression:

$$N_0 = C_0 f_0 exp\left(\frac{-\Delta G^*}{kT}\right), \tag{3.5}$$

where C_0 is the number of gas molecules dissolved per unit volume, f_0 is a kinetic pre-exponential factor, k is the Boltzmann constant, T is absolute temperature.

From Eqs. 3.4 and 3.5 it can be seen that to control the nucleation rate in a given system the temperature, degree of saturation and pressure drop need to be controlled.

Once nucleated, bubbles will continue to grow, with the growth rate limited by the mechanical resistance of the continuous phase and diffusion [46] until they are constrained by adjacent bubbles, a mold wall, reinforcements, or increased polymer viscosity, they coalesce with adjacent bubbles, or there is inadequate dissolved blowing agent to support continued growth. The addition of blowing agents often reduces the glass transition temperature, T_g, of the polymer. This has been exploited by foaming at a temperature above the T_g of the polymer with dissolved blowing agent, but below the T_g of the neat polymer. Bubble nucleation and growth is illustrated in Fig. 3.3.

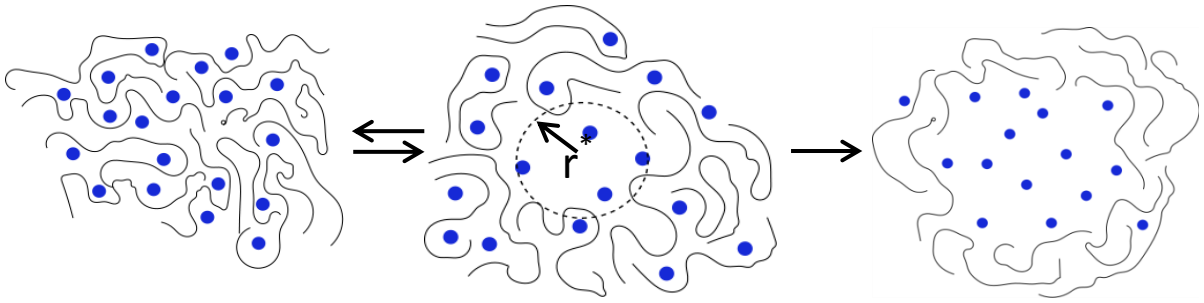

Figure 3.3. An illustration of the bubble nucleation and growth of bubbles in a homopolymer, where the blue dots represent dissolved gas molecules and the black lines are the polymer

Block-copolymer micelles have been used successfully in thermoplastics to reduce the average bubble size. The block-copolymer can form self-assembled, micelle *blowing agent wells;* regions several nanometers in diameter of high blowing agent concentration. Thus, when a bubble nucleates its growth would be limited by the amount of blowing agent in the micelle. This is shown schematically in Fig. 3.4. In one experiment performed by Yokoyama and Sugiyama [47], poly(styrene-*block*-perfluorooctylethyl methacrylate) (PS-PFMA) and

poly[styrene-*block*-4-(perfluorooctylpropyloxy)styrene] (PS-PFS) diblock copolymers were added to a polystyrene (PS) matrix in an attempt to make micelle wells. The block-copolymers micelles were saturated with CO_2 and then slowly depressurized at 0.5 MPa min^{-1}, at varying temperatures, but 0°C produced the smallest cells, 20 nm, and the most uniform size distribution, shown in Fig. 3.5(a). An unconventionally slow pressure release rate was used to prevent cracking in the glassy polymer at low temperatures. An unusually low temperature was used to restrict bubble growth after nucleation, and because at higher temperatures, even at 30°C, well below the T_g of PS, there was some cell consolidation, leading to a bimodal size distribution of nano- and microcells, shown in Fig. 3.5(b).

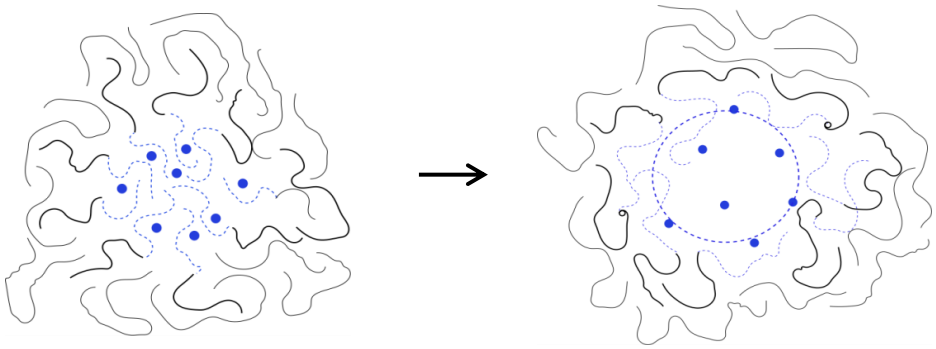

Figure 3.4. An illustration bubble nucleation from in a blowing agent well, the lack of dissolved gas in the homopolymer would prevent continuous bubble growth, the block copolymer is represented by a line with a bold black segment (continuous phase miscible) and a dotted blue segment (continuous phase *im*miscible)

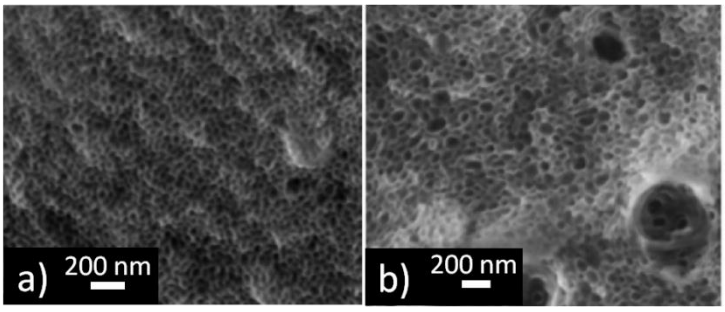

Figure 3.5. An SEM micrograph of the fracture surface of poly(styrene) foamed with poly[styrene-*block*-4-(perfluorooctylpropyloxy)styrene] blowing agent wells with CO_2 depressurized at a) 0°C and b) 30°C [47]

In another similar, but distinct method, blowing agent wells can be created by forming an immiscible polymer blend, instead of relying on the self-assembly of block copolymers [48,49]. This has been done using polypropylene (PP) as the matrix and poly(propylene-*block*-ethylene) (PER) for the discontinuous regions [50]. The blowing agent, CO_2, was about 2.5 times more soluble in the PER at the saturation pressure and temperature, causing them to act as CO_2 wells. Additionally, the PP was more rigid than the PER, so the PP matrix served to restrict the bubble growth. At 25 wt% PER the discontinuous regions were on average 0.4 μm in diameter, an SEM image of this system is show in Fig. 3.6a, where the darker circles are PER blowing agent wells, and the lighter, continuous region is the PP matrix. After foaming, the cell diameter was only 0.5 μm, smaller than typically possible with more basic microcellular foaming techniques, an SEM image of the kugelschaum is shown in Fig. 3.6b.

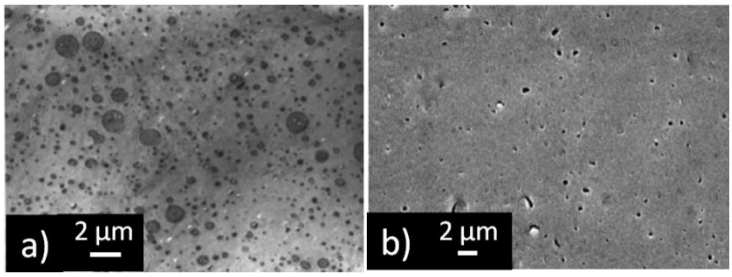

Figure 3.6. An SEM of a) poly(propylene-*block*-ethylene) discontinuous regions in polypropylene and b) after the material had been foamed with CO_2 [50]

As stated earlier, most foamed polymers are thermoplastics because a degree of control over bubble size and coalescence can be had by controlling the temperature after bubble nucleation. In microcellular foaming this is particularly important because a rapid temperature drop, below the T_g of the polymer, arrests bubble growth immediately after nucleation. This is not an option in foaming thermosetting polymers; the transition from a liquid to a solid is controlled by the rate of cure, which is generally too slow to arrest bubble growth. This is a

problem that would need to be solved if foaming techniques were used to lighten high performance fiber-polymer composites, which are almost exclusively made from thermosets. The most likely solution would be to partially cure the resin (as is done with a “prepreg”), saturate with blowing agent, nucleate the bubbles, form the desired part, and finally complete the cure. Partially curing the resin would create a viscoelastic solid, restricting bubble growth and coalescence. This is not an unreasonable suggestion as the prepreg industry has developed strategies for accurately controlling partial cures, and it has been shown that in order to prevent coalescence the matrix must be very rigid.

3.2.3 Block copolymer micelles in thermosets

An amphiphile is a compound possessing both solvent soluble and solvent insoluble properties. Let us consider briefly aqueous systems, where an amphiphilic molecule would have a hydrophilic side (the *head* of the amphiphile), often an ionic species or a poly(ethylene oxide) (PEO) segment covalently bound to a hydrophobic side (the *tail* of the amphiphile), often an alkane. At low concentrations, the amphiphile will exist as dissolved single molecules, if the hydrophobic portion is not too large. If the concentration is increased sufficiently, many amphiphiles will self-assemble into nano-scale spherical structures called micelles, shown in a Fig. 3.7. This concentration is the critical micelle concentration. Micelles form because they create a hydrophobic core that is devoid of water, reducing the unfavorable interaction between the hydrophobic moiety and water.

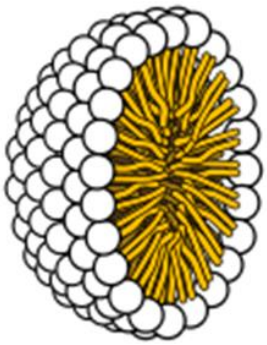

Figure 3.7. A representation of the cross section of a surfactant micelle, the white spheres are the hydrophilic head group and the yellow lines are the hydrophobic tail groups [1]

Increasing the amphiphile concentration leads to an increase in the number of micelles, but generally, the aggregation number, the number of amphiphile molecules in a micelle at equilibrium, remains fixed. This narrow distribution is caused by a narrow minimum of the Gibb's free energy of micellization. If a micelle has fewer amphiphile molecules than the aggregation number, the addition of an amphiphile molecule would decrease in the free energy by minimizing the interaction between the hydrophobic moiety and water, but once the micelle has enough monomers to have a close packed hydrophilic shell, additional monomers would be energetically unfavorable from strong steric repulsion, or in the case of charged head groups, electrostatic repulsion, between the hydrophilic moieties. In the application considered here, this is a very advantageous phenomenon. The number of blowing agent wells could be easily controlled with the amphiphile concentration, and their size would be consistent.

Micelles in water provide apolar domains, permitting the *solubilization* of apolar chemicals such as oils many polymer monomers that would otherwise be sparingly soluble or insoluble.

[1] This illustration is public domain, and can be found at:
http://upload.wikimedia.org/wikipedia/commons/c/c6/Phospholipids_aqueous_solution_structures.svg

With an understanding of micelles in aqueous solutions, it is possible to infer what materials would create micelles in an epoxy resin. It has been shown by a number of researchers that poly(ethylene oxide) (PEO) is soluble in many bisphenol A diglycidyl ether (BADGE) epoxies with many curing agents [51,52].

Bates and coworkers have developed numerous block copolymers based on a poly(ethylene oxide) soluble head group with poly(ethylene-*alt*-propylene) [53–56], poly(ethyl ethylene) [57], poly(butylene oxide) [58], poly(hexylene oxide) [59,60] tail groups as well as poly(methyl methacrylate)-*block*-poly(2-ethylhexyl methacrylate) [61], poly(methyl methacrylate-*co*-glycidyl methacrylate)-*block*-poly(2-ethylhexyl methacrylate) [61], and poly(1,2-butadiene)-*block*-poly(epoxy-1,4-isoprene-*ran*-1,4-isoprene) [62,63]. At concentrations of 5 to 10 wt% these block copolymers self-assemble into vesicles, worm like micelles or spherical micelles in epoxy resins with aromatic amine curing agents, depending on the size of the PEO block. A PEO block 45 to 60 vol% of the block copolymer would self-assemble into micelles, where smaller PEO blocks 10 to 45 vol% would self-assemble into worm like micelles or vesicles, depending on the composition. Additionally, poly(ethylene)-*block*-poly(ethylene oxide) (PE-PEO), MW = 1,400, 50 wt% PEO has been shown to form spherical micelles in epoxy resin with methylenedianiline at concentrations between 5 and 30 wt% block copolymer [64].

The self-assembled structure is dependent on the relative size of the resin miscible group to resin immiscible group. The resin miscible group must occupy a large enough area to generate a sufficiently small radius of curvature to cause self-assembly into micelles, shown in Fig. 3.8a and 3.8b. This is analogous to the "critical packing parameter:" $v/a_0R \leq 1/3$, where v

and *R* are the volume and length of the epoxy immiscible group and a_0 is the effective head group area. Qualitatively, this corresponds to a block copolymer with roughly 50 vol% PEO.

As the cure progresses, the PEO groups are expelled from the continuous phase, reducing their volume, Fig. 3.8c. If the diffusivity is low enough, the pre-cure structures are locked in place, as is commonly reported in the literature. However, if a partial cure is sufficient to reduce the effective size of the PEO domain, while diffusivity is still relatively high, there may be an order-order transition from spherical micelles to cylinders or worm like micelles, Fig. 3.8d, or if the solubility is sufficiently reduced there may be bulk phase separation, Fig. 3.8e.

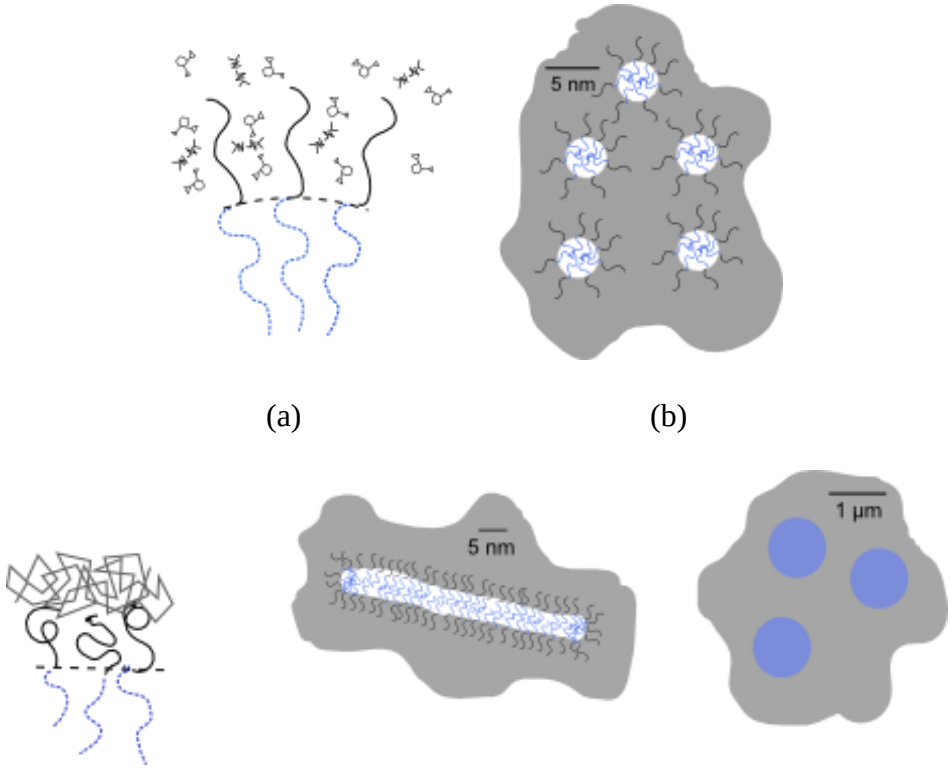

Figure 3.8. An illustration of some block copolymer morphologies in a thermoset showing a) the increase in radius of curvature caused by solubilization of PEO into the uncured epoxy b) block copolymers in epoxy c) the expulsion of PEO blocks from the cured epoxy, which *may* lead to d) the formation of wormlike micelles or e) bulk phase separation

3.3 Methods

Two separate classes of amphiphilic materials were tested to make blowing agent wells in epoxy. The first class was a perfluorinated alkane segment with a poly(ethylene oxide) segment, the second were non fluorinated materials, with either a poly(ethylene) or an oleophilic poly(ether) segment with a poly(ethylene oxide segment). These two classes of materials are considered separately.

3.3.1 Methods: fluorinated amphiphiles

Two fluorinated surfactants were investigated, Zonyl FSN-100 and FSO-100, FSO-100 which are comprised of a perfluorinated alkane block 1-7 repeat units long and an ethyl ether block, 0-15 repeat units long and FSN-100 is comprised of a perfluorinated alkane block 2-18 repeat units long and an ethyl ether block, 0-25 repeat units long, the chemical formula is shown in Fig. 3.9a. FSN-100 was the main focus of these studies. The thermoset was an epoxy, bisphenol-F diglycidyl ether, shown in Fig. 3.9b, (BFDGE) PY306 (Huntsman, The Woodlands, TX) and the curing agent was dimethyltoluene diamine, shown in Fig. 3.9c (DETDA) Ethacure-100 (Albemarle, Baton Rouge, LA). All materials were used as received, without further purification.

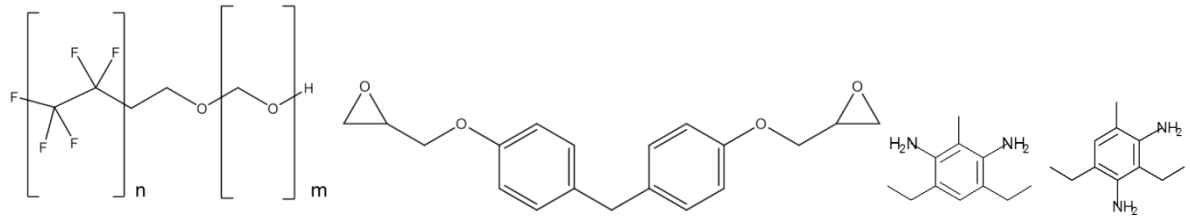

(a) (b) (c)

Figure 3.9. Molecular structure of a) FSN and FSO, b) bisphenol-F diglycidyl ether, and c) dimethyltoluene diamine

Varying concentrations of FSN and FSO were mixed with PY306 using a magnetic stirrer with gentle heating. In cured samples, a stoichiometric amount of DETDA was mixed with a magnetic stirrer at room temperature. The resin was cured in rectangular silicon molds with dimensions of 18 x 4 x 4 mm at 120°C for 2 hours and post cured at 185°C for 2 hours in a convection oven (model 825F, Fisher Scientific, Hampton, NH). Prior to curing the molds were placed in the oven for 1 hour or more at 185°C to remove any adsorbed or absorbed gas and water vapor, to prevent the formation of large bubbles in the samples. Some samples were exposed to 7.8 atm octafluoropropane or varying pressures of CO_2 for 16 hours in a stainless steel pressure vessel (model 4768, Parr Instrument Company, Moline, IL), shown in Fig 3.10. The pressure vessel was wrapped with a fiberglass and resistance wire heater, which was controlled with LabView software on a PC with a LabView TC01 thermocouple USB input and a USB-6009 I/O interface, switching a solid-state relay (5 V DC/120 V AC). By heating the pressure vessel, it was possible to cure the samples without reducing the applied pressure.

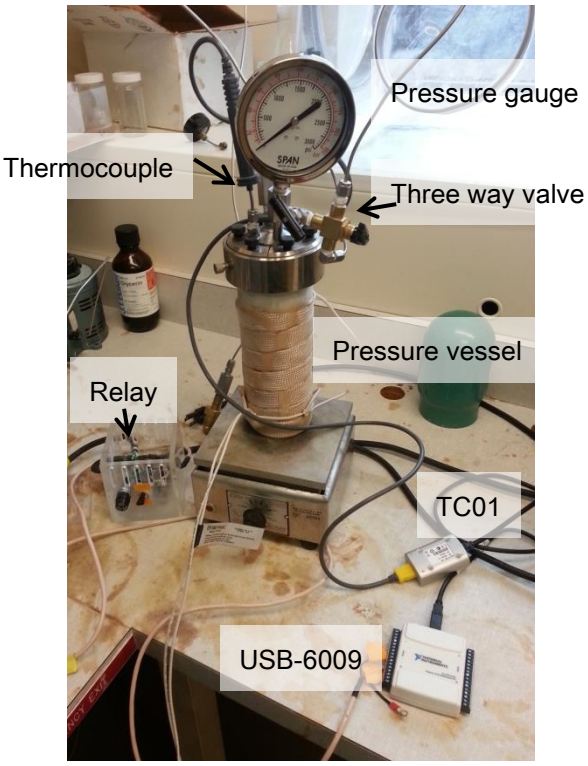

Figure 3.10. The pressure vessel and ancillary components to control the temperature and pressure

The critical micelle concentration of FSN-100 in PY306 at 44°C was determined by surface tension measurements using a platinized Wilhelmy plate using a tensiometer (K12, Krüss USA, Charlotte, NC).

As the epoxy cures the chemical composition of the resin changes, motivating the use of small angle x-ray scattering (SAXSess, Anton Paar USA, Ashland, VA), shown in Fig. 3.11, to track the morphology as a function of cure. A Cu-K_α x-ray source was used, which generated x-rays with a wavelength of 15 Å. The samples were held in quartz capillary tubes. The scattered x-rays were detected with imaging plates (Fuji, Greenwood, SC) which were scanned with a drum scanner (Pelkin Elmer Cyclone, Covina, CA). The scattering profiles PY306 and PY306 with DETDA, with no FSN or FSO, were measured first. SAXS measurements were taken as

the amount of FSN-100 was varied from 0.1 – 5 wt% in PY306 (with no curing agent), at 25°C, for the 5 wt% sample the temperature was varied from 25°C to 60°C. SAXS measurements were also taken on a sample with 5 wt% FSN-100 in a stoichiometric amount of PY306 and DETDA as the temperature was increased from 22°C to 120°C and while the sample was cured at 120°C for two hours.

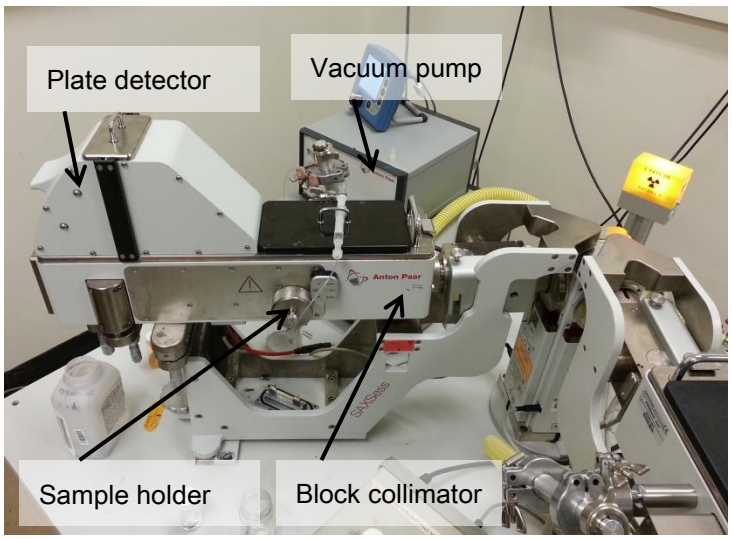

Figure 3.11. A photograph of the SAXS instrument

The morphology following complete cure was determined with atomic force microscopy (AFM) (Autoprobe, Park Scientific Instruments, Santa Clara, CA) in contact mode and scanning electron microscopy (SEM) (JEOL 7000, Tokyo, Japan) of the fractured surface. For SEM the surfaces were sputter coated with a palladium-gold blend to render the surface conductive, to prevent charging.

3.3.2 Methods: non-fluorinated block-copolymers

Three non-fluorinated amphiphilic block copolymers were also tested, polyethylene-block-poly(ethylene oxide) (PE-PEO) (Aldrich, St Louis, MO) M_n: ~1,400 g/mol with each

block having an approximately equal mass fraction, shown in Fig. 3.12a, poly(ethylene oxide)-block-poly(propylene oxide)-block-poly(ethylene oxide) (PEO-PPO-PEO) Pluronic F38 (BASF, Ludwigshafen, Germany) M_w: 4,700 g/mol 80 wt% PEO, shown in Fig. 3.12b, and Fortegra 102 (Dow Corning, Midland, MI). The exact composition of Fortegra 102 is a trade secret, but it is likely poly(ethylene oxide)-block-poly(propylene oxide), shown in Fig. 3.12c, or poly(butylene oxide) block-copolymer, shown in Fig. 3.12d.

1 wt% PE-PEO was mixed into PY306 with a magnetic mixer at 100°C in, the temperature was reduced to 60°C and a stoichiometric amount of DETDA was added. In some cases, various concentrations of pentane and tetradecane were added and gently mixed. These mixtures were cured at temperatures between 85°C and 120°C. 1 wt% Pluronic F38 was added to PY306 with a stoichiometric amount of N-aminoethyl-piperazine, Ancamine AEP (Air Products and Chemicals, Allentown, PA), shown in Fig. 3.12e, with a magnetic mixer, at room temperature. Samples were prepared with and without 5 wt% hexane. The mixture was allowed to cure at room temperature overnight.

5 wt% of the Fortegra 102 block-copolymer was added to BADGE epoxy EP-828 (Miller-Stephenson, Danbury, CT), shown in Fig. 3.9f, and mixed at 75°C. A stoichiometric amount of m-phenylenediamine (mPDA) (Sigma-Aldrich, St. Louis, MI), shown in Fig. 3.12g, and was also mixed at 75°C. The mixture was cooled to room temperature and 5 wt% heptane was added first my hand mixing, then by mixing in a dual asymmetric centrifugal mixer, (DAC 150.1, FlackTek, Landrum, SC) for 10 min at 3,500 RPM. The samples were cured at room temperature for 10 days, followed by 75°C for 2 hours then 125°C for 2 hours.

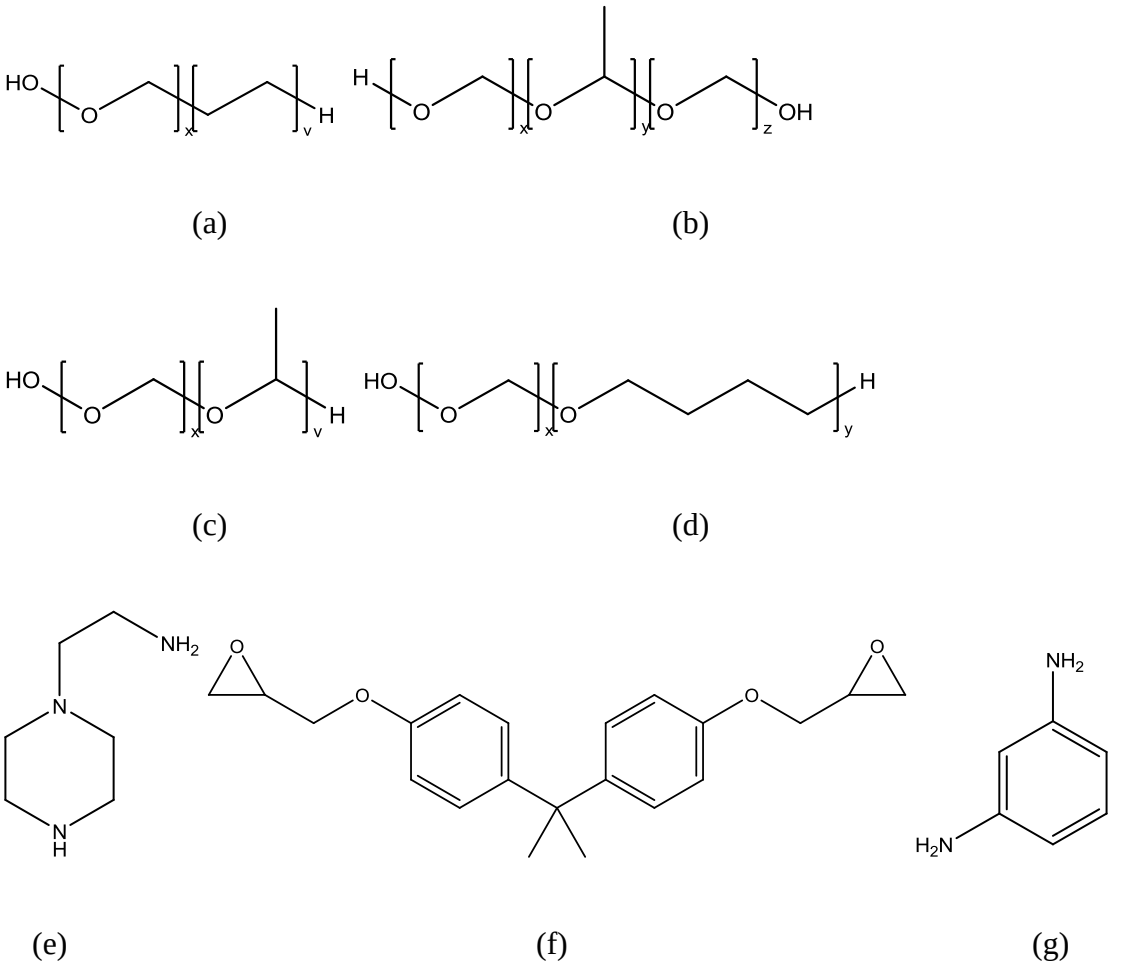

Figure 3.12. The chemical structures for a) poly(ethylene oxide)-*block*-poly(ethylene), b) Pluronic F38, c) poly(ethylene oxide)-*block*-poly(propylene oxide), d) poly(ethylene oxide)-*block*-poly(butylene oxide), e) Ancamine AEP, f) EP-828 BADGE epoxy, and g) m-phenylene diamine

The morphology of the samples was determined after curing by imaging a fracture surface with SEM and AFM (EasyScan, Nanosurf, Woburn, MA).

3.4 Results and discussions

3.4.1 Fluorinated amphiphiles in epoxy

It was concluded that PEO would be the best candidate for the head group of the amphiphile. For the initial study, the other block was chosen to be a perfluorinated alkane

because a perfluorinated micelle core would preferentially absorb CO_2 and perfluorinated, short alkanes, such as octafluoropropane. There are a limited number of commercially available materials that meet these criteria, included Zonyl FSN and FSO.

The first step in making void lightened thermosets using blowing agent wells is the formation and characterization of the blowing agent wells. One of the most important properties of this system is the critical micelle concentration, or CMC. The CMC can be determined by measuring the change in surface tension with change in concentration. An abrupt change in the slope of the surface tension versus concentration curve is often indicative of a CMC where further addition of the amphiphile leads to formation of more micelles, instead of adsorbing to liquid-air and liquid-solid interfaces. The surface tension versus concentration in PY306 at 44°C curve is shown in Fig. 3.13.

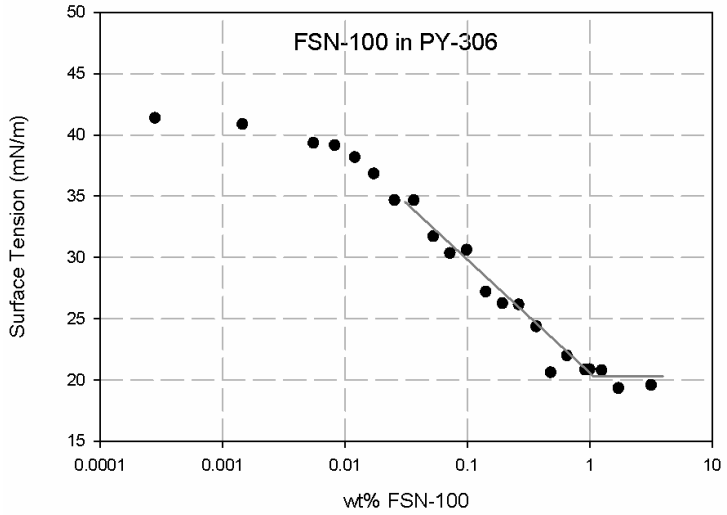

Figure 3.13. The change in surface tension of PY-306 as a function of FSN-100 concentration, where the point of intersection of the grey lines indicates what may be CMC at 1 wt%

The significant change in slope at 1.0 wt% may be indicative of the CMC of the system. 1.0 wt% would be a very high CMC in aqueous systems, but in other systems with a BADGE

continuous phase with block-copolymer the CMC was observed to be very high, often above 5 wt%. An elevated temperature was used because it was observed that at low concentrations, below the CMC, the FSN was insoluble. Thus it was necessary to increase the temperature to increase the solubility above the CMC. The point at which the solubility of a surfactant is equal to the CMC is the Krafft point. To find the approximate temperature at the Krafft point a 1.25 wt% of FSN was mixed into PY306 at 60°C, then allowed to cool to 22°C, then slowly heated in a water bath. At room temperature the mixture was turbid and yellow, when heated to 40°C the solution was clear suggesting dissolution. Bright field micrographs were taken at nearly 50°C and at 22°C, shown in Fig. 3.14. Fig 3.14a shows a solution that is largely free of structures large enough to be resolved with light microscopy. A heated stage was not used, and thus rapid cooling would occur, causing the crystallization of some FSN. When the solution is allowed to cool for several days, the FSN crystallizes into rod like structures typically ~2 μm by 4 – 8 μm, shown in Fig. 3.14b.

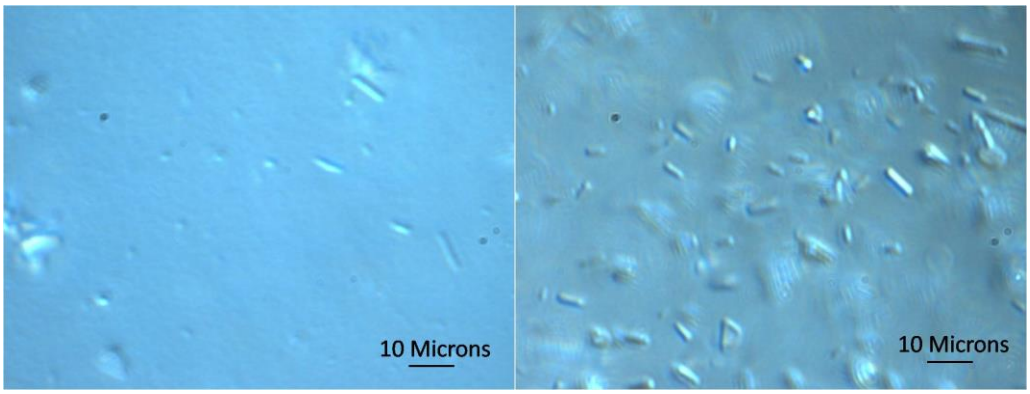

Figure 3.14. A micrograph of 1.24 wt% FSN-100 in PY-306 a) immediately after taking out of a 50°C water bath and b) several days since being heated

In order to better understand the system, small angle x-ray scattering (SAXS) measurements were performed on FSN-100 with PY306 and stoichiometric amounts of PY306 and DETDA at varying concentrations and temperatures.

SAXS is a scattering technique where columnated, monochromatic x-rays pass through a sample causing the electrons to resonate with the electrical field of x-rays, emitting coherent secondary x-rays, with a wavelength equal to that of the incident x-rays. These secondary x-rays interfere constructively and destructively, generating a spatially non-uniform distribution of x-rays. Here, the x-ray beam is line columnated and directed through the sample. The majority of the x-rays pass through the sample, without scattering, which are stopped with a beam blocker. The scattered x-rays bombard a photographic plate, generating a distribution of intensity, $I(\theta)$ as a function of scattering angle, relative to the transmitted beam, $\theta = 0$. From knowledge of this distribution in intensities, significant information can be gathered about shape, size, size distribution, and other structural information for structures between 1 nm and typically 150 nm. X-ray scattering is dependent on a difference in *scattering length density* (SLD), which is the number of atoms per unit volume, multiplied by the constant scattering length of a single electron. Thus, if there is sufficient electron density heterogeneity between the structures of interest and the continuous phase or solvent, analogous to a refractive index mismatch in light scattering. This requirement is satisfied if micelles form, as there would be perfluorinated alkane core, having a significantly higher electron density than the epoxy and the PEO shell.

For the purpose of analysis scattering data are considered as a function of intensity versus the scattering wave vector, q,

$$q = \frac{4\pi}{\lambda} \sin \frac{\theta}{2} \tag{3.6}$$

The scattering data, as a function of q the scattering vector, is shown in Fig. 3.15.

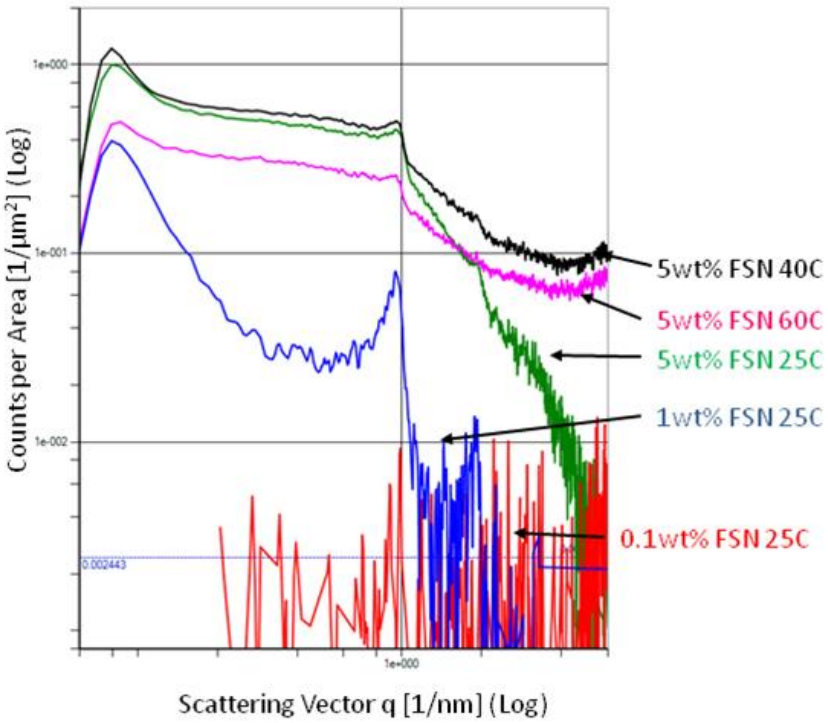

Figure 3.15. SAXS data for 0.1, 1 and 5 wt% at 25°C and 5 wt% at 25, 40 and 60°C

At 0.1 wt% there is very little scattering indicating that there are no ordered structures present. At 1 wt% the shape of the slope and the peak at $q \approx 0.95$ nm^{-1} with the peak at $q \approx 1.9$ nm^{-1} are indicative of an ordered lamellar structure with an average spacing of 6 nm, perhaps the nanostructure of the crystals seen in Fig. 3.14. At 5 wt% at 25°C the linear region below $q =$ 0.95 nm^{-1} is indicative of micelles, additionally, the peaks indicative of a lamellar structure are still present, although less pronounced. This implies that there are both micelles and lamella structures present. Interestingly, the data for 1 and 5 wt% suggest that a lamellar phase forms at concentrations lower than the CMC, which is not generally the case. As the temperature is increased to 40 and 60°C the peaks indicative of the lamellar structure become less pronounced suggesting the lamellar structure is breaking down. This agrees with bright field microscopy and

qualitative observation; as the mixture is warmed to 60°C it transitions from green tinted and cloudy to yellow and clear.

Another SAXS study was performed using PY306 with DETDA with 5 wt% FSN-100 to determine if the curing agent had any effect on micellization and to investigate, *in situ*, effects of curing on the system, the scattering data are shown in Fig. 3.16. As the epoxy cures the FSN-100 becomes less soluble.

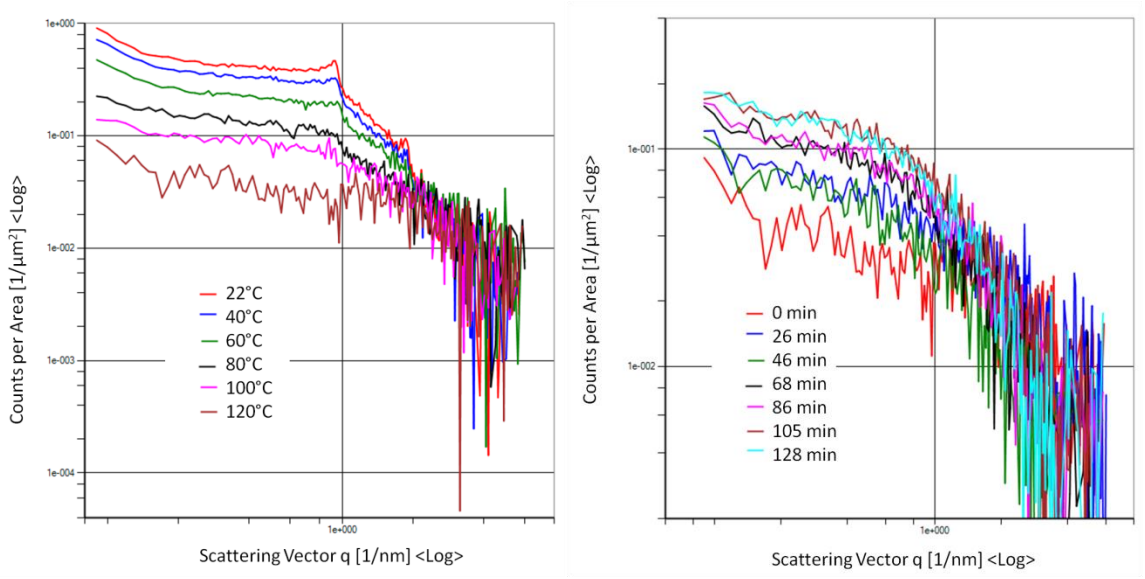

(a) (b)

Figure 3.16. SAXS of 5 wt% FSN in epoxy samples with a) increasing temperature and b) increasing degree of cure

A scattering peak seen at low temperatures at q = 0.94 nm^{-1} corresponds to a lamellar phase from undissolved bulk crystalized regions of FSN-100, identical to the system without Ethaure-100. This peak gradually lessens as the temperatures increases and is not identifiable at temperatures of 80°C and above, indicative of complete melting. At 120°C the existence of micelles is not apparent at time zero; the times correspond to the start of the 15 min exposure.

However, as the cure progresses the scattering increases and takes on a shape that plateaus at low *q*, suggesting the formation of micelles.

These SAXS data suggest that initially at high temperatures micelles are not present. This is not entirely surprising; FSN is a relatively small molecule, compared to the block-copolymers that have been used to make micelles and vesicles in epoxies in other studies and is probably completely dissolved as monomers at high temperatures. However, as the cross link density increases, the solubility of the FSN is decreased, and the formation of micelles becomes thermodynamically favorable. The large 0.5 μm domains seen in SEM images, shown below, were too large and too disordered to have any effect on the SAXS scattering data.

From the SAXS and surface tension data and the microscopy images, it was determined that at about 60°C, prior to curing, micelles or micelle-like structures were likely present. In order to determine if the micelles remain following curing, samples were completely cured, fractured then imaged with SEM and AFM. The SEM micrographs for FSN-100 concentrations between 1 and 10 wt% are shown in Fig. 3.17 and an AFM micrograph of a 5 wt% sample is shown in Fig. 3.18.

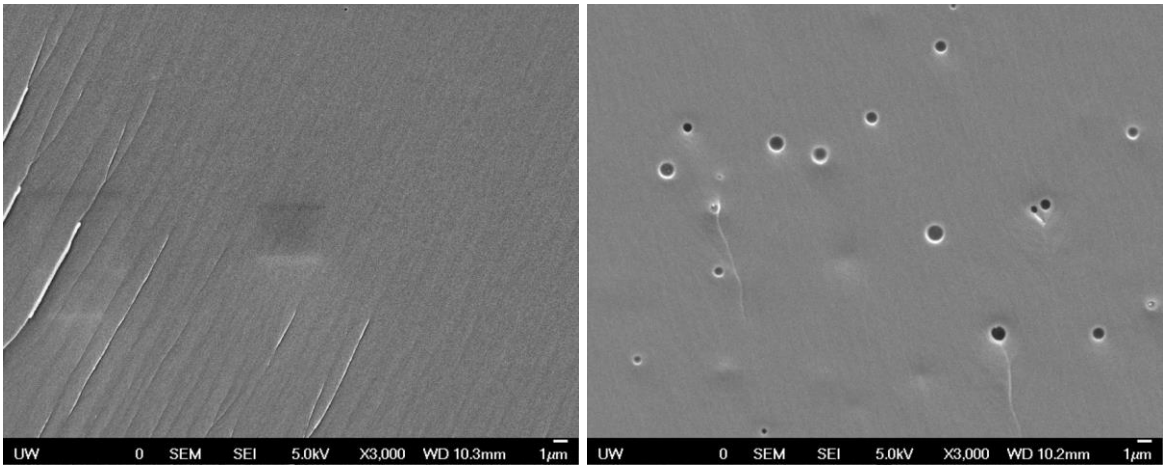

(a) (b)

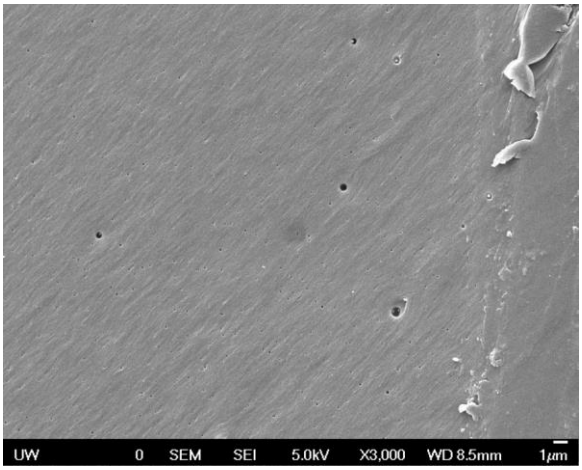

(c)

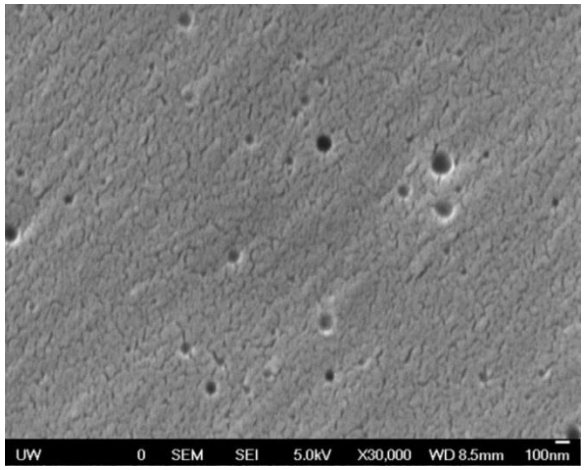

(d)

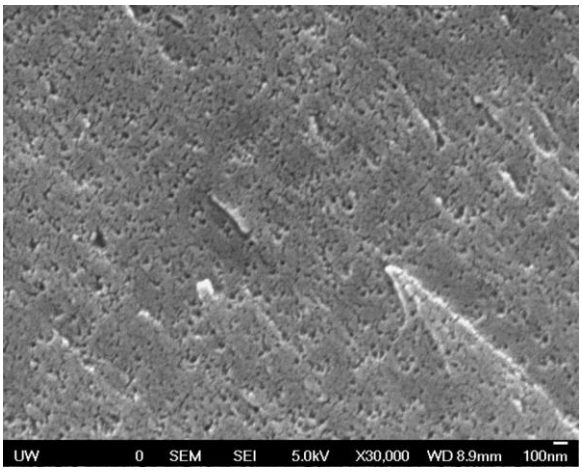

(e)

Figure 5.17. PY306/Ethacure-100 made with a) 1 wt% FSN, b) 3 wt% FSN, c) and d) 5 wt% FSN, and e) 10 wt% FSN

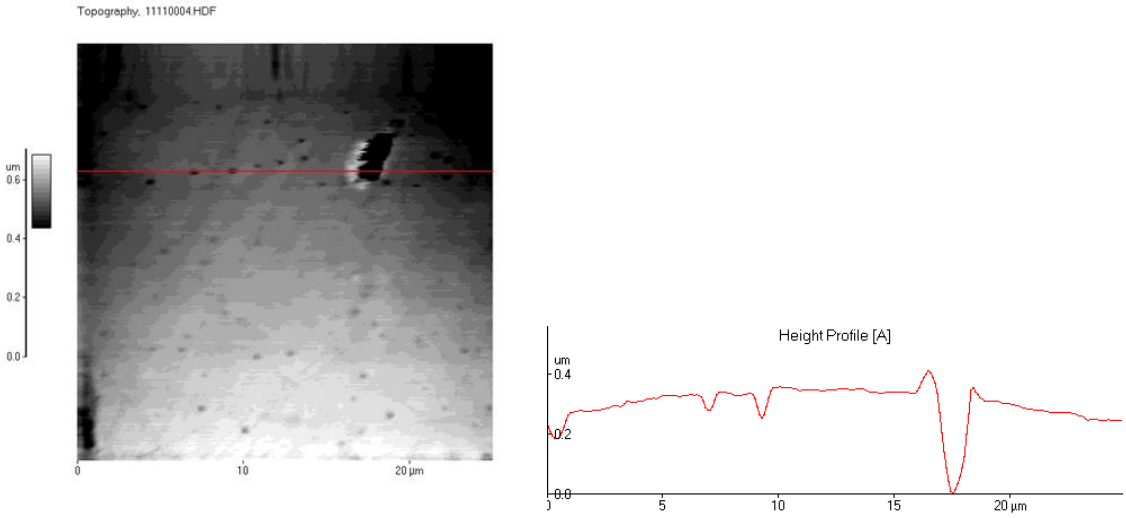

Figure 3.18. Topology of a fractured and polished surface of epoxy with FSN, the red line indicating the location of the height profile, shown below the image

At low concentrations, 1 wt% FSN and less, the amphiphile remains miscible in the epoxy, even after the cure is completed. At higher magnifications there was no indication of nanostructures. At a concentration of 3 wt% FSN, there is phase separation, generating spherical domains 0.5 – 1 µm in diameter. At 5wt% FSN a bimodal distribution of the discontinuous phase formed, with typical diameters of less than 100 nm and 0.5 µm. At higher concentrations, 10 wt% FSN, 30 nm spherical structures remained after the cure. These small structures were likely FSN micelles swollen with low molecular weight perfluorinated FSN fractions.

In another set of samples, the low molecular fractions of FSN were removed by heating to 60°C, applying vacuum, 0.1 atm pressure absolute, and stirring for 1 hour, the amount of time necessary for the FSN to stop boiling. This process removed 3.4 wt% FSN. This "degassed" FSN was used to make another set of samples, similar to those shown in Fig. 3.17. The results are shown in Fig. 3.19.

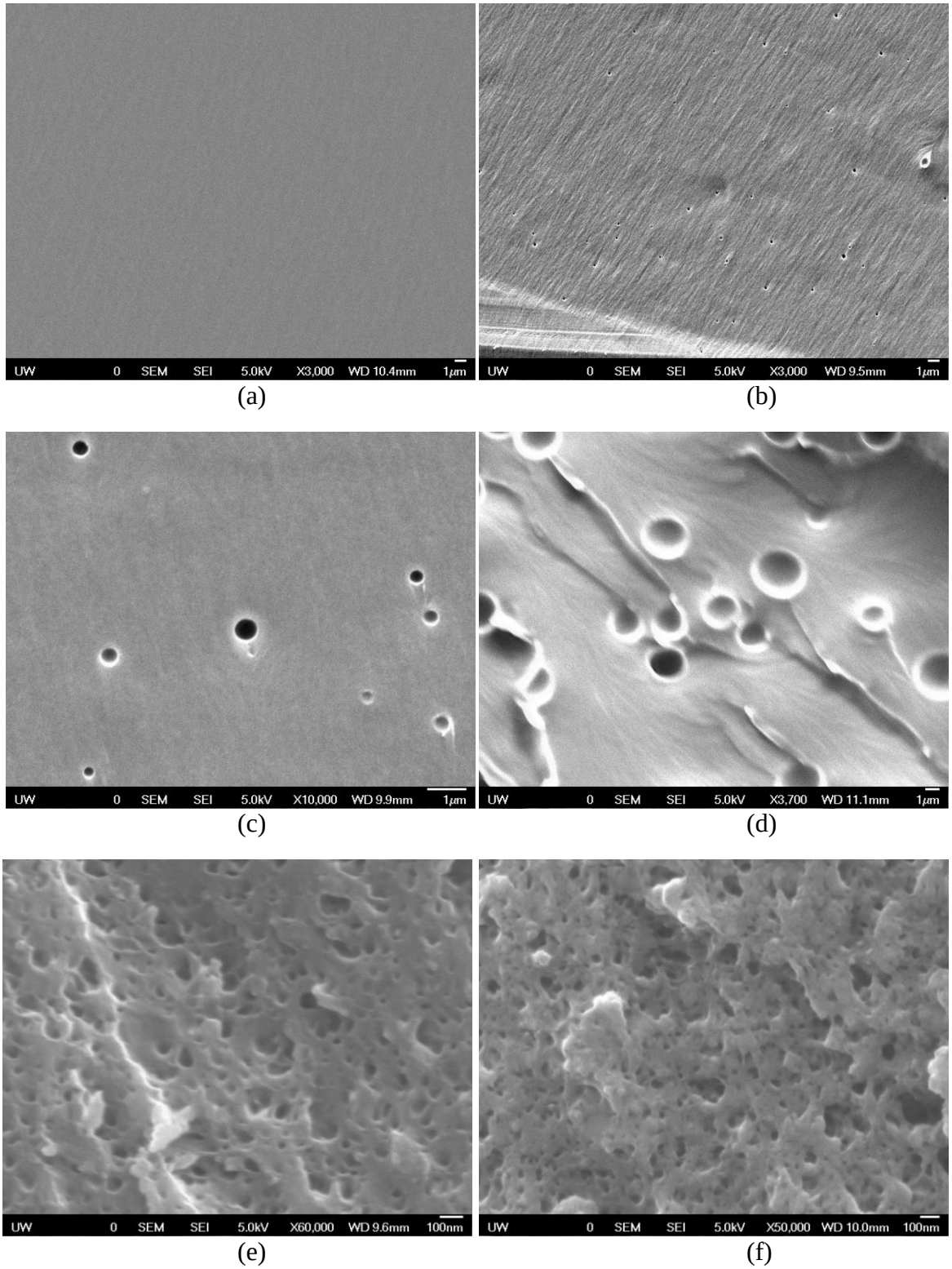

Figure 3.19. PY306/Ethacure-100 made with a) 1 wt%, b) 3 wt%, c) 5 wt%, d) 10 wt% e) 15 wt%, and f) 20 wt% *degassed* FSN

Degassing the FSN appeared to have significant effects on the morphology of the cured samples. 1 wt% FSN remained miscible, at 3 wt% the FSN domains were much smaller, about 200 nm. With 5 wt% degassed FSN, there was a monomodal distribution, with a diameter size of about 200 nm. The most striking difference between the as received FSN and the degassed FSN was observed at 10 wt%, with the degassed FSN the average discontinuous domain size was 2.5 μm. The reason for this change in domain size is not immediately evident. As the epoxy is cured any micelles present go through a meso-stable state where the solubility of the PEO groups is small, but the diffusion rate of amphiphile is low. Slight perturbations in this meso-stable state can cause bulk phase separation, seen in Fig. 19d. When the concentration is increased further, to 15 and 20 wt% degassed FSN, small domains, between 10 and 100 nm were seen.

For reasons discussed above, C_3F_8 was chosen as a potential blowing agent. To determine if it affected the morphology, samples were prepared with degassed FSN, in the same manner as the samples described above, however, the specimens were placed in a pressure vessel and exposed to 8.8 atm C_3F_8 for 16 hours at 60°C. An elevated temperature was used to dissolve the large crystalline FSN phase observed with optical microscopy and SAXS. The specimens were then cured in the pressure vessel, without reducing the pressure. SEM images were taken near the specimen surface, where C_3F_8 would have diffused into the liquid epoxy monomer. The results are shown in Fig. 3.20.

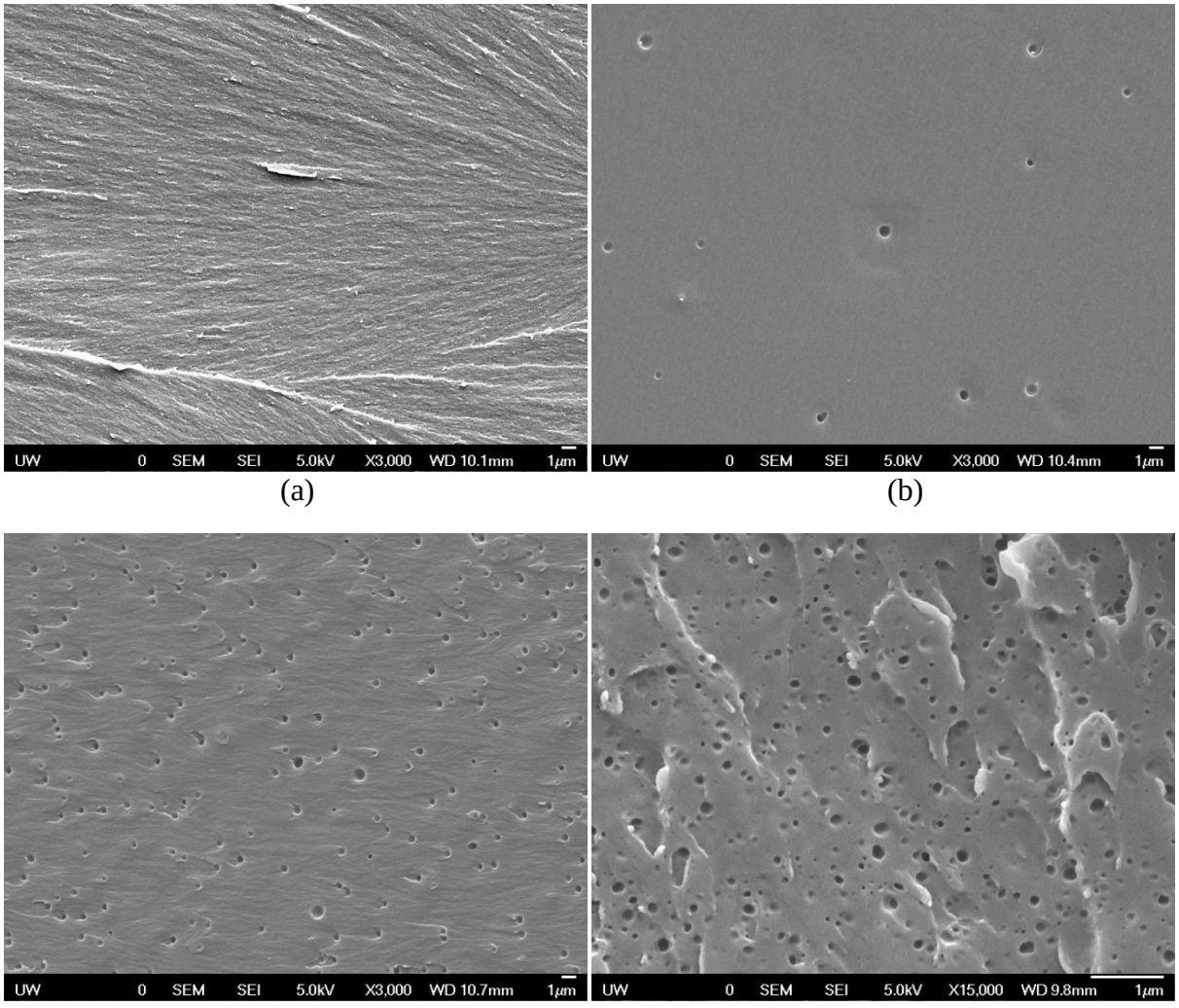

Figure 3.20. PY306/Ethacure-100 made with a) 1 wt%, b) 3 wt%, c) 5 wt%, and d) 10 wt% *degassed* FSN and exposed to 8.8 atm C_3F_8

1 wt% FSN had no observable change in morphology from the pure epoxy resin system. 3 and 5 wt% FSN generated discontinuous spherical domains with a typical size of 300 nm. A broad distribution of diameters, from 50 to 150 nm, was seen on the fractured surface of the sample made with 10 wt% degassed FSN with C_3F_8.

The phase behavior of FSN in BFDGE epoxy resin with DETDA curing agent was dynamic, changing as the resin system was heated and cured. Additionally, using the surfactant FSN introduced a broad range of compounds, including low molecular weight perfluorinated

alkanes and short amphiphilic oligomers. Based on the SAXS data and SEM observations of the cured systems some general conclusions about the system can be made. At concentrations of 1 wt% FSN and less it remains miscible in the epoxy resin, even after the epoxy resin cures. At higher concentrations there is phase separation. As the epoxy resin cures, the molecular weight increases until the entire specimen is crosslinked, and can be considered a single macromolecule. This increase in molecular weight decreases the molecular interaction and miscibility of dissolved compounds. This phenomenon, chemically induced phase separation, is well understood and frequently employed to make micro- domains of liquid rubber for toughening of thermosets. The size of domains is a product of composition, miscibility, viscosity, and diffusion rate. In samples with micron sized discontinuous phases, the heterogeneity was caused by phase separation, not by the self-assembly of amphiphile into micelles. Samples with nano-sized domains were likely the product of amphiphile self-assembly into micelles, however, the thermodynamically unstable nature of the systems limited reproducibility.

3.4.2 PE-PEO and PEO-PPO-PEO in epoxy

The PEO block of FSN did not have a high enough molecular weight to prevent phase separation as the cure progressed. Given an apparent lack of any commercially available higher molecular weight analogs to FSN, a non-fluorinated block-copolymer was tested. PE-PEO, was chosen because Guo et al. observed that it formed micelles in BADGE epoxy resin cured with methylenedianiline (MDA) at 120°C [64]. In an attempt to reproduce their results, a system with similar composition was made using 1 wt% PE-PEO in a stoichiometric ratio of BADGE epoxy (PY-306, Huntsman, Salt Lake City, UT) cured with DETDA at 120°C. From SEM observations it was seen that in *most* cases ~1 μm spherical domains of PE-PEO were formed, shown in Fig. 3.21. When cured at 105°C 500 nm diameter worm like structures were observed.

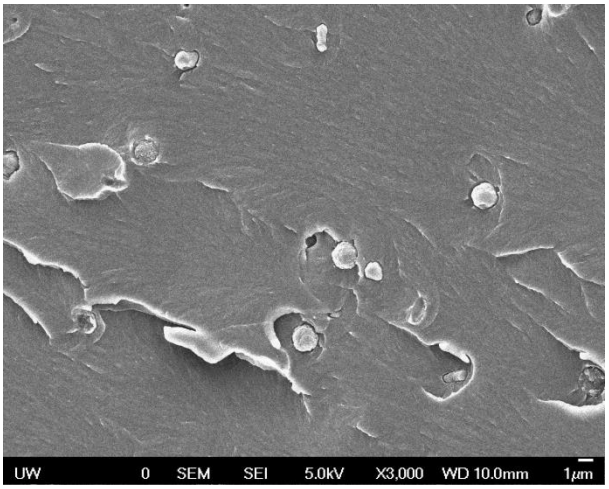

Figure 3.21. Spherical domains of bulk PE-PEO in cured epoxy

However, when the PE-PEO mixture was combined with 2 wt% pentane and cured at 120°C, sub 100 nm semi-spherical features were seen on the facture surface, showing in Fig. 3.22. These were likely swollen PE-PEO micelles.

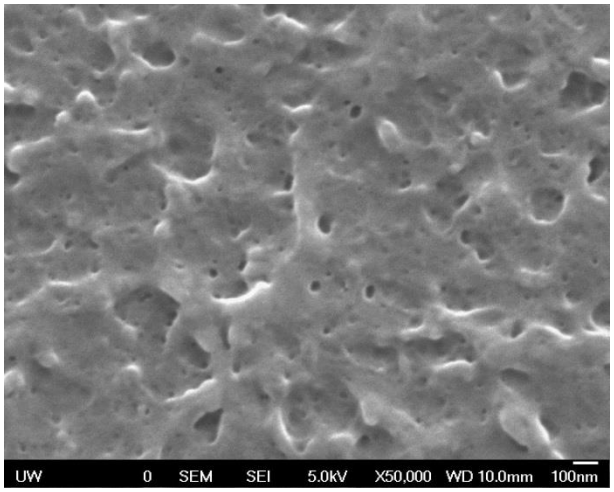

Figure 3.22. The fracture surface of a sample made with PY306, DETDA, 1 wt% PE-PEO and 2 wt% pentane cured at 120°C, the semi-spherical structures are likely fractured swollen PE-PEO micelles

Like the systems with FSN, consistency of generating nano structures was low. The bulk densities of poly(ethylene oxide), MW = 700 and pentacontane (C50 alkane) MW = 703 are 1.13

and 0.824 g/cm^2 respectively, given the reported 50/50 *mass* fraction of the segments of the block copolymer, the calculated PEO volume fraction is 0.42. Based on the published literature, this is approaching the minimum volume fraction of PEO necessary to generate micelles in epoxy resins. Thus, slight perturbations in the system are sufficient to cause phase separation during cure.

Experiments were also done with Pluronic F38 to determine its ability to be a blowing agent well. F38 is a triblock copolymer with a MW of 4,700 g/mol and is comprised of 80 wt% PEO, ensuring miscibility throughout the cure. When mixed with PY306 and Ancamine AEP the mixture was clear and strongly scattered laser light, suggesting the formation of micelles. When cured at room temperature overnight, there was no bulk phase separation, as determined by SEM imaging of the fractured surface. SEM imaging of the fracture surface could not be used to determine the presence of micelles, however. When 5 wt% hexane was incorporated into the mixture an emulsion was formed, as seen in Fig. 3.23.

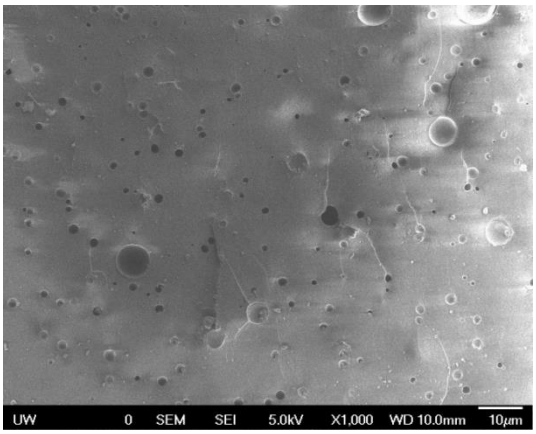

Figure 3.23. The fracture surface of a sample made with PY306, Ancamine AEP, 1 wt% Pluronic F38 and 5 wt% hexane cured at room temperature, the spherical structures are likely emulsified hexane

This sample was produced with gentle mixing with a magnetic stir bar. It is possible that the formation of the emulsion was simply the product of poor mixing. This sample was

produced prior to the acquisition of the FlackTek speed mixer, which generates significant amounts of shear and would be better suited for mixing these samples.

3.4.3 Fortegra 102 blowing agent wells

Fortegra 102 is a commercially available self-assembling block copolymer for toughening resin systems. Interestingly, when cured at elevated temperatures the material would phase separate, necessitating a partial room temperature cure to increase the viscosity. The post cured sample was fractured with a razor blade at room temperature and sputter coated for 50 s for SEM. Another sample was fractured and imaged with a Nanosurf AFM in contact mode with a new tip. Fig. 3.24 shows the SEM micrograph, where the dark circles are presumably fractured heptane swollen micelles. Fig. 3.25 shows the AFM micrographs of the epoxy without heptane but with Fortegra 102 and micrographs of the resin with heptane *and* Fortegra 102 at two different magnifications.

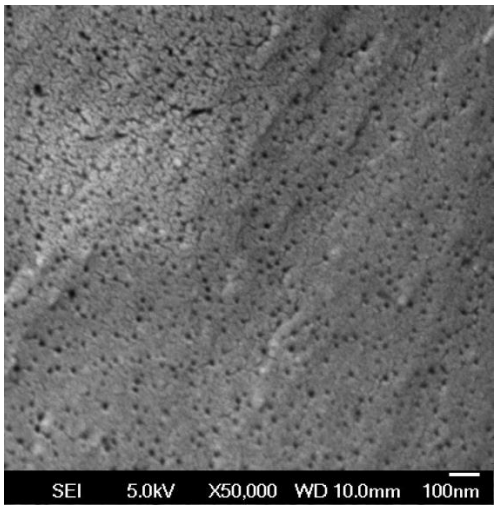

Figure 3.24. SEM micrograph of 5 wt% heptane, 5 wt% block copolymer in EP-828/mPDA

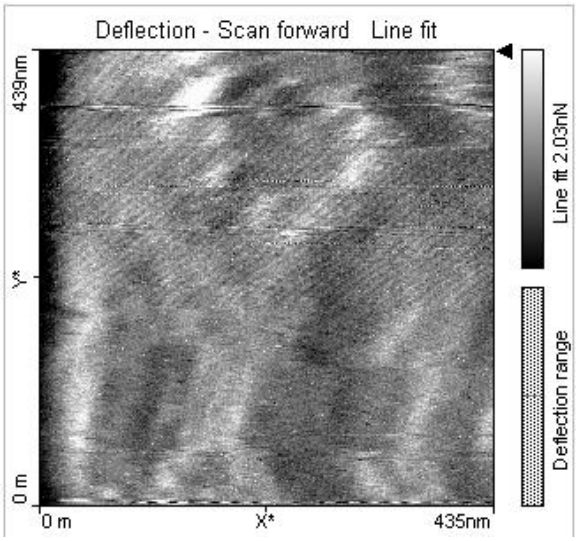

(a)

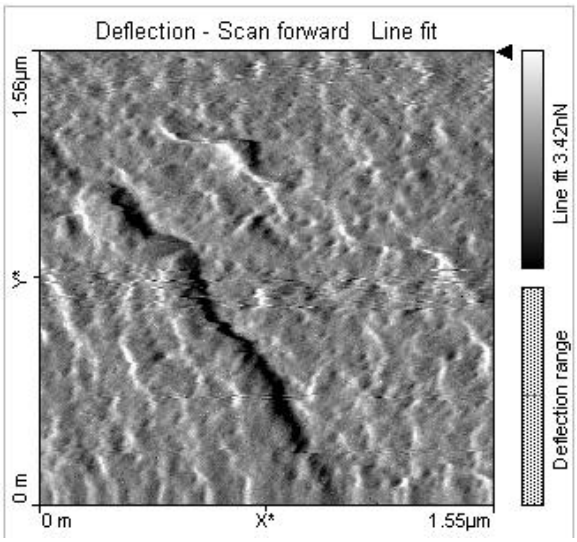

(b)

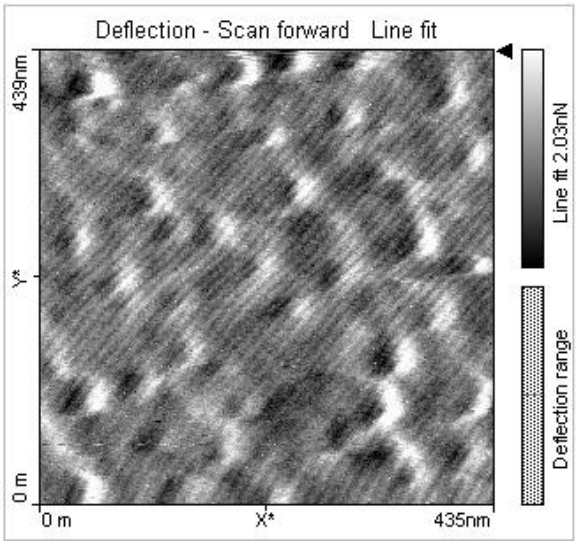

(c)

Figure 3.25. AFM micrograph of 5 wt% block copolymer in EP-828/mPDA with a) *no* heptane, b) and c) with 5 wt% heptane

When there is no heptane, no topographical variation exists, as would be expected. The non-swollen micelle size is too small to be imaged after sputter coating. But when heptane is added hemispherical holes are present at the fracture surface, left by fractured swollen micelles. Based on image analysis of the AFM micrograph, the fractured cross sections are between 20 and 30 nm in diameter.

It was possible that the very consistent domain size seen here, and not in other systems, was from using the Flacktek planetary mixer which generated higher shear forces in the mixture than what was accomplished with a magnetic mixer.

3.5 Conclusions

It was postulated that a thermoset with spherical, non-interacting nano-sized gas filled bubbles or voids (a *kugelschaum*) could be used as a light weight matrix material for a continuous fiber composite. A literature review was performed to find potential methods for generating such a material. It was concluded that self-assembling block copolymers could be used as blowing agent wells. To take advantage of the very low solubility demonstrated by fluorinated materials in many solvents a fluorinated non-ionic surfactant, Zonyl FSN was initially studied. For all curing conditions used, phase separation was observed, because the relative volume of the PEO segment was not large enough to provide sufficient solubility as the cure progressed.

Other, non-fluorinated block-copolymers were used, including poly(ethylene)-*block*-poly(ethylene oxide) (PE-PEO), poly(ethylene oxide)-*block*-poly(propylene oxide)-*block*-poly(ethylene oxide), and Fortegra 102. It was possible to make swollen micelles with both PE-PEO and Fortegra 102 with careful control of the cure conditions.

However, it remains to be seen if this method can be used to generate *hollow* sub 100 nm spherical domains. The alkanes used have relatively high vapor pressures, making it difficult to achieve sufficient supersaturation to cause a phase change, however, lower molecular weight gaseous alkanes could be used.

References

[1] Agarwal BD, Broutman LJ, Chandrashekhara K. Analysis and Performance of Fiber Composites. 3rd ed. Wiley; 2006.

[2] Ramanathan T, Muthumanickam MA, Subramanian K. Study on the effect of loading rate on flexural strength of glass/polyester composites as a function of span-to-depth ratio and fiber volume fraction. Mater Manuf Process 2000;15:845–52.

[3] Frisch KC, Saunders JH. Plastic foams. New York: M. Dekker; 1972.

[4] Koopman M, Chawla KK, Carlisle KB, Gladysz GM. Microstructural failure modes in three-phase glass syntactic foams. J Mater Sci 2006;41:4009–14.

[5] Shankar R, Sankaran S. Short-beam three-point bend test study in syntactic foam. Part III: Effects of interface modification on strength and fractographic features. J Appl Polym Sci 2005;98:687–93.

[6] Cardoso RJ, Shukla A, Bose A. Effect of particle size and surface treatment on constitutive properties of polyester-cenosphere composites. J Mater Sci 2002;37:603–13.

[7] Wouterson EM, Boey FYC, Hu X, Wong SC. Specific properties and fracture toughness of syntactic foam: Effect of foam microstructures. Compos Sci Technol 2005;65:1840–50.

[8] Gupta N, Woldesenbet E. Microballoon wall thickness effects on properties of syntactic foams. J Cell Plast 2004;40:461–80.

[9] Peter SL, Woldesenbet E. Nanoclay and Microballoons Wall Thickness Effect on Dynamic Properties of Syntactic Foam. J Eng Mater Technol 2009;131:021007.

[10] Porfiri M, Gupta N. Effect of volume fraction and wall thickness on the elastic properties of hollow particle filled composites. Compos Part B Eng 2009;40:166–73.

[11] Huang JS, Gibson LJ. Elastic moduli of a composite of hollow spheres in a matrix. J Mech Phys Solids 1993;41:55–75.

[12] Kishore, Shankar R, Sankaran S. Effects of microballoons' size and content in epoxy on compressive strength and modulus. J Mater Sci 2006;41:7459–65.

[13] Kishore, Shankar R, Sankaran S. Short-beam three-point bend tests in syntactic foams. Part II: Effect of microballoons content on shear strength. J Appl Polym Sci 2005;98:680–6.

[14] Ying-long Y, Zi-xing L. Modulus prediction and discussion of reinforced syntactic foams with coated hollow spherical inclusions. Appl Math Mech 2004;25:528–35.

[15] Marur PR. Effective elastic moduli of syntactic foams. Mater Lett 2005;59:1954–7.

[16] Zouari R, Benhamida A, Dumontet H. A micromechanical iterative approach for the behavior of polydispersed composites. Int J Solids Struct 2008;45:3139–52.

[17] Cho J, Joshi MS, Sun CT. Effect of inclusion size on mechanical properties of polymeric composites with micro and nano particles. Compos Sci Technol 2006;66:1941–52.

[18] Gupta N, Woldesenbet E. Characterization of flexural properties of syntactic foam core sandwich composites and effect of density variation. J Compos Mater 2005;39:2197–212.

[19] Woldesenbet E, Gupta N, Jerro HD. Effect of microballoon radius ratio on syntactic foam core sandwich composites. J Sandw Struct Mater 2005;7:95–111.

[20] Bardy E, Mollendorf J, Pendergast D. Thermal resistance and compressive strain of underwater aerogel–syntactic foam hybrid insulation at atmospheric and elevated hydrostatic pressure. J Phys Appl Phys 2006;39:1908.

[21] Jhaver R, Tippur H. Processing, compression response and finite element modeling of syntactic foam based interpenetrating phase composite (IPC). Mater Sci Eng A 2009;499:507–17.

[22] Schmidt W, Roessling G. Novel manufacturing process of hollow polymer microspheres. Chem Eng Sci 2006;61:4973–81.
[23] Caruso RA, Susha A, Caruso F. Multilayered titania, silica, and laponite nanoparticle coatings on polystyrene colloidal templates and resulting inorganic hollow spheres. Chem Mater 2001;13:400–9.
[24] Caruso F, Caruso RA, Mohwald H. Nanoengineering of inorganic and hybrid hollow spheres by colloidal templating. Science 1998;282:1111–4.
[25] Zhang Y, Lv F, Ke S, Yu L, Huang H, Chan HLW. Effect of hollow structure and covalent bonding on the mechanical properties of core–shell silica nanoparticles modified poly (methyl acrylate) composites. Mater Chem Phys 2011;129:77–82.
[26] Liu J, Fan F, Feng Z, Zhang L, Bai S, Yang Q, et al. From Hollow Nanosphere to Hollow Microsphere: Mild Buffer Provides Easy Access to Tunable Silica Structure. J Phys Chem C 2008;112:16445–51.
[27] Chen J-F, Ding H-M, Wang J-X, Shao L. Preparation and characterization of porous hollow silica nanoparticles for drug delivery application. Biomaterials 2004;25:723–7.
[28] Lou XW (David), Archer LA, Yang Z. Hollow Micro-/Nanostructures: Synthesis and Applications. Adv Mater 2008;20:3987–4019.
[29] Tamai H, Sumi T, Yasuda H. Preparation and characteristics of fine hollow carbon particles. J Colloid Interface Sci 1996;177:325–8.
[30] Schacht S, Huo Q, VoigtMartin IG, Stucky GD, Schuth F. Oil-water interface templating of mesoporous macroscale structures. Science 1996;273:768–71.
[31] Carlisle KB, Koopman M, Chawla KK, Kulkarni R, Gladysz GM, Lewis M. Microstructure and compressive properties of carbon microballoons. J Mater Sci 2006;41:3987–97.
[32] Fu S-Y, Feng X-Q, Lauke B, Mai Y-W. Effects of particle size, particle/matrix interface adhesion and particle loading on mechanical properties of particulate–polymer composites. Compos Part B Eng 2008;39:933–61.
[33] Zhou Y, White E, Hosur M, Jeelani S. Effect of particle size and weight fraction on the flexural strength and failure mode of TiO2 particles reinforced epoxy. Mater Lett 2010;64:806–9.
[34] Zhao S, Schadler L, Duncan R, Hillborg H, Auletta T. Mechanisms leading to improved mechanical performance in nanoscale alumina filled epoxy. Compos Sci Technol 2008;68:2965–75.
[35] Hutchinson JW. Crack tip shielding by micro-cracking in brittle solids. Acta Metall 1987;35:1605–19.
[36] Kawaguchi T, Pearson RA. The effect of particle–matrix adhesion on the mechanical behavior of glass filled epoxies: Part 1. A study on yield behavior and cohesive strength. Polymer 2003;44:4229–38.
[37] Wouterson EM, Boey FY, Hu X, Wong S-C. Fracture and impact toughness of syntactic foam. J Cell Plast 2004;40:145–54.
[38] Lee J, Yee AF. Inorganic particle toughening I: micro-mechanical deformations in the fracture of glass bead filled epoxies. Polymer 2001;42:577–88.
[39] Gent A, Park B. Failure Processes in Elastomers at or Near a Rigid Spherical Inclusion. J Mater Sci 1984;19:1947–56.
[40] Griffith AA. The Phenomena of Rupture and Flow in Solids. Philos Trans R Soc Lond Ser Contain Pap Math Phys Character 1921;221:163–98.

[41] Ema Y, Ikeya M, Okamoto M. Foam processing and cellular structure of polylactide-based nanocomposites. Polymer 2006;47:5350–9.
[42] Fu J, Naguib HE. Effect of nanoclay on the mechanical properties of PMMA/clay nanocomposite foams. J Cell Plast 2006;42:325–42.
[43] Colton JS, Suh NP. The nucleation of microcellular thermoplastic foam with additives: Part I: Theoretical considerations. Polym Eng Sci 1987;27:485–92.
[44] Zettlemoyer AC. Nucleation,. New York: M. Dekker; 1969.
[45] Becker R, Doring W. Kinetic treatment of germ formation in supersaturated vapour. Ann Phys 1935;24:719–52.
[46] Ham FS. Diffusion-Limited Growth of Precipitate Particles. J Appl Phys 1959;30:1518–25.
[47] Yokoyama H, Sugiyama K. Nanocellular structures in block copolymers with CO2-philic blocks using CO2 as a blowing agent: Crossover from micro- to nanocellular structures with depressurization temperature. Macromolecules 2005;38:10516–22.
[48] Nemoto T, Takagi J, Ohshima M. Nanoscale Cellular Foams from a Poly (propylene)-Rubber Blend. Macromol Mater Eng 2008;293:991–8.
[49] Qingfeng Wu, Park CB, Nanqiao Zhou, Wenli Zhu. Effect of Temperature on Foaming Behaviors of Homo- and Co-polymer Polypropylene/Polydimethylsiloxane Blends with CO2. J Cell Plast 2009;45:303–19.
[50] Nemoto T, Takagi J, Ohshima M. Control of Bubble Size and Location in Nano-/Microscale Cellular Poly (propylene)/Rubber Blend Foams. Macromol Mater Eng 2008;293:574–80.
[51] Luo X, Zheng S, Zhang N, Ma D. Miscibility of epoxy resins/poly (ethylene oxide) blends cured with phthalic anhydride. Polymer 1994;35:2619–23.
[52] Larranaga M, Mondragon I, Riccardi CC. Miscibility and mechanical properties of an amine-cured epoxy resin blended with poly(ethylene oxide). Polym Int 2007;56:426–33.
[53] Schulz MF, Khandpur AK, Bates FS, Almdal K, Mortensen K, Hajduk DA, et al. Phase behavior of polystyrene-poly (2-vinylpyridine) diblock copolymers. Macromolecules 1996;29:2857–67.
[54] Dean JM, Lipic PM, Grubbs RB, Cook RF, Bates FS. Micellar structure and mechanical properties of block copolymer-modified epoxies. J Polym Sci Part B Polym Phys 2001;39:2996–3010.
[55] Lipic PM, Bates FS, Hillmyer MA. Nanostructured thermosets from self-assembled amphiphilic block copolymer/epoxy resin mixtures. J Am Chem Soc 1998;120:8963–70.
[56] Hillmyer MA, Bates FS. Synthesis and characterization of model polyalkane-poly (ethylene oxide) block copolymers. Macromolecules 1996;29:6994–7002.
[57] Hillmyer MA, Lipic PM, Hajduk DA, Almdal K, Bates FS. Self-assembly and polymerization of epoxy resin amphiphilic block copolymer nanocomposites. J Am Chem Soc 1997;119:2749–50.
[58] Wu J, Thio YS, Bates FS. Structure and properties of PBO-PEO diblock copolymer modified epoxy. J Polym Sci Part B Polym Phys 2005;43:1950–65.
[59] Thio YS, Wu J, Bates FS. Epoxy Toughening Using Low Molecular Weight Poly(hexylene oxide)−Poly(ethylene oxide) Diblock Copolymers. Macromolecules 2006;39:7187–9.
[60] Thio YS, Wu J, Bates FS. The Role of inclusion size in toughening of epoxy resins by spherical micelles. J Polym Sci Part B Polym Phys 2009;47:1125–9.

[61] Dean JM, Grubbs RB, Saad W, Cook RF, Bates FS. Mechanical properties of block copolymer vesicle and micelle modified epoxies. J Polym Sci Part B Polym Phys 2003;41:2444–56.
[62] Grubbs RB, Dean JM, Broz ME, Bates FS. Reactive Block Copolymers for Modification of Thermosetting Epoxy. Macromolecules 2000;33:9522–34.
[63] Grubbs RB, Broz ME, Dean JM, Bates FS. Selectively Epoxidized Polyisoprene−Polybutadiene Block Copolymers. Macromolecules 2000;33:2308–10.
[64] Guo QP, Thomann R, Gronski W, Staneva R, Ivanova R, Stuhn B. Nanostructures, semicrytalline morphology, and nanoscale confinement effect on the crystallization kinetics in self-organized block copolymer/thermoset blends. Macromolecules 2003;36:3635–45.

Chapter 4 – Improving fiber-matrix adhesion with functionalized silica nanoparticles

cf. Rutz B.H., and Berg J.C., "Improvement of Interfacial Shear Strength Using Electrostatically Deposited Silica Nanoparticles," *Composites Science and Technology*. Submitted 10/2013.

Summary

In order to achieve the best mechanical properties from a fiber composite, the adhesion between the fiber and matrix must be optimized. This has traditionally been done by modifying the chemistry of the fiber surface, but recently there has been increased interest in *topographical interface modifiers*. In the present study the effect of poly(ethyleneimine) functionalized silica nanoparticles deposited E-glass fibers on the interfacial shear strength (IFSS) between the fiber and an epoxy matrix was determined. The IFSS was measured with the single fiber fragmentation test (SFFT). 26 nm diameter nanoparticles increased the IFSS of sized, desized and (glycidyloxypropyl)trimethoxysilane (GPS) functionalized E-glass fibers 16%, 16%, and 8%, respectively. The IFSS is highly dependent on particle size; 16 nm functionalized particles had little effect on the IFSS, and increasing particle size to 71 and 100 nm led to increasingly poor IFSS values. The nanoparticles were electrostatically deposited with careful control of the volume fraction of nanoparticles, pH, and electrolyte (along with other variables) to achieve dense surface coverage without particle-particle aggregation.

4.1 Introduction

The mechanical properties of continuous fiber reinforced plastics (CFRPs) are dependent not only on the mechanical properties of the fiber and matrix, but also the adhesion between them [1–3]. In the case of glass fibers, the adhesion is improved using silane coupling agents such as (3-glycidyloxypropyl)trimethoxysilane (GPS) and (3-aminopropyl)trimethoxysilane (APS). The use of chemical interphase modifiers has been the subject of extensive research for decades [4].

Instead of modifying the fiber surfaces chemically it is possible to modify them physically by introducing nano-, or possibly micro-, whiskers, carbon nanotubes (CNTs) or particles to the fiber surface. These structural interphase modifiers can increase the mechanical interlock and surface area for bonding, improving the adhesion beyond that which is possible with chemical surface modification. There has been significant interest in growing CNTs on carbon fibers using chemical vapor deposition (CVD) techniques [5–7]. However, the harsh environment of CVD damages carbon fibers, reducing their strength, decreasing composite mechanical properties. Zinc oxide whiskers have been grown on carbon fibers, but under benign reaction conditions that do not degrade the fiber strength [8–10]. These ZnO whiskers improved the IFSS, interlaminar shear strength, and modulus of the systems tested. In another study, the surface roughness on glass fibers was increased with a tetraethylorthosilicate (TEOS)/GPS blend, improving mechanical interlock at the interface [11]. The energy absorption during a microdroplet shear test and the IFSS were increased.

Instead of growing structures on the surface of fibers, it is possible to synthesize interphase modifiers separately and to deposit them on the surface. CNTs were deposited on to carbon fibers using electrophoresis, leading to an increase in interlaminar shear strength [12].

CNTs treated with poly(ethyleneimine) (PEI) were electrostatically deposited on to carbon fibers, modestly increasing the IFSS [13]. 22 nm silica particles were incorporated into a sizing package, with other adhesion modifiers, to improve the impact energy absorption of an E-glass composite [14,15]. A novel method of depositing both high and low modulus nanoparticles on to the fiber surfaces from the matrix during cure of the resin was developed by Nguyen and coworkers [16–18]. They observed significant improvements in the energy release rate, G_{IC}, as well as improvements in tensile strength, interlaminar shear strength and other mechanical properties.

Previously, our laboratory has investigated the effects on IFSS, strength, and modulus, in E-glass/poly(vinyl butyral) systems when modifying the interphase with polymeric core-shell particles, where the shell and core consisted of poly(ethyleneimine) (PEI) and poly(styrene), respectively [2]. Two different particle diameters were investigated, 143 nm and 327 nm. The 327 nm particles led to only a modest improvement in properties, while 143 nm particles increased the IFSS and longitudinal tensile modulus and strength by 56%, 42%, and 34%, respectively.

The objective of the present study was to investigate how trimethoxysilane modified poly(ethyleneimine) (SPEI) functionalized silica nanoparticles, electrostatically deposited to E-glass fibers, affected the IFSS of a single fiber composite, as a function of particle size. Well adhered particles would increase the surface roughness of the fibers, increasing the surface area for bonding and provide mechanical interlock between the fiber and matrix. Moreover, mineral oxide nanoparticles have been shown to increase the Young's modulus and fracture toughness in certain thermosets [19–21], improving the shear stress transfer from the matrix to the fiber and limiting the size of debonded regions at the fiber ends, increasing the apparent IFSS. Although

work has been done previously on particle covered fiber composites, there has been no systematic investigation into the effects of particle size, nor has the use of silica/PEI core-shell type interphase modifiers been studied. The particle size determines the toughness and modulus of the interphase, the degree of bonding between the particle and fiber, and the thickness of interphase that is modified. The importance of pH, electrolyte concentration, and particle volume fraction on producing optimum surface coverage was also explored. Although this work focused on E-glass fibers, the methods would be largely applicable to carbon fiber systems as well.

4.2 Micro-mechanical fiber adhesion testing

It is well understood that in continuous fiber reinforced plastics (CFRPs) it is necessary to have good adhesion between the fibers and the matrix. There are a large number of contributing factors that control the adhesion, many of which are can be altered. Clearly, it is necessary to have a means of measuring the adhesion, to determine how processing, materials, and surface modification change the adhesion.

Several methods have been developed; the micro-droplet and the single fiber fragmentation test (SFFT) are the most commonly used, though the fiber pull-out test and the micro-indentation test are historically significant. Here, the general procedure, advantages, and disadvantages will be discussed, with a focus on the SFFT, as it was used extensively in the present work.

4.2.1 Micro-droplet test

In the micro-droplet test a very small droplet of resin is placed on the fiber and cured. The fiber and droplet are then mounted in a test jig which has a “blade micrometer” which

permits the fine adjustment of two sharp edges to a position close to, but not touching, the fiber, schematically shown in Fig. 4.1a. An increasing level of force is then applied to the fiber, pulling the micro-droplet against the blade micrometer, the level of applied force is recorded with a load cell. If the fiber is strong enough, the micro-droplet will debond from the fiber. With knowledge of the fiber diameter, d, applied stress at failure, S_c, fiber length in the droplet, l, and assuming that the shear stress along the length of the fiber is constant, the interface bond strength, τ, can be calculated from Eqn. 4.1, which was derived from a simple force balance [22].

$$\tau = \frac{dS_c}{4l} \tag{4.1}$$

This method is advantageous because it permits the direct, unambiguous measurement of *applied* force necessary to cause interfacial failure. There are a number of considerations, and challenges that hinder consistent, precise measurements. Most significantly is the development of a meniscus, which leads to a wide variation in shear force along the length of the fiber [23]. It can also make the measurement of l ambiguous. The position of the blade micrometer can significantly change the location and magnitude of local shear stress [24]. These effects taken together lead to significant amounts of experimental scatter.

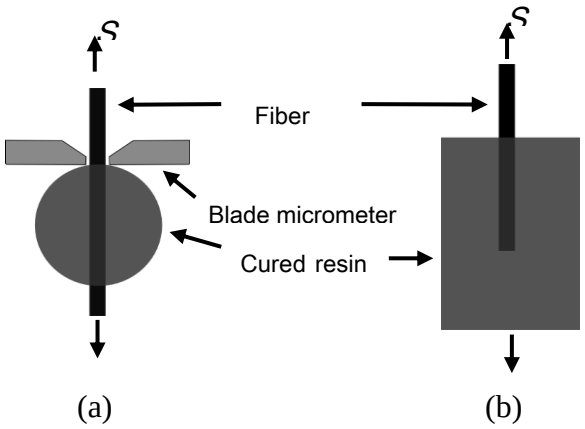

Figure 4.1. An illustration of the a) micro-droplet test and the b) fiber pull-out test

4.2.2 Fiber pull-out test

The fiber pull-out test, shown in Fig. 4.1b, is another direct force measurement for the determination of adhesion [22]. This method was more common when large diameter fibers were the state of the art. Modern small diameter fibers (<~15 μm) are difficult to handle, and can carry only small loads, limiting the depth of fiber that can be embedded into the matrix, *l*, because the fiber would break before the interface. The maximum *l*, for many carbon fiber/epoxy matrix systems is less than 1 mm. The geometry of the in fiber/matrix/air interface generates large stress concentrations, which can cause crack initiation, followed by propagation. As with the micro-droplet test, a meniscus forms by wicking, making determination of *l* difficult, and altering the shear stress distribution [23]. These factors often lead to a lack of precision in the experimental data.

4.2.3 Micro-indentation test

The micro-indentation technique is a way to measure the adhesion in a real composite, which can be advantageous, as processing can affect the adhesion. In this test, a section of unidirectional composite specimen is cut, transverse to the fiber direction and polished. Then, using a micro-hardness indenter a compressive force is applied to the composite surface, until debonding is observed microscopically [25], the procedure is shown in Fig. 4.2. The interface bond strength, τ, can be calculated from Eqn. 4.2, here S_c is the average compressive stress applied to the fiber to cause debonding and τ_{max}/S_{app} is the ratio of the maximum interface shear stress divided by the applied stress, as determined by a finite element model (FEM) for the given system.

$$\tau = S_c \left(\frac{\tau_{max}}{S_{app}}\right)_{FEM} \tag{4.2}$$

Major limitations include the need for a FEM solution for the system, composite slice preparation, and sensitivity to local fiber volume fractions. However, automated, commercially available instruments have been developed.

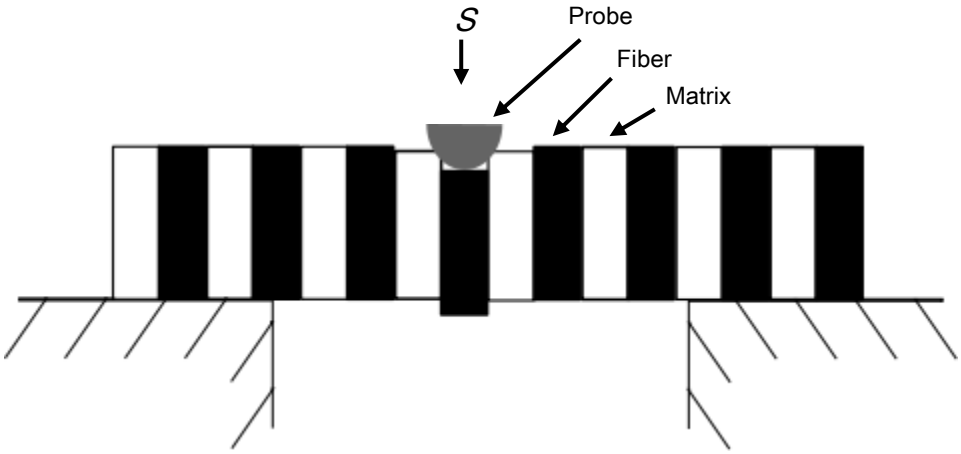

Figure 4.2. An illustration of the micro-indentation test

4.2.4 Single fiber fragmentation test

The most common method for adhesion determination with continuous fibers is the single fiber fragmentation test (SFFT), initially developed by Kelly and Tyson who were investigating brittle tungsten fibers in a ductile copper matrix [26]. In this test, a fiber is embedded in a dog-bone shaped specimen, made of a material with a failure to strain more than three times that of the fiber, to avoid premature specimen failure. When the specimen is subjected to increasing levels of axial tensile stress the fiber breaks where the fiber axial stress, S_f, reaches its tensile strength, $S_{f,c}$. This process continues until all the fiber segments are so short that there is not sufficient area for shear stress transfer to generate a fiber tensile stress great enough to cause the fiber to break. This minimum length is called the *critical transfer length*, l_c. Figure 4.3 illustrates the dog-bone specimen, the fiber breakage with increasing applied stress, and the fiber axial stress profile, assuming constant shear stress along the fiber length. The length of the fiber

segments can then be determined by transmitted light microscopy. Often cross polarized light microscopy is used to determine the stress distribution near the fiber ends.

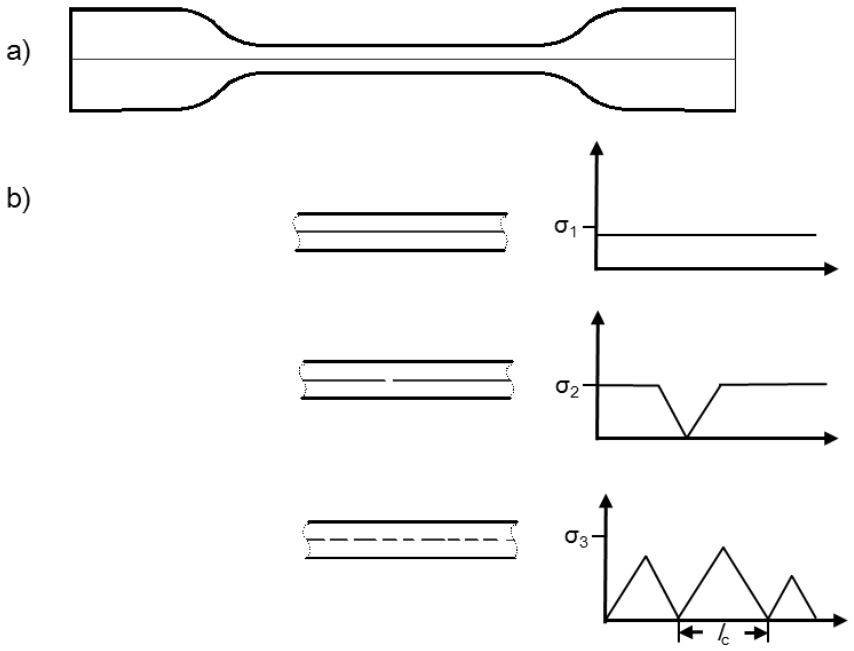

Figure 4.3. A schematic showing a) a dog-bone specimen for SFFTs and b) the fiber fragmentation as the SFFT test progresses (as higher loads are applied) with the corresponding fiber axial stresses, assuming the shear stress is uniform the length of the fiber segment

Kelly and Tyson applied a simple force balance across a differential fiber segment to estimate the average shear strength at the interface, τ, assuming a constant shear stress along the length of the fiber segment:

$$\tau = \frac{S_{f,c} d}{2 l_c} \tag{4.3}$$

where d is the fiber diameter.

In practice, there is a distribution of fiber segments following the SFFT. If a segment length is greater than l_c it will break into two segments, thus in practice the broken segments have lengths between $0.5 l_c$ and l_c. If the probability of fiber segment length is constant from

$0.5l_c$ and l_c, this leads to the relationship $l_c = 4/3l_{ave}$, where l_{ave} is the average length of the fiber segments, typically determined by dividing the gauge length by the number of breaks, plus one [27]. Although this analysis is used in this work, and many others, the assumption that the broken fiber segments vary in size linearly between l_c and $0.5l_c$ is not valid [28,29]. Intrinsic flaws, and flaws introduced during handling, are stress concentrators causing failure well below the theoretical material maximum. Their spatial distribution and severity varies, leading to a distribution in fiber strength. This causes the probability fiber segment length to vary from $0.5l_c$ and l_c. If the Weibull distribution of fiber strength is determined the relationship between l_c and l_{ave} can be more accurately be determined as [30]:

$$l_c = \Gamma\left[1 - \frac{1}{1-k}\right] l_{ave} \tag{4.4}$$

where Γ is the gamma function and k is the Weibull shape parameter, often referred to as the Weibull modulus, of fiber strength.

The fiber strength, $S_{f,c}$, can be determined by applying a tensile strain sufficient to cause the fiber to break, measuring the applied stress at failure. ASTM C1557 recommends that 20 or more fibers are tested, with a uniform gauge length. Then using Weibull statistics, the Weibull mean can be determined, which is discussed in section 2.3.2. Alternatively, the gauge length can be varied, typically to lengths as short as is practical, and $S_{f,c}$ can be determined as a function of gauge length. Extrapolating to zero gives the fiber strength independent of the presence of surface flaws. The distribution of fiber strength and diameter leads to a wide distribution of measured interfacial shear strength, even if the fiber surface strength and chemistry is consistent from fiber to fiber. Because the fiber strength varies as a function of length, the value for $S_{f,c}$ used in Eqn. 4.3 would ideally be measured at l_{ave}.

Additionally, Eqn. 4.3 assumes a constant shear stress along the length of the fiber segment, which is not the case [31]. Cox [32] first derived an elastic load transfer model for fibrous materials, with two major assumptions: first, lateral stiffness and Poisson contraction of the matrix and fiber is the same and second, that the shear stress at the interface is dependent on the relationship between the displacement in the fiber axial direction (in the single fiber composite) and the displacement at the same location, in the absence of a fiber. The Cox one dimensional solution for fiber stress as a function of the fiber axial direction, *s(z)*, and interfacial shear stress, *τ(z)* are:

$$s(z) = E_f \varepsilon_\infty \left(1 - \frac{\cosh \beta(1/2 - z)}{\cosh 1/2 \beta}\right) \tag{4.5}$$

$$\tau(z) = E_f \varepsilon_\infty \frac{\beta R_f}{2} \left(\frac{\sinh \beta(1/2 - z)}{\cosh 1/2 \beta}\right) \tag{4.6}$$

with

$$\beta = \left(\frac{2G_m}{E_f R_f^2 \ln \frac{R_m}{R_f}}\right)^{1/2} \tag{4.7}$$

where E_f is the Young's modulus of the fiber, ε_∞ is applied strain, z is the location in the fiber direction, where $z = 0$ at the fiber end, R_f is the fiber radius, G_m is the matrix shear modulus and R_m is the radius of the region of matrix which is under shear stress. Knowledge of R_m is, of course, essential for the application of the Cox model, but is difficult to accurately determine experimentally for the single fiber composite case [33], but can be taken to be half the distance between fibers in a multiple fiber composite system [29]. An empirical solution for R_m has been developed [29]:

$$R_m = \left(0.782 + \frac{13.36}{L/(2R_f)}\right)\left(\frac{E_f}{E_m}\right) exp\left(0.42 - \frac{9.86R_f}{L}\right) \quad (4.8)$$

where L is the segment length.

Dow [34] refined the Cox model, relaxing the assumptions that the matrix axial displacement is constant, and that there is no bonding at the fiber end. Rosen [35] expanded on Cox's work for the solution of the stress on a fiber embedded in a continuous fiber composite, assuming that a fiber is embedded in a matrix embedded in a homogenous material with mechanical properties equal to that of the composite. Since these early works on the shear-lag model, there have been a number of researchers [36,37] who have expanded, and complicated, the analysis.

Early shear-lag models assumed perfect bonding, but in real specimens there are often debonded regions near the fiber ends caused by interfacial crack propagation, a product of the SFFT, as well as debonded regions present before the SFFT caused by chemical and physical heterogeneity [38,39]. The size of the debonded regions is dependent on the applied strain, shear strength and fracture toughness of the interface [40,41]. These debonded regions transfer shear stress to the fiber by friction and so the coefficient of friction and radial stress become important. The radial stress is a function of cure shrinkage, residual thermal stress and the Poisson effect. When a material is subject to strain in one direction, it typically contracts in the other direction (when considering a radially symmetrical and isotropic body in radial coordinates), the ratio of contraction to applied strain is the Poisson ratio, v:

$$\nu = -\frac{d\varepsilon_r}{d\varepsilon_z} \quad (4.9)$$

where ε_r is the strain in the radial direction, and ε_z is the applied strain in the fiber axial direction. Typically, polymers have higher Poisson ratios than glass or carbon fiber, leading to increasing radial compressive stress with increasing applied tensile strain, causing strain dependent frictional forces at debonded regions, which is taken into account in some micromechanical models [40–42]. This can create an apparent dependence on applied strain for critical fiber lengths.

There are other effects that control the level of fiber axial stress, in addition to the interfacial strength such as interfacial friction, and matrix shear modulus, discussed above. It has been postulated that in some systems the shear strength of the matrix is the limiting factor for shear stress transfer to the fiber [43,44], not the strength of the fiber-matrix interface. That is, the region of matrix near the fiber can yield plastically before the interfacial strength is exceeded. Additionally, the modulus of the interphase, also determines the fiber axial stress [45,46]

In the present work, as well as nearly every other work investigating fiber surface treatments, the analysis of the SFFT was performed with the Kelly-Tyson shear-lag model, Eqn. 4.3, using $l_c = 4/3 l_{ave}$. The limitations of the simple analysis are understood, however, it permits a *comparative* study for different surface treatments, as long as the fiber type, treatment, and strength of the fiber and matrix material are kept constant. Additionally, one of the most significant advantages of the SFFT, when compared to most of the other micromechanical adhesion tests, is the similarity to real composites. Thus, if there is an *apparent* increase in interfacial strength, that is an *actual* increase of stress transfer to the fiber, due to an increase in modulus of the interphase, or an increase in friction at the debonded regions, the effect can be just as significant as an actual increase in interfacial strength.

4.3 Methods

4.3.1 Fiber functionalization

The fiber sizing was removed from E-glass fibers, (Fiberex Inc., Leduc, Alberta, Canada) by soaking in NoChromix (Godax Laboratories, Cabin John, MD) and concentrated sulfuric acid for 90 min. The fibers were rinsed with deionized (DI) H_2O, then dried at 100°C for several hours. The desized fibers had an average diameter of 8.9 μm, as determined by scanning electron microscope (SEM) (JSM 7000, JEOL, Akishima, Japan) image analysis. Individual fibers were removed from the tow and mounted on a handling jig. 0.5 vol% GPS (Gelest Inc, Morrisville, PA) was hydrolyzed in 190 proof ethanol for 20 min with sufficient acetic acid to reduce the pH to 4.5. The fibers were functionalized in the GPS solution for 60 min then dried at room temperature. For comparison, one set of fibers was functionalized with trimethoxysilane modified poly(ethyleneimine) (SPEI) (Gelest Inc), molecular weight 1,500 – 1,800. The functionalization procedure was identical to functionalization with GPS.

4.3.2 Nanoparticle functionalization

Four different silica nanoparticles were used, 16 nm Ludox SM-30, 26 nm Ludox TMA (Sigma Aldrich, St. Louis, MO), 71 nm Nexsil 85A (Nyacol, Ashland, MO), and 100 nm (Fiber Optic Center, New Bedford, MA). The referenced particle sizes for the three smallest silica particles were determined by dynamic light scattering (90Plus, Brookhaven Instruments Corp, Holtzville, NY), the diameter of the 100 nm particles was provided by the manufacturer. 1 wt% silica nanoparticles were dispersed in DI H_2O with vigorous stirring followed by 5 min of ultrasonication with a Sonifier 250 with a cup-horn attachment (Branson Ultrasonics Corp., Danbury, CT). The amount of SPEI used to functionalize each batch was 0.5 vol% or calculated from the approximate number of moles of hydroxyl functional groups on the surface, whichever

was larger. The manufacturer reported values for surface area for SM-30, TMA, Nexsil 85A, and 100 nm silica were 400, 140, 55, and 6 m^2/g, respectively. Assuming a hydroxyl surface coverage of 5 OH nm^{-2} [4], the approximate molar concentration of surface hydroxyl groups can be determined. Assuming that one SPEI molecule reacts with one hydroxyl surface group, the amount of SPEI needed for each particle type was 5.80, 2.03, 0.8, and 0.5 vol%, for 16, 26, 71, and 100 nm particles, respectively. The SPEI was added drop-wise with vigorous mixing, and the pH was reduced to 4.5 with acetic acid. Flocculation occurred with the addition of SPEI which was dispersed by sonicating for 15 min (Model 8848, Cole-Parmer, Vernon Hills, IL). The suspensions were mixed for an additional 45 min.

After functionalization, the suspensions were purified. The 16 and 26 nm particles were dialyzed with regenerated cellulose dialysis tubing (Fisher Scientific, Waltham, MA), with a nominal pore size of 4.8 nm which retains materials with a M.W. of 12,000 g/mol or higher. The suspension was dialyzed in DI H_2O until the conductivity remained constant with time, typically four days. The purified suspensions were diluted to 0.1 vol% in DI H_2O. The larger particles, 71 and 100 nm, were centrifuged at 7,500 RPM for 15 min or 5,500 for 10 min, respectively. The supernatant was removed, an equivalent amount of DI H_2O was added, the particles were redispersed and centrifuged again to "rinse" the particles. Finally, the particles were redispersed in DI H_2O and diluted to achieve 0.1 vol% solids.

The relative amounts of SPEI and silica were determined by thermogravimetric analysis (TGA). The colloidal suspensions were dried at room temperature, about 20 mg of the solids were placed in an alumina crucible and heated to 900°C at 20°C/min in a TGA instrument (Q50, TA Instruments, New Castle, DE) with a nitrogen purge.

4.3.3 Nanoparticle deposition on fibers

The pH of the suspensions was adjusted to 7.0 using KOH and HNO_3. KNO_3 was added at concentrations of 0.5, 0.75, 0.015, and 0.05 M for the 16, 26, 71, and 100 nm silica suspensions, respectively. The 0.1 vol% SPEI functionalized silica suspensions were heated to 85°C, and the GPS functionalized fibers were submerged for 60 s. The fibers were then rinsed with DI H_2O to remove residual salt. The optimum conditions for surface coverage (KNO_3 concentration, pH, particle volume fraction, and submersion duration) were determined by systematically varying each variable independently, then making qualitative observations from SEM images.

4.3.4 Particle-fiber adhesion determination: wipe test and fracture surface analysis

To qualitatively determine the adhesion between the nanoparticles and the fiber surfaces a wipe test was performed. Following particle deposition, the fiber was placed between two, 1 x 3 inch pieces of Whatman 41 filter paper (Whatman International Ltd, Springfield Mill, UK), backed by glass microscope slides and weighted to generate 690 Pa of pressure. The fiber was then pulled through the filter paper at about 1 cm/s. The fibers were then imaged with SEM to determine the extent of particle removal.

Additionally, a single tow composite made with nanoparticles on the fibers was mode I fractured and the surface was imaged with SEM to determine if the particles remained adhered to the fibers or if they were removed with the matrix. Single tows were surface treated in a similar manner to the single fiber specimens. The treated tows were placed in a mold with a 1.0 x 1.0 mm grove. The composite was made with a wet layup method using a stoichiometric ratio of diglycidyl ether of bisphenol A (EP-828, Miller-Stephenson, Danbury, CT) and m-phenylenediamine (mPDA) (Sigma-Aldrich, St. Louis, MO). The mold was vacuum bagged

using a woven peel ply and cotton breather fabric, and about 27 in Hg vacuum was applied for the first 2 hours of cure. The composite was cured at 75°C for 2 hours and post cured at 125°C for an additional 2 hours. A crack was started in the specimen with a razor blade, and propagated by pulling the two halves apart. The fracture surfaces were sputter coated with a gold-palladium mixture for 70 s and imaged with SEM.

4.3.5 Single fiber strength determination

The strength of the E-glass fibers, as-received (sized), bare (desized), and GPS functionalized was determined in accordance with ASTM C1557 using a tensile test machine (T1000, Satec, Grove City, PA). The fibers were mounted in paper-board tabs to facilitate handling. The gauge length was 5 cm and the displacement rate was 1 mm/min. 20 specimens of each fiber type were tested.

4.3.6 Single fiber fragmentation test

Individual fibers were suspended across a dog-bone style silicone mold, with dimensions illustrated in Fig. 4.4. A stoichiometric ratio of diglycidyl ether of bisphenol A (EP-828, Miller-Stephenson, Danbury, CT) and m-phenylenediamine (mPDA) (Sigma-Aldrich, St. Louis, MO) were mixed for 10 min at 800 RPM with a magnetic stir bar at 75°C. 0.8 ml was pipetted into the mold cavities and cured at 75°C for 2 hours and post cured at 125°C for an additional 2 hours in a convection oven (model 825F, Fisher Scientific, Hampton, NH).

The dog-bone samples were placed a miniature tensile test frame (St. John's Computer Machine, St. John's, MI), shown mounted to a transmitted light microscope (IX70, Olympus, Tokyo, Japan) in Fig. 4.5. Tensile strain was applied at 0.003 mm/ mm min. Generally, fiber fragmentation started at a strain of 8% and reached the critical length, l_c, at 10% strain. The

samples were strained to 12%. At least six samples were tested for each system; 10 samples were typical. After straining, a 25mm slide cover was placed on the sample to act as a consistent measure of the gauge length, and the fiber breaks were counted using a transmitted light bright field microscope.

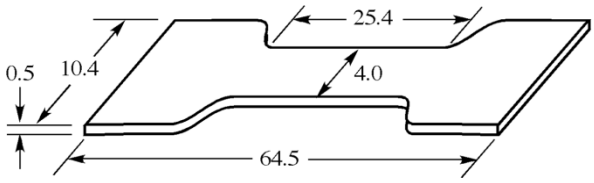

Figure 4.4. A schematic of a dog-bone sample; the dimensions are in mm

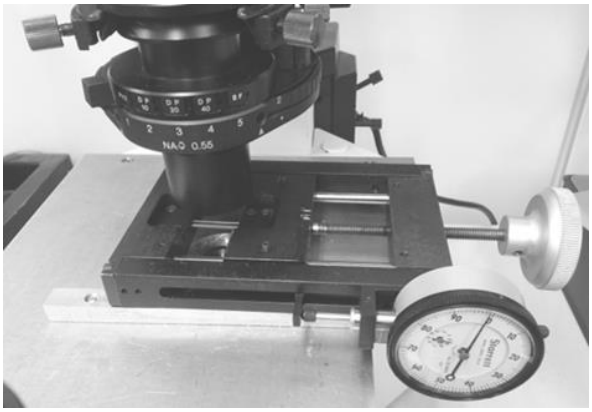

Figure 4.5. The miniature tensile test frame, mounted to a transmitted light microscope

4.4 Results and discussion

4.4.1 Fiber strength

In order to estimate the IFSS using the SFFT method, it was necessary to know the strength of the fibers. The strength of the ceramic fibers was largely controlled by the presence of surface flaws. By modifying the fiber surfaces these flaws could become more severe, or mitigated, changing the strength of the fibers [47]. Thus, the fiber strength was measured for the as-received, desized and GPS functionalized fibers. The stresses to failure were plotted on a

cumulative Weibull plot, and linear lines were fit to the data for the three fiber types investigated, shown in Fig. 4.6. From the linearized cumulative Weibull distribution, Eqn. 4.10, the Weibull shape, *k*, and scale, λ, parameters were determined with knowledge of the cumulative probability of failure, *F(x)*, and the stress at failure, *x*.

$$\ln(-\ln(1 - F(x)) = k\ ln(x) - k\ \ln(\lambda) \tag{4.10}$$

The Weibull means of fiber critical strength, $S_{f,c}$, were calculated with Eqn. 4.11, where Γ is the gamma function. The values for the shape and scale factors and mean strength are given in Table 4.1. More details on Weibull statistics are giving in section 2.3.2.

$$S_{f,c} = \lambda\Gamma(1 + {}^{1}/_{k}) \tag{4.11}$$

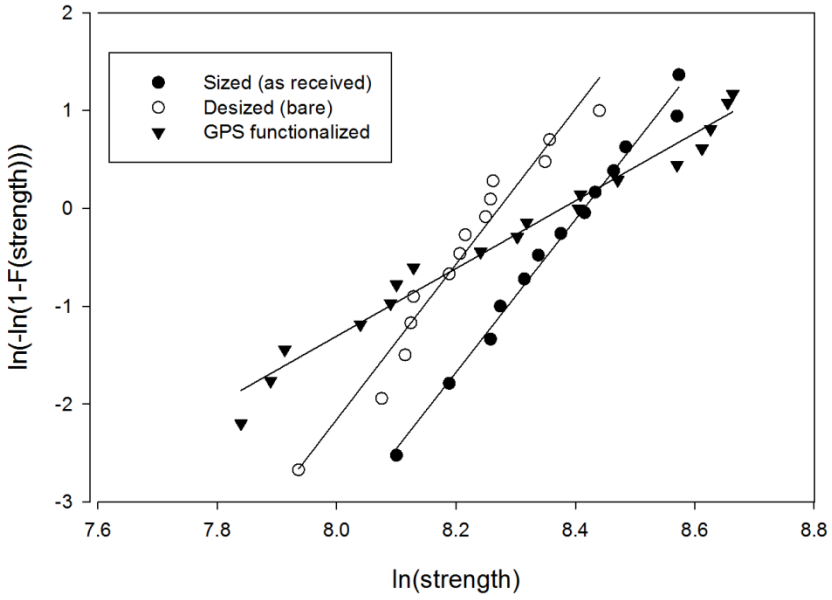

Figure 4.6. The Weibull plot of the strengths of E-glass fibers, as received (black circles), desized with NoChromix and H_2SO_4 (open circles), and desized then functionalized with GPS (triangles)

Table 4.1. The Weibull scale factor, shape factor and mean of sized, desized, and GPS functionalized E-glass fibers

	Scale Factor [MPa]	Shape Factor	Mean [MPa]
Sized	4512	7.8	4244
Bare	3911	7.6	3681
GPS	4349	3.3	3900

When the sizing was removed from the fiber surface it became vulnerable to physical damaged from handing, leading to a reduction in strength. When the desized fibers were treated with GPS it would crosslink on, and with, the fiber surface mitigating the surface flaws, leading to an increase in average fiber strength, when compared to the desized fibers [48,49]. However, the GPS functionalized fibers had a large variation in fiber strength, indicating that GPS strengthens fibers inconsistently.

4.4.2 Surface coverage as a function of pH and salt concentration

By controlling the electrostatics of the particles and fibers, it was possible to control the extent of particle coverage on the fibers. The amine groups of the SPEI were basic, causing the functionalized particles to take on a positive surface charge, and the hydroxyl groups on the E-glass fibers were acidic causing them to have a negative surface charge in water, over a large pH range. This is illustrated in Fig. 4.7, where the mobilities of ground E-glass fibers and PEI functionalized particles are plotted as a function of pH. Thus, when the fibers were submerged in a suspension of SPEI functionalized particles, they spontaneously adhered to the fiber surface. To determine the optimum pH, GPS functionalized fibers were dipped in 0.1 vol% 100 nm SPEI functionalized silica suspensions with a pH varied between 4.4 and 9.2. It was found, with SEM imaging, that a pH of 7 gave the best surface coverage. Representative micrographs of some pHs tested are shown in Fig. 4.8.

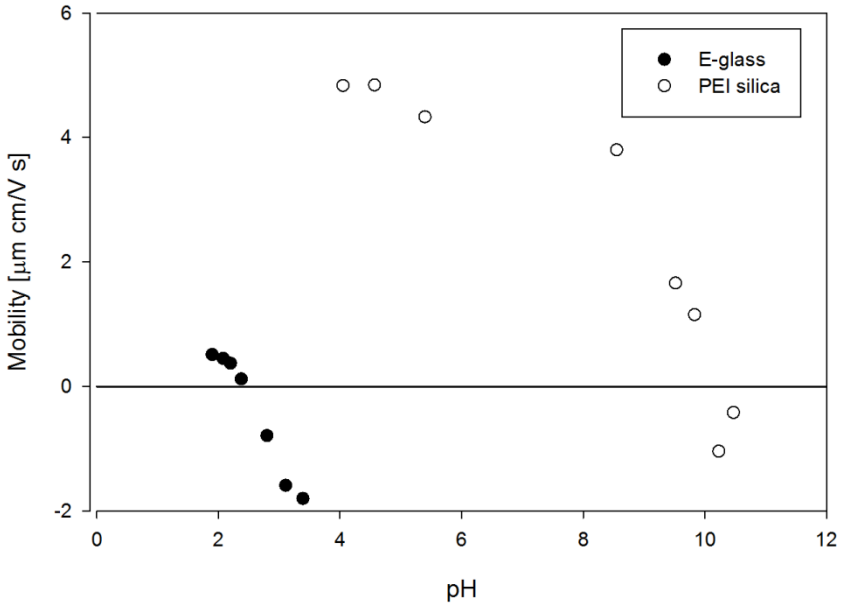

Figure 4.7. The electrophoretic mobilities of ground E-glass fibers and PEI functionalized 100 nm silica particles as a function of pH

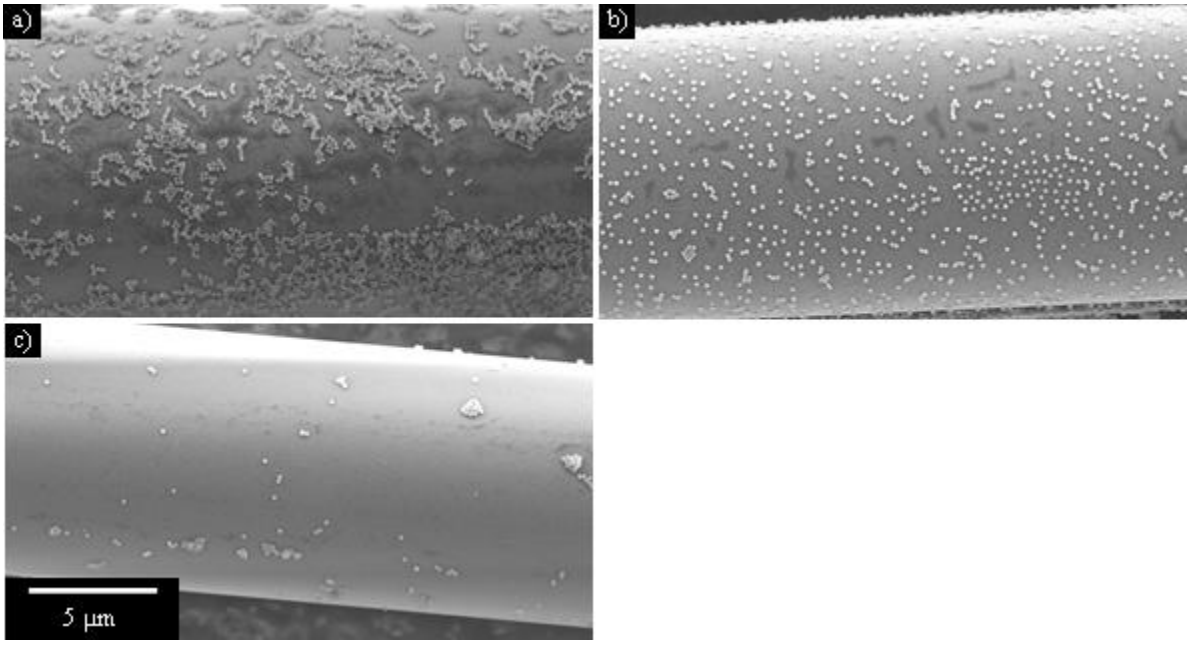

Figure 4.8. SPEI functionalized 100 nm silica particles on a GPS functionalized fiber with a pH of a) 9.2, b) 7.0, and c) 4.4

A monolayer of particles would give the maximum surface area without particle-particle bonding, and is assumed to be the ideal case. However, it can be seen from Fig. 4.8b that adjusting the pH is not sufficient to obtain a monolayer because electrostatic repulsion between the particles prevents the approach of close neighbors. The range of electrical potential is related to the Debye length, κ^{-1}, or the "screening length;" it is the distance from the particle surface over which the electrical potential has fallen to 1/e (0.368) of its surface potential. It can be calculated by [50]:

$$\kappa^{-1} = \sqrt{\frac{\varepsilon\varepsilon_0 kT}{2e^2z^2n_\infty}} \tag{4.12}$$

where ε is dielectric constant of the medium, ε_0 is permittivity of free space, k is the Boltzmann constant, T is the temperature, e is the protonic charge, z is the valence of the background electrolyte, and n_∞ is the number density of the electrolyte. Thus, by adding an electrolyte, such as KNO_3, the range of electrostatic repulsion can be reduced, leading to a denser layer of particles on the surface. KNO_3 was chosen as an electrolyte because neither ion specifically adsorbs to the fiber or particle surfaces.

The optimum KNO_3 concentration was determined for each particle size by systematically varying the concentration, coating GPS functionalized fibers, and making observations using SEM. An example of the surface coverage dependence on electrolyte concentration is shown in Fig. 4.9, where the KNO_3 concentration is varied from 0 – 0.75 M for the colloidal suspension of 26 nm functionalized particles. Example micrographs of the particle coating, for each particle size, using the optimum KNO_3 concentration, are shown in Fig. 4.10. For the two smallest particle sizes, the volume of electrical double layer was sufficient to cause depletion of bulk electrolyte concentration, necessitating large amounts of KNO_3.

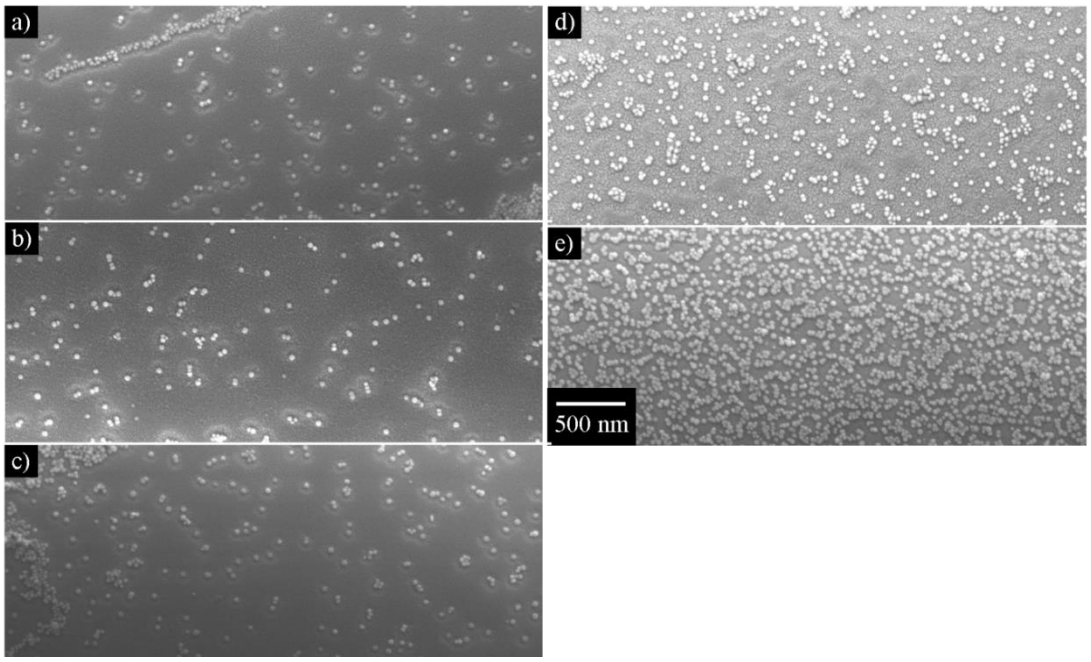

Figure 4.9. The change in surface coverage of SPEI functionalized 26 nm silica particles on GPS functionalized fibers with a KNO_3 concentration of a) 0, b) 0.01, c) 0.05, d) 0.25, and e) 0.75 M

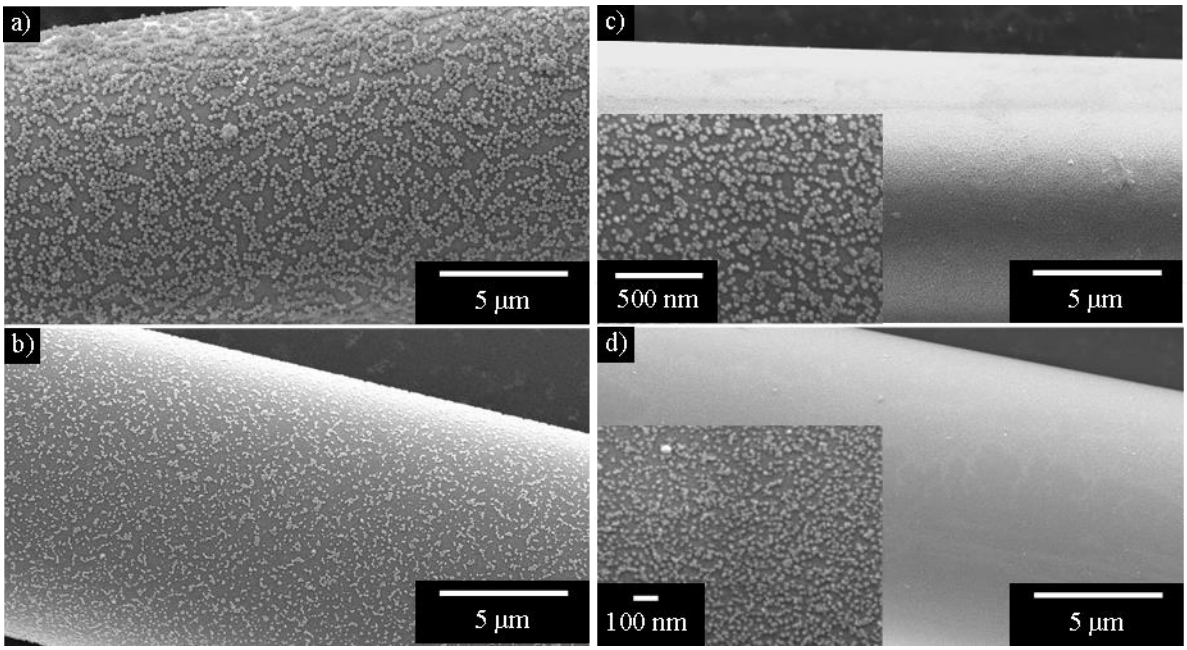

Figure 4.10. SEM micrographs of GPS glass fibers with a) 100 nm, b) 71 nm, c) 26, and d) 16 nm SPEI particles deposited on the surface, using optimum KNO_3 concentrations

4.4.3 Particle adhesion: wipe test and fracture surface

Preparing samples for the SFFT, as well as performing the test, required significant amounts of time. In an effort to improve throughput in screening potential particle size, types, and surface chemistries it was necessary to develop a means of rapid characterization of the adhesion between particles and the fiber surface. The wipe test, where a particle coated fiber was pulled through weighted glass slides covered in filter paper, followed by SEM imagining, was a way to qualitatively determine the adhesion. Additionally, the IFSS is dependent on a multitude of factors, including matrix modulus [44,51], the variation in interphase modulus as a function of distance from the fiber surface [52], fracture toughness [53] of the interface, and the formation of cracks at the fiber breaks. The wipe test was a way to simply measure the particle-fiber adhesion. Differences in particle size would change the amount of force exerted on each particle. An example the images generated for a wipe test are shown in Fig. 4.11. With SPEI functionalized particles on GPS functionalized fibers, as the particle size is decreased the number of particles removed decreases. This is expected because the ratio of particle-fiber contact to particle height increases, and the relative amount of SPEI to silica also increases, making the small particles more difficult to remove. Functionalized 16, 26, 71 and 100 nm silica particles contained 57, 28, 1.9 and 0.3 wt% polymer, respectively, as determined by TGA. Because SPEI is essential for adhesion between the particles and fibers, larger amounts would improve the adhesion.

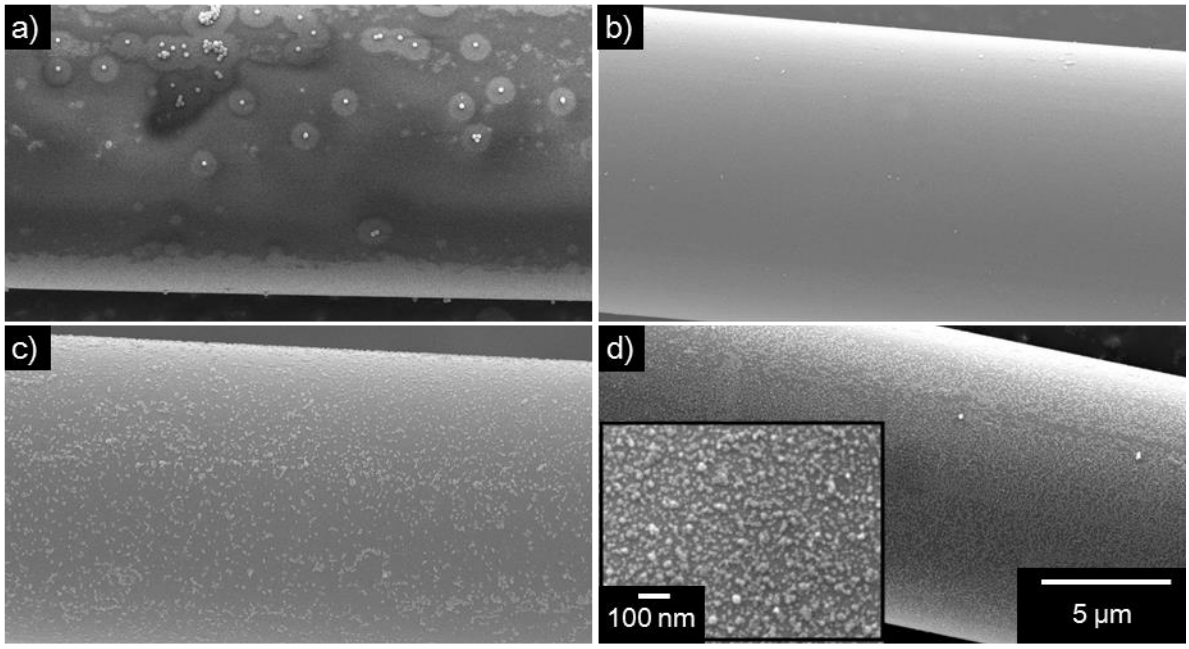

Figure 4.11. SEM micrographs of GPS glass fibers with a) 100 nm, b) 71 nm, c) 26, and d) 16 nm SPEI particles following the wipe test

In another qualitative adhesion test, single tow composites with nanoparticles deposited on the fiber surfaces were *mode I* fractured, with the crack propagating in the fiber direction. 100 nm particles were relatively poorly adhered and the crack propagated at the fiber-particle interface, particles can be seen embedded in the matrix (lower third of the image) but not on the fiber surface (upper two thirds of the image) in Fig. 4.12a. The 71 nm particles were better adhered and exhibited a mixed failure interface, shown in Fig. 12b, where the fiber surface (bottom two thirds of the image) is *partially* covered in particles, the remainder were pulled off with the matrix. 26 nm particle systems exhibited crack propagation at the particle-matrix interface (right hand side of the image) or cohesive failure of the matrix (left hand side of the image), Fig. 12c. 16 nm particle systems generated mainly smooth fracture surfaces, owing to the low surface roughness generated by the very small size, shown in Fig. 12d.

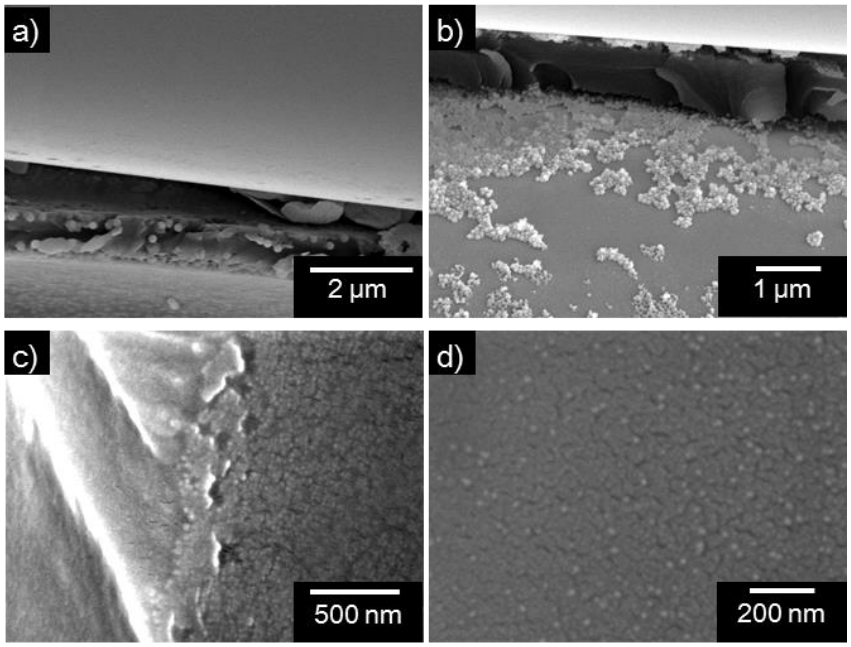

Figure 4.12. SEM micrographs of the fiber surfaces from a single tow composite, fractured in *mode I*

4.4.4 Interfacial Shear Strength

There are a number of potential mechanisms by which particles deposited on to the surface of the fibers would affect the IFSS. They may alter the inter*phase*; in the system studied here the modulus would be increased and, depending on the particle size, the fracture toughness may be increased by increasing the surface area generated by a growing crack, increasing the energy necessary to cause propagation. They would also alter the inter*face* if they are sufficiently well adhered, increasing the surface for bonding area and improving adhesion by mechanical interlock. There was no attempt to quantitatively determine the individual contributions of these different mechanisms to the IFSS.

The ability of the interphase to transfer stress from the polymer matrix to the glass fiber was determined by single fiber fragmentation tests [23,54]. When tensile strain is applied to the dog-bone specimen load is transferred to the fiber by shear stress at the fiber surface. With

increasing strain the fiber axial tensile stress is increased until the strength of the fiber is exceeded, causing the fiber to break. Additional strain is applied and the process continues until the area of the fiber fragment is too small to transfer sufficient stress to cause further fiber breaks. This minimum fiber length, l_c, can be used to estimate the IFSS, τ, with Eqn. 4.3. As discussed in section 4.2.4, the $S_{f,c}$ is a relatively wide distribution of values, as is the fiber diameter, leading to a distribution of measured IFSS values. IFSS for as received, bare (desized), GPS functionalized, SPEI functionalized, and GPS functionalized with 16, 26, 71, and 100 nm SPEI functionalized particles are shown in Fig. 4.13.

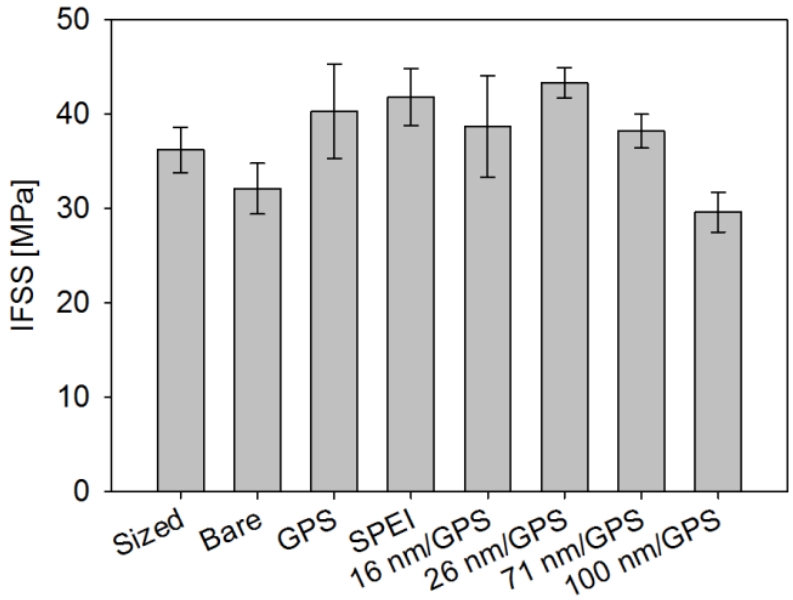

Figure 4.13. The IFSS for sized (as received), desized (bare), GPS functionalized, SPEI functionalized and GPS functionalized with 16, 26, 71, and 100 nm SPEI functionalized particles

The IFSS of the bare fibers was 11% lower than the as received, sized fibers because the sizing contains adhesion promoters. Treating the bare fibers with GPS increased the IFSS by 25% as it forms a partially cross-linked interphase, covalently bound to both the fiber and the

matrix. Treating the fiber with SPEI increased the IFSS 30%, a similar amount to treating with GPS. This is fortuitous as it allows conclusions to be made about altering the fiber surface topography and interphase with functionalized particles; that is, changes in IFSS in systems with functionalized nanoparticles were not simply a product of changing the surface chemistry.

The 26 nm SPEI functionalized silica particles on GPS functionalized fibers increased the IFSS 35% over bare fibers, and 8% over GPS fibers, with no particles. This improvement was attributed to an increase in the fracture toughness and modulus of the interphase and mechanical interlock between the particle layer and the matrix. The increase in fracture toughness is from the increase in energy necessary to propagate an interface crack because there is increase in surface area of the fracture surface. Typically, when a fiber breaks during the SFFT a large shear stress concentration is developed at the end, causing debonding. By increasing the fracture toughness and reducing fiber debonding a larger portion of the fiber remains bound to the matrix, allowing increased shear stress transfer as the SFFT proceeds. If segments of the fiber are debonded, shear stress is transferred only by friction, reducing the shear stress transfer as the number of breaks, and thus the debonded area, increases.

When the average particle size is reduced to 16 nm the IFSS is decreased by 4%. These particles are well adhered, as illustrated in section 4.4.3, but were too small to significantly increase the level of mechanical interlock or otherwise affect the interface or interphase. Moreover, the depositing nanoparticles invariably introduced some aggregates, leading to a slight reduction in strength.

The 71 and 100 nm particles decreased the IFSS 4% and 27%, respectively, when compared to GPS functionalized fibers. The 100 nm particles were poorly adhered, as demonstrated by the wipe test, and therefore were not effective at transferring load to the fiber.

The particles also acted as flaws at the fiber-matrix interface, decreasing the interfacial strength and toughness. The 71 nm particles were an intermediate case between the 100 nm and 26 nm particles. Many of the particles were well adhered, but many were removed during the wipe test.

Clearly there is an optimum particle size for increasing the IFSS. If the particles are too large, the applied shear forces easily exceed the adhesive strength of the particles to the fibers. If the particles are too small, the interfacial roughness and mechanical interlock would not be significantly increased, and so the IFSS would not be improved. It follows that if the particles could be better adhered to the fiber, larger particles could be used, increasing mechanical interlock and surface roughness, improving the IFSS further. Attempts were made at improving the particle-fiber adhesion using high temperature annealing, ceramic sol gel thin films and other techniques but none were successful. These experiments are detailed in Appendix B.

The SPEI functionalized 26 nm particles were also deposited on sized and bare fibers, increasing the IFSS 16% in both cases. The IFSS of these systems, with the corresponding fiber type without particles, are shown in Fig. 4.14. This suggests that appropriately sized functionalized silica nanoparticles can be used as a robust method to improve adhesion, even if applied after the sizing.

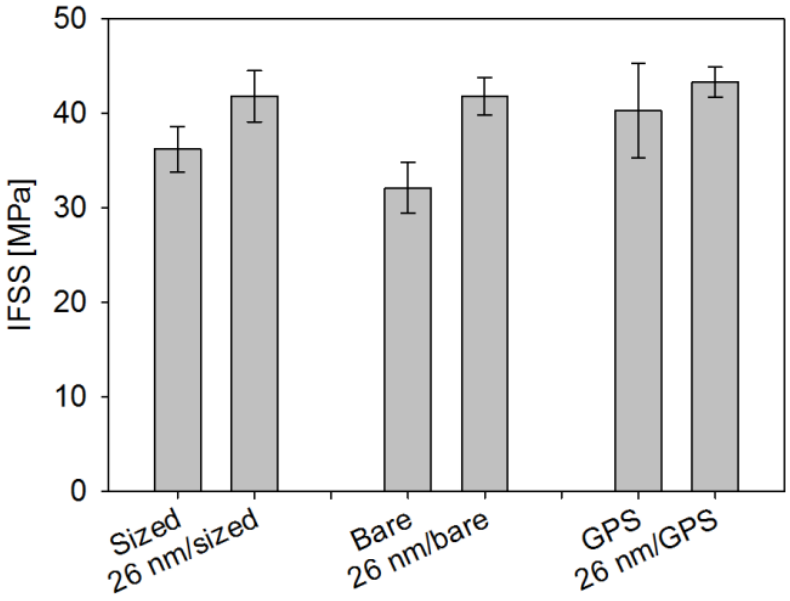

Figure 4.14. IFSS values of sized, bare and GPS functionalized E-glass fibers with and without SPEI functionalized 26 nm silica particles

4.4.5 Bright field optical microscopy

It is possible to make qualitative conclusions about the adhesive strength of the fiber-matrix bond by taking bright field micrographs of the fiber ends, following the SFFT. In systems with fibers having a higher Young's modulus than the matrix, a large shear stress concentration develops at the fiber-matrix interface with applied tensile load, leading to debonding unless the fibers are well adhered. This can be observed using bright field optical microscopy to examine the fibers after the SFFT. Representative transmitted light bright field micrographs are shown in Fig 4.15.

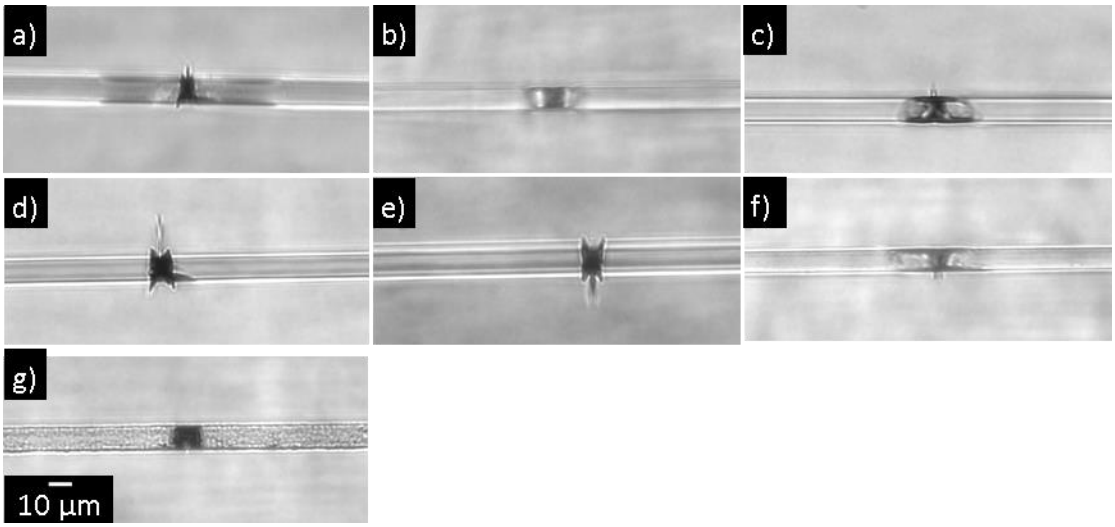

Figure 4.15. Optical micrographs of the fiber ends following the SFFT with varying surface treatments a) sized, b) bare, c) GPS functionalized, d) 16 nm particles, e) 26 nm particles, f) 71 nm particles and g) 100 nm particles

Debonding exists at the fiber ends for sized, bare and even GPS functionalized fibers. However, the addition of 16 and 26 nm SPEI functionalized particles prevents debonding. Increasing the particle size to 71 and 100 nm increases the amount of debonding. Although it is not clear from Fig. 4.15g, the 100 nm system has large regions of debonding that are not associated with fiber ends; the interface, in some regions, failed before the fiber during the SFFT. These debonded regions were observed using cross polarized light microscopy, example micrographs are not shown here.

4.5 Conclusions

Using appropriately sized trimethoxysilane modified poly(ethyleneimine) functionalized silica nanoparticles can be an effective means to improve the interfacial shear strength (IFSS) between E-glass fibers and a matrix of m-phenylenediamine and the BADGE epoxy EP-828. 26 nm particles on a GPS functionalized fiber the IFSS was increased 35% over bare fibers, and 8% over GPS functionalized fibers. The IFSS is highly dependent on the size of nanoparticles used.

16 nm particles had little effect on the IFSS, while increasing the size to 71 and 100 nm leads to decreasing IFSS values. The improvement in IFSS was likely caused by shear stress transfer by mechanical interlock, an increase in the fiber surface area, and increasing the interphase toughness and modulus.

Obtaining uniform, dense coverage of the SPEI functionalized particles on the fiber surfaces was achieved by carefully controlling the electrostatics. The pH was adjusted to 7, to achieve a strong negative surface charge on the fibers and a strong positive surface charge on the functionalized particles. Varying amounts of KNO_3 were added to reduce the range of electrostatic repulsion between the particles, increasing the surface coverage on the fibers, leading to monolayer coverage.

References

[1] Madhukar M, Drzal L. Fiber-Matrix Adhesion and Its Effect on Composite Mechanical-Properties .2. Longitudinal (0-Degrees) and Transverse (90-Degrees) Tensile and Flexure Behavior of Graphite Epoxy Composites. J Compos Mater 1991;25:958–91.

[2] Leonard GC, Hosseinpour D, Berg JC. Modulus-Graded Interphase Modifiers in E-Glass Fiber/Thermoplastic Composites. J Adhes Sci Technol 2009;23:2031–46.

[3] Drzal LT. The role of the fiber-matrix interphase on composite properties. Vacuum 1990;41:1615–8.

[4] Plueddemann EP. Silane Coupling Agents. Springer; 1982.

[5] Thostenson ET, Li WZ, Wang DZ, Ren ZF, Chou TW. Carbon nanotube/carbon fiber hybrid multiscale composites. J Appl Phys 2002;91:6034–7.

[6] Zhao ZG, Ci LJ, Cheng HM, Bai JB. The growth of multi-walled carbon nanotubes with different morphologies on carbon fibers. Carbon 2005;43:663–5.

[7] Garcia EJ, Wardle BL, Hart AJ, Yamamoto N. Fabrication and multifunctional properties of a hybrid laminate with aligned carbon nanotubes grown In Situ. Compos Sci Technol 2008;68:2034–41.

[8] Ehlert GJ, Sodano HA. Zinc Oxide Nanowire Interphase for Enhanced Interfacial Strength in Lightweight Polymer Fiber Composites. Acs Appl Mater Interfaces 2009;1:1827–33.

[9] Galan U, Lin Y, Ehlert GJ, Sodano HA. Effect of ZnO nanowire morphology on the interfacial strength of nanowire coated carbon fibers. Compos Sci Technol 2011;71:946–54.

[10] Lin Y, Ehlert G, Sodano HA. Increased Interface Strength in Carbon Fiber Composites through a ZnO Nanowire Interphase. Adv Funct Mater 2009;19:2654–60.

[11] Gao X, Jensen RE, Li W, Deitzel J, McKnight SH, Gillespie JW. Effect of fiber surface texture created from silane blends on the strength and energy absorption of the glass fiber/epoxy interphase. J Compos Mater 2008;42:513–34.
[12] Bekyarova E, Thostenson ET, Yu A, Kim H, Gao J, Tang J, et al. Multiscale carbon nanotube-carbon fiber reinforcement for advanced epoxy composites. Langmuir 2007;23:3970–4.
[13] Kamae T, Drzal LT. Carbon fiber/epoxy composite property enhancement through incorporation of carbon nanotubes at the fiber–matrix interphase – Part I: The development of carbon nanotube coated carbon fibers and the evaluation of their adhesion. Compos Part Appl Sci Manuf 2012;43:1569–77.
[14] Jensen R, Mcknight S. Inorganic–organic fiber sizings for enhanced energy absorption in glass fiber-reinforced composites intended for structural applications. Compos Sci Technol 2006;66:509–21.
[15] Gao X, Jensen RE, McKnight SH, Gillespie JW. Effect of colloidal silica on the strength and energy absorption of glass fiber/epoxy interphases. Compos Part -Appl Sci Manuf 2011;42:1738–47.
[16] Nguyen FN, Haro A, Yoshioka K. Maximizing Fiber-to-composite strength translation with a nanomaterial reinforced interphase, 2012.
[17] Nguyen FN, Haro A, kenichi Y. Effects of a nanomaterial toughened interphase in carbon fiber reinforced polymer composite, Wichita, KS: 2013.
[18] Nguyen FN, Haro A, Tun S, Yoshioka K. Hard nanomaterial toughened carbon fiber reinforced polymer composite, Wichita, KS: Society for the Advancement of Material and Process Engineering; 2013.
[19] Hsieh TH, Kinloch AJ, Masania K, Sohn Lee J, Taylor AC, Sprenger S. The toughness of epoxy polymers and fibre composites modified with rubber microparticles and silica nanoparticles. J Mater Sci 2009;45:1193–210.
[20] Fu S-Y, Feng X-Q, Lauke B, Mai Y-W. Effects of particle size, particle/matrix interface adhesion and particle loading on mechanical properties of particulate–polymer composites. Compos Part B Eng 2008;39:933–61.
[21] Cho J, Joshi MS, Sun CT. Effect of inclusion size on mechanical properties of polymeric composites with micro and nano particles. Compos Sci Technol 2006;66:1941–52.
[22] Broutman LJ. Measurement of the Fiber-Polymer Matrix Interfacial Strength. In: Committee D-30, editor. Interfaces Compos., West Conshohocken, PA: ASTM International; n.d., p. 27–27–15.
[23] Herrerafranco P, Drzal L. Comparison of Methods for the Measurement of Fiber Matrix Adhesion in Composites. Composites 1992;23:2–27.
[24] Wu H, Claypool C. An Analytical Approach of the Microbond Test Method Used in Characterizing the Fiber Matrix Interface. J Mater Sci Lett 1991;10:260–2.
[25] Mandell J, Chen J, McGarry F. A Microdebonding Test for In-Situ Fiber-Matrix Bond Strength and Moisture Effects, New Orleans, LA: Society of the Plastics Industry; 1980, p. 26–d.
[26] Kelly A, Tyson W. Tensile Properties of Fibre-Reinforced Metals - Copper/Tungsten and Copper/Molybdenum. J Mech Phys Solids 1965;13:329–&.
[27] Ohsawa T, Nakayama A, Miwa M, Hasegawa A. Temperature-Dependence of Critical Fiber Length for Glass Fiber-Reinforced Thermosetting Resins. J Appl Polym Sci 1978;22:3203–12.

[28] Feillard P, Desarmot G, Favre J. Theoretical Aspects of the Fragmentation Test. Compos Sci Technol 1994;50:265–79.
[29] Yilmaz YI. Analyzing single fiber fragmentation test data by using stress transfer model. J Compos Mater 2002;36:537–51.
[30] Drzal LT, Rich MJ, Camping JD, Park WJ. Interfacial shear strength and failure mechanisms in graphite fiber composites, 1980, p. 20C.
[31] Guild F, Vlattas C, Galiotis C. Modeling of Stress Transfer in Fiber Composites. Compos Sci Technol 1994;50:319–32.
[32] Cox H. The Elasticity and Strength of Paper and Other Fibrous Materials. Br J Appl Phys 1952;3:72–9.
[33] Galiotis C. Interfacial Studies on Model Composites by Laser Raman-Spectroscopy. Compos Sci Technol 1991;42:125–50.
[34] Dow NF. Study of stresses near a discontinuity in a filament-reinforced composite metal. DTIC Document; 1963.
[35] Rosen BW. Mechanics of composite strengthening. 1965:37–75.
[36] Nairn J. A Variational Mechanics Analysis of the Stresses Around Breaks in Embedded Fibers. Mech Mater 1992;13:131–54.
[37] Drzal LT, Whitney JM. Toughened Composites: Symposium on Toughened Composites. ASTM International; 1987.
[38] Lacroix T, Tilmans B, Keunings R, Desaeger M, Verpoest I. Modeling of Critical Fiber Length and Interfacial Debonding in the Fragmentation Testing of Polymer Composites. Compos Sci Technol 1992;43:379–87.
[39] Favre J, Sigety P, Jacques D. Stress Transfer by Shear in Carbon-Fiber Model Composites .2. Computer-Simulation of the Fragmentation Test. J Mater Sci 1991;26:189–95.
[40] Zhou L, Mai Y, Baillie C. Interfacial Debonding and Fiber Pull-Out Stresses .5. a Methodology for Evaluation of Interfacial Properties. J Mater Sci 1994;29:5541–50.
[41] Zhou L, Kim J, Baillie C, Mai Y. Fracture-Mechanics Analysis of the Fiber Fragmentation Test. J Compos Mater 1995;29:881–902.
[42] Copponnex TJ. Analysis and evaluation of the single-fibre fragmentation test. Compos Sci Technol 1996;56:893–909.
[43] Bascom W, Jensen R. Stress Transfer in Single Fiber Resin Tensile Tests. J Adhes 1986;19:219–39.
[44] Drzal LT. The effect of polymeric matrix mechanical properties on the fiber-matrix interfacial shear strength. Mater Sci Eng A 1990;126:289–93.
[45] Ho H, Drzal LT. Non-linear numerical study of the single-fiber fragmentation test. Part I: Test mechanics. Compos Eng 1995;5:1231–44.
[46] Ho H, Drzal LT. Non-linear numerical study of the single-fiber fragmentation test. Part II: A parametric study. Compos Eng 1995;5:1245–59.
[47] Zinck P, Mader E, Gerard JF. Role of silane coupling agent and polymeric film former for tailoring glass fiber sizings from tensile strength measurements. J Mater Sci 2001;36:5245–52.
[48] Iglesias JG, González-Benito J, Aznar AJ, Bravo J, Baselga J. Effect of Glass Fiber Surface Treatments on Mechanical Strength of Epoxy Based Composite Materials. J Colloid Interface Sci 2002;250:251–60.
[49] Hamada H, Ikuta N, Nishida N, Maekawa Z. Effect of interfacial silane network structure on interfacial strength in glass fibre composites. Composites 1994;25:512–5.

[50] Berg JC. An introduction to interfaces & colloids: the bridge to nanoscience. Singapore; Hackensack, NJ: World Scientific; 2010.
[51] Rao V, Drzal L. The Dependence of Interfacial Shear-Strength on Matrix and Interphase Properties. Polym Compos 1991;12:48–56.
[52] Williams JG, Donnellan ME, James MR, Morris WL. Properties of the interphase in organic matrix composites. Mater Sci Eng A 1990;126:305–12.
[53] Kim J-K, Mai YW. Engineered interfaces in fiber reinforced composites. Amsterdam; New York: Elsevier Sciences; 1998.
[54] Feih S, Wonsyld K, Minzari D, Westermann P, Lilholt H. Testing procedure for the single fiber fragmentation test 2004.

Chapter 5 – Conclusions and recommendations

Engineering the next generation of composite materials is an important and difficult task. There are still large gaps in our fundamental understanding of the materials and there are persistent needs to improve material properties, control the stress transfer between the phases, and reduce weight and cost, among other goals. Recognizing the breadth of challenges in the composites industry, this work addressed three major challenges: improving the understanding of stress concentration in particulate composites, progress to making lightweight thermosetting resin systems, and improving the adhesion between continuous fibers and a thermosetting matrix with a topography modifier. Major discoveries and recommendations for further study are summarized below.

5.1 Debonding in particulate composites

5.1.1 Conclusions

650 μm glass spheres were used to make a particulate composite with poly(vinyl butyral) (PVB). The volume percent of spheres was changed from 1 to 15 vol% to decrease the inter-particle separation to probe the effects of overlapping stress fields. A simple computer model of these systems was developed.

1) Increasing the particle volume fraction decreases the average inter-particle spacing leading to an increase in overlap of the stress concentrations formed around the spheres. This increase in stress concentration, led to high local stresses which cause debonding at relatively low *applied* stress. However, given the random nature of the dispersion, a wide distribution of local stresses were developed.

2) An adhesion promoter, 3-aminopropyltriethoxysilane (APS) was applied to some systems, leading to a higher applied stress necessary to cause debonding, proportional to the increase in adhesive strength. APS did not increase the adhesion strength of all spheres equally, leading to a wider distribution of stress necessary to cause debonding.

3) A semi-predictive model for the level of debonding for a given experimentally determined adhesive strength, particle volume fraction, and applied stress was developed based on Goodier's

analytical solution for the stress concentration developed around a single inclusion and the superposition principle.

5.1.2 Future work

One could imagine methods to better measure the complex stress fields developed in a particulate composite, by using methods other than counting the number of debonding events, perhaps by using cross polarized light microscopy. The most obvious means of continuing this work would be the refinement of the model, though, one of the model's most appealing attributes as presented is its simplicity.

1) The model could be improved by considering the finite dimensions of the rectangular specimen, that is, the stress concentration present in a rectangular specimen without particulates could be calculated and summed with the stress concentration from neighboring particulates.

2) More importantly, the method of a generating a virtual composite, the random placement of spheres, could be modified to generate a distribution more representative of a real composite system.

5.2 Nano-voids in thermosets

Using the methods outlined in Chapter 3, there are three steps that must be accomplished to generate a nano-void lightened thermoset: first, a *blowing agent well* must be made presumably with a self-assembling block-copolymer, next, a blowing agent must partition into the interior of the blowing agent well, finally, to generate a "void" the blowing agent would undergo a phase change becoming a gas, thermally decompose into gaseous compounds, or, if the matrix were a solid, the "blowing agent" could simply diffuse out. The first two steps have been successful, laying the ground work for the generation of these lightweight materials.

5.2.1 Conclusions

A number of amphiphiles with one portion of the molecule being epoxy soluble poly(ethylene oxide) (PEO) were studied as potential blowing agent wells. Some materials appear to be successful candidates.

1) Fortegra 102 (likely poly(ethylene oxide)-block-poly(propylene oxide) or poly(butylene oxide) block-copolymer) and poly(ethylene)-block-poly(ethylene oxide) (PE-PEO) could be used

to create micelle blowing agent wells to solubilize alkanes. These solubilized alkanes could be used as blowing agents.

2) The fluorinated, non-ionic surfactant, FSN-100, forms micelles at a temperature above 40°C and at a concentration greater than 1.0 wt% prior to curing. After curing there were typically ~0.5 μm spherical domains, the result of a phase separation caused by the reduced solubility as the cure progressed .Increasing the temperature above 60°C decreased the intensity of SAXS scattering, suggesting the dissolution of micelles.

5.2.2 Future work

Two of the three steps for generating a lightweight thermoset have been performed. However, the last step of taking alkane swollen micelles and generating gas filled bubbles still must be developed. There are a number of possible avenues.

1) If sufficient supersaturation in the interior of the micelle were generated, that is, a high enough temperature with a low enough pressure, the alkane would undergo a phase change, generating a gas, possibly giving the material desired. This method presents challenges because the degree of cure would be dependent on the thermal history, and the degree of cure and temperature dictate the viscosity and modulus, which, in turn, would control the interior pressure of the micelles. These two coupled parameters would make controlling nucleation and bubble growth difficult. Additionally, using lower molecular weight alkanes, such as methane or ethane would increase the super saturation at a given temperature, but would increase the solubility in the thermoset.

2) In an alternative method, it may be possible to incorporate *chemical* blowing agents into the blowing agent wells, such as octanioc hydrazide, shown in Fig. 5.1. Chemical blowing agents typically generate low molecular weight gases via thermal degradation. Thus, if a high enough concentration of gas molecules were produced, it may be possible to generate gas filled bubbles at relatively low temperatures.

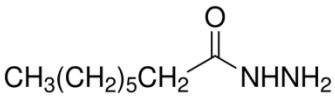

Figure 5.1. The chemical formula of octanoic hydrazide

3) A template method may also be feasible, the alkane may diffuse out of the swollen micelles with elevated temperature and reduced pressure, and if the matrix were solid, gas filled bubbles would remain. This method would require diffusion through a solid substrate, which would be very slow, or, if the matrix were a highly cross-linked resin, impossible. This method would be feasible with solid precursors, partially cured resins, or lightly cross-linked resins.

5.3 Improving fiber-matrix adhesion with functionalized silica nanoparticles

The adhesions between E-glass fibers and an epoxy matrix can be improved using a very narrow size range of poly(ethylene imine) (PEI) functionalized silica nano-particles. A number of other surface topography modification methods were used, without an increase in adhesion, and are outlined in Appendix B.

5.3.1 Conclusions

1) Depositing a near monolayer of 26 nm PEI functionalized silica nano-particles on glycidyloxypropyltrimethoxysilane (GPS) increased the interfacial shear stress (IFSS) 35% when compared to the bare fiber. There was a 16% increase in IFSS when these particles were deposited on bare and sized fibers, when compared to the analogous system without particles.

2) Using 16, 71, and 100 nm PEI functionalized silica nanoparticles did not increase the IFSS.

3) By carefully controlling the pH to maximize the electrostatic attraction between the particles and fibers, while using KNO_3 to reduce the range of electrostatic repulsion between particles, the surface coverage can be optimized.

5.3.2 Future work

1) The motivation for increasing the adhesion is to increase composite mechanical properties. Therefore, it is necessary to make and test high fiber volume fraction composite specimens, with the particle coated fibers to ascertain their influence on bulk properties, particularly tensile and flexural strength and modulus, but also interlaminar shear strength.

2) There are a number of possible mechanisms that contribute to the improved shear stress transfer between the fiber and the matrix, including mechanical interlock and an increase in interfacial fracture toughness. It is difficult to completely deconvelute these mechanisms, but some additional experimentation may provide some further insight. For example, similarly sized

core-shell rubber particles could be deposited on the surface, where the shell would remain PEI, but the core would be a soft polymer, such as poly(styrene). These particles would increase the interfacial toughness, at the expense of the interphase modulus. Also, colloidal tip atomic force microscopy experiments with analogous systems could provide qualitative measurements of the adhesion of the particles to the fibers.

Bibliography

Agarwal, Bhagwan D., Lawrence J. Broutman, and K. Chandrashekhara. 2006. *Analysis and Performance of Fiber Composites*. 3rd ed. Wiley.

Anderson, T. L. 2005. *Fracture Mechanics: Fundamentals and Applications*. Boca Raton, FL: Taylor & Francis.

Asp, L. E., B. A. Sjogren, and L. A. Berglund. 1997. "Prediction of Failure Initiation in Polypropylene with Glass Beads." *Polymer Composites* 18 (1) (February): 9–15. doi:10.1002/pc.10256.

Bardy, Erik, Joseph Mollendorf, and David Pendergast. 2006. "Thermal Resistance and Compressive Strain of Underwater Aerogel–syntactic Foam Hybrid Insulation at Atmospheric and Elevated Hydrostatic Pressure." *Journal of Physics D: Applied Physics* 39 (9): 1908.

Bascom, Wd, and Rm Jensen. 1986. "Stress Transfer in Single Fiber Resin Tensile Tests." *Journal of Adhesion* 19 (3-4): 219–239. doi:10.1080/00218468608071225.

Beck, Rh, S. Gratch, S. Newman, and Kc Rusch. 1968. "Yield Behavior of Polyblends." *Journal of Polymer Science Part B-Polymer Letters* 6 (10PB): 707–&. doi:10.1002/pol.1968.110061005.

Becker, R., and W. Doring. 1935. "Kinetic treatment of germ formation in supersaturated vapour." *Annalen Der Physik* 24 (8) (December): 719–752.

Bekyarova, E., E. T Thostenson, A. Yu, H. Kim, J. Gao, J. Tang, H. T Hahn, T. -W Chou, M. E Itkis, and R. C Haddon. 2007. "Multiscale Carbon Nanotube-Carbon Fiber Reinforcement for Advanced Epoxy Composites." *Langmuir* 23 (7) (March 27): 3970–3974. doi:10.1021/la062743p.

Berg, John C. 2010. *An Introduction to Interfaces & Colloids: The Bridge to Nanoscience*. Singapore; Hackensack, NJ: World Scientific.

Bogush, Gh, Ma Tracy, and Cf Zukoski. 1988. "Preparation of Monodisperse Silica Particles - Control of Size and Mass Fraction." *Journal of Non-Crystalline Solids* 104 (1) (August): 95–106. doi:10.1016/0022-3093(88)90187-1.

Bradley, R. H., X. Ling, and I. Sutherland. 1993. "An Investigation of Carbon Fibre Surface Chemistry and Reactivity Based on XPS and Surface Free Energy." *Carbon* 31 (7): 1115–1120.

Broutman, L J. 2013. "Measurement of the Fiber-Polymer Matrix Interfacial Strength." In *Interfaces in Composites*, edited by Committee D-30, 27–27–15. West Conshohocken, PA: ASTM International. Accessed December 11.

Cardoso, R. J., A. Shukla, and A. Bose. 2002. "Effect of Particle Size and Surface Treatment on Constitutive Properties of Polyester-Cenosphere Composites." *Journal of Materials Science* 37 (3): 603–613.

Carlisle, K. B., M. Koopman, K. K. Chawla, R. Kulkarni, G. M. Gladysz, and M. Lewis. 2006. "Microstructure and Compressive Properties of Carbon Microballoons." *Journal of Materials Science* 41 (13): 3987–3997.

Caruso, F., R. A. Caruso, and H. Mohwald. 1998. "Nanoengineering of Inorganic and Hybrid Hollow Spheres by Colloidal Templating." *Science* 282 (5391) (November 6): 1111–1114. doi:10.1126/science.282.5391.1111.

Caruso, Rachel A., Andrei Susha, and Frank Caruso. 2001. “Multilayered Titania, Silica, and Laponite Nanoparticle Coatings on Polystyrene Colloidal Templates and Resulting Inorganic Hollow Spheres.” *Chemistry of Materials* 13 (2): 400–409.

Chan, C. M., G. Z. Cao, H. Fong, M. Sarikaya, T. Robinson, and L. Nelson. 2000. “Nanoindentation and Adhesion of Sol-Gel-Derived Hard Coatings on Polyester.” *Journal of Materials Research* 15 (1) (January): 148–154. doi:10.1557/JMR.2000.0025.

Chand, S. 2000. “Review Carbon Fibers for Composites.” *Journal of Materials Science* 35 (6): 1303–1313.

Chen, Jian-Feng, Hao-Min Ding, Jie-Xin Wang, and Lei Shao. 2004. “Preparation and Characterization of Porous Hollow Silica Nanoparticles for Drug Delivery Application.” *Biomaterials* 25 (4): 723–727.

Cho, J., M.S. Joshi, and C.T. Sun. 2006. “Effect of Inclusion Size on Mechanical Properties of Polymeric Composites with Micro and Nano Particles.” *Composites Science and Technology* 66 (13) (October): 1941–1952. doi:10.1016/j.compscitech.2005.12.028.

Colton, J. S., and N. P. Suh. 1987. “The Nucleation of Microcellular Thermoplastic Foam with Additives: Part I: Theoretical Considerations.” *Polymer Engineering & Science* 27 (7): 485–492. doi:10.1002/pen.760270702.

Copponnex, T. J. 1996. “Analysis and Evaluation of the Single-Fibre Fragmentation Test.” *Composites Science and Technology* 56 (8): 893–909. doi:10.1016/0266-3538(96)00049-8.

Cosgrove, T. 2005. *Colloid Science Principles, Methods and Applications*. Oxford, UK; Ames, Iowa: Blackwell Pub.

Cox, Hl. 1952. “The Elasticity and Strength of Paper and Other Fibrous Materials.” *British Journal of Applied Physics* 3 (MAR): 72–79. doi:10.1088/0508-3443/3/3/302.

Dean, J. M., R. B. Grubbs, W. Saad, R. F. Cook, and F. S. Bates. 2003. “Mechanical Properties of Block Copolymer Vesicle and Micelle Modified Epoxies.” *Journal of Polymer Science Part B: Polymer Physics* 41 (20): 2444–2456.

Dean, J. M., P. M. Lipic, R. B. Grubbs, R. F. Cook, and F. S. Bates. 2001. “Micellar Structure and Mechanical Properties of Block Copolymer-Modified Epoxies.” *Journal of Polymer Science Part B: Polymer Physics* 39 (23): 2996–3010.

Dow, Norris F. 1963. “Study of Stresses near a Discontinuity in a Filament-Reinforced Composite Metal”.

Drzal, L T, M J Rich, J D Camping, and W J Park. 1980. “Interfacial Shear Strength and Failure Mechanisms in Graphite Fiber Composites.” In , 20C.

Drzal, L T, and J M Whitney. 1987. *Toughened Composites: Symposium on Toughened Composites*. ASTM International.

Drzal, L. T. 1990. “The Role of the Fiber-Matrix Interphase on Composite Properties.” *Vacuum* 41 (7): 1615–1618.

Drzal, Lawrence T. 1990. “The Effect of Polymeric Matrix Mechanical Properties on the Fiber-Matrix Interfacial Shear Strength.” *Materials Science and Engineering: A* 126 (1): 289–293.

Ehlert, Gregory J, and Henry A Sodano. 2009. “Zinc Oxide Nanowire Interphase for Enhanced Interfacial Strength in Lightweight Polymer Fiber Composites.” *Acs Applied Materials & Interfaces* 1 (8) (August): 1827–1833. doi:10.1021/am900376t.

Ema, Yu, Manabu Ikeya, and Masami Okamoto. 2006. “Foam Processing and Cellular Structure of Polylactide-Based Nanocomposites.” *Polymer* 47 (15): 5350–5359.

Favre, Jp, P. Sigety, and D. Jacques. 1991. “Stress Transfer by Shear in Carbon-Fiber Model Composites .2. Computer-Simulation of the Fragmentation Test.” *Journal of Materials Science* 26 (1) (January 1): 189–195. doi:10.1007/BF00576050.

Feih, S, K Wonsyld, D Minzari, P Westermann, and H Lilholt. 2004. “Testing Procedure for the Single Fiber Fragmentation Test”. Pitney Bowes.

Feih, S., E. Boiocchi, G. Mathys, Z. Mathys, A. G Gibson, and A. P Mouritz. 2011. “Mechanical Properties of Thermally-Treated and Recycled Glass Fibres.” *Composites Part B-Engineering* 42 (3) (April): 350–358. doi:10.1016/j.compositesb.2010.12.020.

Feillard, P., G. Desarmot, and Jp Favre. 1994. “Theoretical Aspects of the Fragmentation Test.” *Composites Science and Technology* 50 (2): 265–279. doi:10.1016/0266-3538(94)90148-1.

Fowkes, Frederick M. 1987. “Role of Acid-Base Interfacial Bonding in Adhesion.” *Journal of Adhesion Science and Technology* 1 (1): 7–27. doi:10.1163/156856187X00049.

Frisch, Kurt Charles, and J. H Saunders. 1972. *Plastic Foams.* New York: M. Dekker.

Fu, Jin, and Hani E. Naguib. 2006. “Effect of Nanoclay on the Mechanical Properties of PMMA/clay Nanocomposite Foams.” *Journal of Cellular Plastics* 42 (4): 325–342.

Fu, Shao-Yun, Xi-Qiao Feng, Bernd Lauke, and Yiu-Wing Mai. 2008. “Effects of Particle Size, Particle/matrix Interface Adhesion and Particle Loading on Mechanical Properties of Particulate–polymer Composites.” *Composites Part B: Engineering* 39 (6) (September): 933–961. doi:10.1016/j.compositesb.2008.01.002.

Galan, Ulises, Yirong Lin, Gregory J Ehlert, and Henry A Sodano. 2011. “Effect of ZnO Nanowire Morphology on the Interfacial Strength of Nanowire Coated Carbon Fibers.” *Composites Science and Technology* 71 (7) (May 4): 946–954. doi:10.1016/j.compscitech.2011.02.010.

Galiotis, C. 1991. “Interfacial Studies on Model Composites by Laser Raman-Spectroscopy.” *Composites Science and Technology* 42 (1-3): 125–150. doi:10.1016/0266-3538(91)90015-H.

Gao, X., R. E Jensen, S. H McKnight, and J. W. Gillespie. 2011. “Effect of Colloidal Silica on the Strength and Energy Absorption of Glass Fiber/epoxy Interphases.” *Composites Part a-Applied Science and Manufacturing* 42 (11) (November): 1738–1747. doi:10.1016/j.compositesa.2011.07.029.

Gao, X., R. E. Jensen, W. Li, J. Deitzel, S. H. McKnight, and J. W. Gillespie. 2008. “Effect of Fiber Surface Texture Created from Silane Blends on the Strength and Energy Absorption of the Glass Fiber/epoxy Interphase.” *Journal of Composite Materials* 42 (5) (March): 513–534. doi:10.1177/0021998307086203.

Garcia, Enrique J., Brian L. Wardle, A. John Hart, and Namiko Yamamoto. 2008. “Fabrication and Multifunctional Properties of a Hybrid Laminate with Aligned Carbon Nanotubes Grown In Situ.” *Composites Science and Technology* 68 (9) (July): 2034–2041. doi:10.1016/j.compscitech.2008.02.028.

Gent, A. N. 1980. “Detachment of an Elastic Matrix from a Rigid Spherical Inclusion.” *Journal of Materials Science* 15 (11): 2884–2888.

Gent, An, and B. Park. 1984. “Failure Processes in Elastomers at or Near a Rigid Spherical Inclusion.” *Journal of Materials Science* 19 (6): 1947–1956. doi:10.1007/BF00550265.

Goodier, J. 1933. “Concentration of Stress around Spherical and Cylindrical Inclusions and Flaws.” *Journal of Applied Mechanics* 55: 39–44.

Griffith, A. A. 1921. “The Phenomena of Rupture and Flow in Solids.” *Philosophical Transactions of the Royal Society of London. Series A, Containing Papers of a Mathematical or Physical Character* 221 (582-593) (January 1): 163–198. doi:10.1098/rsta.1921.0006.

Grubbs, Robert B., Margaret E. Broz, Jennifer M. Dean, and Frank S. Bates. 2000. “Selectively Epoxidized Polyisoprene−Polybutadiene Block Copolymers.” *Macromolecules* 33 (7) (April): 2308–2310. doi:10.1021/ma992049z.

Grubbs, Robert B., Jennifer M. Dean, Margaret E. Broz, and Frank S. Bates. 2000. “Reactive Block Copolymers for Modification of Thermosetting Epoxy.” *Macromolecules* 33 (26) (December): 9522–9534. doi:10.1021/ma001414f.

Guild, Fj, C. Vlattas, and C. Galiotis. 1994. “Modeling of Stress Transfer in Fiber Composites.” *Composites Science and Technology* 50 (3): 319–332. doi:10.1016/0266-3538(94)90020-5.

Guo, Q. P., R. Thomann, W. Gronski, R. Staneva, R. Ivanova, and B. Stuhn. 2003. “Nanostructures, Semicrytalline Morphology, and Nanoscale Confinement Effect on the Crystallization Kinetics in Self-Organized Block Copolymer/thermoset Blends.” *Macromolecules* 36 (10) (May 20): 3635–3645. doi:10.1021/ma0340154.

Gupta, N., and E. Woldesenbet. 2004. “Microballoon Wall Thickness Effects on Properties of Syntactic Foams.” *Journal of Cellular Plastics* 40 (6) (November): 461–480. doi:10.1177/0021955X04048421.

Gupta, Nikhil, and Eyassu Woldesenbet. 2005. “Characterization of Flexural Properties of Syntactic Foam Core Sandwich Composites and Effect of Density Variation.” *Journal of Composite Materials* 39 (24): 2197–2212.

Ham, Frank S. 1959. “Diffusion-Limited Growth of Precipitate Particles.” *Journal of Applied Physics* 30 (10): 1518–1525. doi:10.1063/1.1734993.

Hamada, H., N. Ikuta, N. Nishida, and Z. Maekawa. 1994. “Effect of Interfacial Silane Network Structure on Interfacial Strength in Glass Fibre Composites.” *Composites* 25 (7): 512–515.

Harding, P. H., and J. C. Berg. 1998. “The Adhesion Promotion Mechanism of Organofunctional Silanes.” *Journal of Applied Polymer Science* 67 (6) (February 7): 1025–1033.

Harding, P. H., S. A. Page, J. a. E. Manson, and J. C. Berg. 1998. “Measurement of Residual Stress Effects by Means of Single-Particle Composite Tests.” *Journal of Adhesion Science and Technology* 12 (5): 497–506. doi:10.1163/156856198X00182.

Herrerafranco, Pj, and Lt Drzal. 1992. “Comparison of Methods for the Measurement of Fiber Matrix Adhesion in Composites.” *Composites* 23 (1) (January): 2–27. doi:10.1016/0010-4361(92)90282-Y.

Hillmyer, M. A., and F. S. Bates. 1996. “Synthesis and Characterization of Model Polyalkane-Poly (ethylene Oxide) Block Copolymers.” *Macromolecules* 29 (22): 6994–7002.

Hillmyer, M. A., P. M. Lipic, D. A. Hajduk, K. Almdal, and F. S. Bates. 1997. “Self-Assembly and Polymerization of Epoxy Resin Amphiphilic Block Copolymer Nanocomposites.” *Journal of the American Chemical Society* 119 (11) (March 19): 2749–2750. doi:10.1021/ja963622m.

Ho, H., and L. T. Drzal. 1995a. “Non-Linear Numerical Study of the Single-Fiber Fragmentation Test. Part I: Test Mechanics.” *Composites Engineering* 5 (10): 1231–1244.

Ho, H., and L. T. Drzal. 1995b. “Non-Linear Numerical Study of the Single-Fiber Fragmentation Test. Part II: A Parametric Study.” *Composites Engineering* 5 (10): 1245–1259.

Hoecker, F., and J. Karger-Kocsis. 1996. “Surface Energetics of Carbon Fibers and Its Effects on the Mechanical Performance of CF/EP Composites.” *Journal of Applied Polymer Science* 59 (1): 139–153.

Hsieh, T. H., A. J. Kinloch, K. Masania, J. Sohn Lee, A. C. Taylor, and S. Sprenger. 2009. “The Toughness of Epoxy Polymers and Fibre Composites Modified with Rubber Microparticles and Silica Nanoparticles.” *Journal of Materials Science* 45 (5) (December 10): 1193–1210. doi:10.1007/s10853-009-4064-9.

Huang, J. S., and L. J. Gibson. 1993. “Elastic Moduli of a Composite of Hollow Spheres in a Matrix.” *Journal of the Mechanics and Physics of Solids* 41 (1): 55–75.

Huang, Y., and A. J. Kinloch. 1992. “The Toughness of Epoxy Polymers Containing Microvoids.” *Polymer* 33 (6): 1330–1332.

Hutchinson, John W. 1987. “Crack Tip Shielding by Micro-Cracking in Brittle Solids.” *Acta Metallurgica* 35 (7): 1605–1619.

Iglesias, J.G., J. González-Benito, A.J. Aznar, J. Bravo, and J. Baselga. 2002. “Effect of Glass Fiber Surface Treatments on Mechanical Strength of Epoxy Based Composite Materials.” *Journal of Colloid and Interface Science* 250 (1) (June): 251–260. doi:10.1006/jcis.2002.8332.

International Conference on Composite Interfaces, Ishida, Hatsuo, and Jack L Koenig, ed. 1986. *Composite Interfaces: Proceedings of the First International Conference on Composite Interfaces (ICCI-I) Held May 27-30, 1986, in Cleveland, Ohio, U.S.A.* New York: North-Holland.

Jensen, R, and S Mcknight. 2006. “Inorganic–organic Fiber Sizings for Enhanced Energy Absorption in Glass Fiber-Reinforced Composites Intended for Structural Applications.” *Composites Science and Technology* 66 (3-4) (March): 509–521. doi:10.1016/j.compscitech.2005.06.004.

Jhaver, Rahul, and Hareesh Tippur. 2009. “Processing, Compression Response and Finite Element Modeling of Syntactic Foam Based Interpenetrating Phase Composite (IPC).” *Materials Science and Engineering: A* 499 (1): 507–517.

Kamae, Toshiya, and Lawrence T. Drzal. 2012. “Carbon Fiber/epoxy Composite Property Enhancement through Incorporation of Carbon Nanotubes at the Fiber–matrix Interphase – Part I: The Development of Carbon Nanotube Coated Carbon Fibers and the Evaluation of Their Adhesion.” *Composites Part A: Applied Science and Manufacturing* 43 (9) (September): 1569–1577. doi:10.1016/j.compositesa.2012.02.016.

Kawaguchi, Takafumi, and Raymond A. Pearson. 2003. “The Effect of Particle–matrix Adhesion on the Mechanical Behavior of Glass Filled Epoxies: Part 1. A Study on Yield Behavior and Cohesive Strength.” *Polymer* 44 (15): 4229–4238.

Kelly, A., and Wr Tyson. 1965. “Tensile Properties of Fibre-Reinforced Metals - Copper/Tungsten and Copper/Molybdenum.” *Journal of the Mechanics and Physics of Solids* 13 (6): 329–&. doi:10.1016/0022-5096(65)90035-9.

Kim, Jang-Kyo, and Y. W Mai. 1998. *Engineered Interfaces in Fiber Reinforced Composites*. Amsterdam; New York: Elsevier Sciences.

Kishore, R. Shankar, and S. Sankaran. 2005. “Short-Beam Three-Point Bend Tests in Syntactic Foams. Part II: Effect of Microballoons Content on Shear Strength.” *Journal of Applied Polymer Science* 98 (2) (October 15): 680–686. doi:10.1002/app.22097.

Kishore, Ravi Shankar, and S. Sankaran. 2006. “Effects of Microballoons’ Size and Content in Epoxy on Compressive Strength and Modulus.” *Journal of Materials Science* 41 (22) (November): 7459–7465. doi:10.1007/s10853-006-0801-5.

Koopman, M., K. K. Chawla, K. B. Carlisle, and G. M. Gladysz. 2006. “Microstructural Failure Modes in Three-Phase Glass Syntactic Foams.” *Journal of Materials Science* 41 (13): 4009–4014.

Kraus, R., W. Wilke, A. Zhuk, I. Luzinov, S. Minko, and A. Voronov. 1997. “Investigation of Debonding Processes in Particle-Filled Polymer Materials by Acoustic Emission: Part I Acoustic Emission and Debonding Stress.” *Journal of Materials Science* 32 (16): 4397–4403.

Lacroix, T., B. Tilmans, R. Keunings, M. Desaeger, and I. Verpoest. 1992. “Modeling of Critical Fiber Length and Interfacial Debonding in the Fragmentation Testing of Polymer Composites.” *Composites Science and Technology* 43 (4): 379–387. doi:10.1016/0266-3538(92)90061-7.

Larranaga, Maider, Inaki Mondragon, and Carmen Cristina Riccardi. 2007. “Miscibility and Mechanical Properties of an Amine-Cured Epoxy Resin Blended with Poly(ethylene Oxide).” *Polymer International* 56 (3) (March): 426–433. doi:10.1002/pi.2184.

Lee, J., and A. F. Yee. 2000. “Fracture of Glass Bead/epoxy Composites: On Micro-Mechanical Deformations.” *Polymer* 41 (23): 8363–8373.

Lee, J., and A. F. Yee. 2001. “Inorganic Particle Toughening I: Micro-Mechanical Deformations in the Fracture of Glass Bead Filled Epoxies.” *Polymer* 42 (2): 577–588.

Leonard, Geoffrey C, Dariush Hosseinpour, and John C Berg. 2009. “Modulus-Graded Interphase Modifiers in E-Glass Fiber/Thermoplastic Composites.” *Journal of Adhesion Science and Technology* 23 (16): 2031–2046. doi:10.1163/016942409X12526743387809.

Lin, Yirong, Gregory Ehlert, and Henry A Sodano. 2009. “Increased Interface Strength in Carbon Fiber Composites through a ZnO Nanowire Interphase.” *Advanced Functional Materials* 19 (16) (August 24): 2654–2660. doi:10.1002/adfm.200900011.

Lipic, P. M., F. S. Bates, and M. A. Hillmyer. 1998. “Nanostructured Thermosets from Self-Assembled Amphiphilic Block Copolymer/epoxy Resin Mixtures.” *Journal of the American Chemical Society* 120 (35): 8963–8970.

Liu, Jian, Fengtao Fan, Zhaochi Feng, Lei Zhang, Shiyang Bai, Qihua Yang, and Can Li. 2008. “From Hollow Nanosphere to Hollow Microsphere: Mild Buffer Provides Easy Access to Tunable Silica Structure.” *Journal of Physical Chemistry C* 112 (42) (October): 16445–16451. doi:10.1021/jp804161f.

Lou, Xiong Wen (David), Lynden A. Archer, and Zichao Yang. 2008. “Hollow Micro-/Nanostructures: Synthesis and Applications.” *Advanced Materials* 20 (21): 3987–4019. doi:10.1002/adma.200800854.

Luo, Xiaolie, Sixun Zheng, Naibin Zhang, and Dezhu Ma. 1994. “Miscibility of Epoxy Resins/poly (ethylene Oxide) Blends Cured with Phthalic Anhydride.” *Polymer* 35 (12): 2619–2623.

Madhukar, Ms, and Lt Drzal. 1991. “Fiber-Matrix Adhesion and Its Effect on Composite Mechanical-Properties .2. Longitudinal (0-Degrees) and Transverse (90-Degrees) Tensile and Flexure Behavior of Graphite Epoxy Composites.” *Journal of Composite Materials* 25 (8) (August): 958–991.

Mandell, J, J Chen, and F McGarry. 1980. “A Microdebonding Test for In-Situ Fiber-Matrix Bond Strength and Moisture Effects.” In , 26–d. New Orleans, LA: Society of the Plastics Industry.

Marshall, P., and J. Price. 1991. “Topography of Carbon Fibre Surfaces.” *Composites* 22 (5): 388–393.

Marur, Prabhakar R. 2005. “Effective Elastic Moduli of Syntactic Foams.” *Materials Letters* 59 (14): 1954–1957.

Miller, A. C., and J. C. Berg. 2003a. “Effect of Silane Coupling Agent Adsorbate Structure on Adhesion Performance with a Polymeric Matrix.” *Composites Part a-Applied Science and Manufacturing* 34 (4): 327–332. doi:10.1016/S1359-835X(03)00051-4.

Miller, A. C., and J. C. Berg. 2003. 2003b. “Unexpected Behavior between Polystyrene and Untreated and Silane-Treated Glass Beads in Filled Polymeric Composites.” *Journal of Applied Polymer Science* 89 (2) (July 11): 521–526. doi:10.1002/app.12303.

Miller, A. C., S. Minko, and J. C. Berg. 2001. “Application of Acoustic Emission Measurements to Investigate Adhesion in Filled Polymeric Composites.” *Journal of Adhesion* 75 (3): 257–266. doi:10.1080/00218460108029604.

Mossakovskii, V.I, and M.T Rybka. 1964. “Generalization of the Grippith-Sneddon Criterion for the Case of a Nonhomogeneous Body.” *Journal of Applied Mathematics and Mechanics* 28 (6): 1277–1286. doi:10.1016/0021-8928(64)90039-5.

Nairn, Ja. 1992. “A Variational Mechanics Analysis of the Stresses Around Breaks in Embedded Fibers.” *Mechanics of Materials* 13 (2) (April): 131–154. doi:10.1016/0167-6636(92)90042-C.

Nemoto, Tomoyuki, Jun Takagi, and Masahiro Ohshima. 2008a. “Nanoscale Cellular Foams from a Poly (propylene)-Rubber Blend.” *Macromolecular Materials and Engineering* 293 (12): 991–998.

Nemoto, Tomoyuki, Jun Takagi, and Masahiro Ohshima. 2008b. “Control of Bubble Size and Location in Nano-/Microscale Cellular Poly (propylene)/Rubber Blend Foams.” *Macromolecular Materials and Engineering* 293 (7): 574–580.

Nguyen, Felix N., and John C. Berg. 2004. “The Effect of Vinyl Alcohol Content on Adhesion Performance in Poly (vinyl Butyral)/glass Systems.” *Journal of Adhesion Science and Technology* 18 (9): 1011–1026.

Nguyen, Felix N., and John C. Berg. 2005. “Use of an Optical–Mechanical Test Combined with Acoustic-Emission Techniques to Study Adhesion in Filled Polymeric Composites.” *The Journal of Adhesion* 81 (7-8) (July): 823–841. doi:10.1080/00218460500189166.

Nguyen, Felix N., and John C. Berg. 2008. “Novel Core-Shell (dendrimer) Epoxy Toughеners: Processing and Hot-Wet Performance.” *Composites Part a-Applied Science and Manufacturing* 39 (6): 1007–1011. doi:10.1016/j.compositesa.2008.03.005.

Nguyen, Felix N., Alfred Haro, and Yochioka kenichi. 2013. “Effects of a Nanomaterial Toughened Interphase in Carbon Fiber Reinforced Polymer Composite.” In Wichita, KS.

Nguyen, Felix N., Alfred Haro, Swezin Tun, and Kenichi Yoshioka. 2013. “Hard Nanomaterial Toughened Carbon Fiber Reinforced Polymer Composite.” In Wichita, KS: Society for the Advancement of Material and Process Engineering.

Nguyen, Felix N., Alfred Haro, and Kenichi Yoshioka. 2012. “Maximizing Fiber-to-Composite Strength Translation with a Nanomaterial Reinforced Interphase.”

Ohsawa, T., A. Nakayama, M. Miwa, and A. Hasegawa. 1978. “Temperature-Dependence of Critical Fiber Length for Glass Fiber-Reinforced Thermosetting Resins.” *Journal of Applied Polymer Science* 22 (11): 3203–3212. doi:10.1002/app.1978.070221115.

Peter, Sameer L., and Eyassu Woldesenbet. 2009. “Nanoclay and Microballoons Wall Thickness Effect on Dynamic Properties of Syntactic Foam.” *Journal of Engineering Materials and Technology* 131 (2): 021007. doi:10.1115/1.3078302.

Plastics and Rubber Institute, and British Plastics Federation, ed. 1986. *Fillers: Proceedings of the Joint Conference of the Plastics and Rubber Institute and the British Plastics Federation, March 1986.* London, England; New York, NY, USA: Plastics and Rubber Institute ; Elsevier Science Pub. Co.

Plueddemann, Edwin P. 1982. *Silane Coupling Agents*. Springer.

Porfiri, Maurizio, and Nikhil Gupta. 2009. “Effect of Volume Fraction and Wall Thickness on the Elastic Properties of Hollow Particle Filled Composites.” *Composites Part B: Engineering* 40 (2): 166–173.

Pukanszky, B., and G. Voros. 1996. “Stress Distribution around Inclusions, Interaction, and Mechanical Properties of Particulate-Filled Composites.” *Polymer Composites* 17 (3) (June): 384–392. doi:10.1002/pc.10625.

Qingfeng Wu, C. B. Park, Nanqiao Zhou, and Wenli Zhu. 2009. “Effect of Temperature on Foaming Behaviors of Homo- and Co-Polymer Polypropylene/Polydimethylsiloxane Blends with CO2.” *Journal of Cellular Plastics* 45 (4) (July 1): 303–319. doi:10.1177/0021955X09102399.

Ramanathan, T., M. A. Muthumanickam, and K. Subramanian. 2000. “Study on the Effect of Loading Rate on Flexural Strength of Glass/polyester Composites as a Function of Span-to-Depth Ratio and Fiber Volume Fraction.” *Materials and Manufacturing Processes* 15 (6): 845–852. doi:10.1080/10426910008913025.

Rao, V., and Lt Drzal. 1991. “The Dependence of Interfacial Shear-Strength on Matrix and Interphase Properties.” *Polymer Composites* 12 (1) (February): 48–56. doi:10.1002/pc.750120108.

Renner, Károly, Min Soo Yang, János Móczó, Hyoung Jin Choi, and Béla Pukánszky. 2005. “Analysis of the Debonding Process in Polypropylene Model Composites.” *European Polymer Journal* 41 (11) (November): 2520–2529. doi:10.1016/j.eurpolymj.2005.05.025.

Rosen, B. W. 1965. “Mechanics of Composite Strengthening.” (January 1): 37–75.

Schacht, S., Q. Huo, I. G. VoigtMartin, G. D. Stucky, and F. Schuth. 1996. “Oil-Water Interface Templating of Mesoporous Macroscale Structures.” *Science* 273 (5276) (August 9): 768–771. doi:10.1126/science.273.5276.768.

Schmidt, Wolfgang, and Georg Roessling. 2006. “Novel Manufacturing Process of Hollow Polymer Microspheres.” *Chemical Engineering Science* 61 (15) (August): 4973–4981. doi:10.1016/j.ces.2006.03.021.

Schulz, Mark F., Ashish K. Khandpur, Frank S. Bates, Kristoffer Almdal, Kell Mortensen, Damian A. Hajduk, and Sol M. Gruner. 1996. “Phase Behavior of Polystyrene-Poly (2-Vinylpyridine) Diblock Copolymers.” *Macromolecules* 29 (8): 2857–2867.

Shankar, Ravi, and S. Sankaran. 2005. “Short-Beam Three-Point Bend Test Study in Syntactic Foam. Part III: Effects of Interface Modification on Strength and Fractographic Features.” *Journal of Applied Polymer Science* 98 (2): 687–693.

Sjögren, B. A., and L. A. Berglund. 1997. “Failure Mechanisms in Polypropylene with Glass Beads.” *Polymer Composites* 18 (1): 1–8.

Tamai, H., T. Sumi, and H. Yasuda. 1996. “Preparation and Characteristics of Fine Hollow Carbon Particles.” *Journal of Colloid and Interface Science* 177 (2) (February 10): 325–328. doi:10.1006/jcis.1996.0038.

Thio, Yonathan S., Junxian Wu, and Frank S. Bates. 2006. “Epoxy Toughening Using Low Molecular Weight Poly(hexylene oxide)−Poly(ethylene Oxide) Diblock Copolymers.” *Macromolecules* 39 (21) (October): 7187–7189. doi:10.1021/ma052731v.

Thio, Yonathan S., Junxian Wu, and Frank S. Bates. 2009. “The Role of Inclusion Size in Toughening of Epoxy Resins by Spherical Micelles.” *Journal of Polymer Science Part B: Polymer Physics* 47 (11) (June 1): 1125–1129. doi:10.1002/polb.21707.

Thostenson, E. T., W. Z. Li, D. Z. Wang, Z. F. Ren, and T. W. Chou. 2002. “Carbon Nanotube/carbon Fiber Hybrid Multiscale Composites.” *Journal of Applied Physics* 91 (9) (May 1): 6034–6037. doi:10.1063/1.1466880.

Weitzsacker, C. L., M. Xie, and L. T. Drzal. 1997. “Using XPS to Investigate Fiber Matrix Chemical Interactions in Carbon-Fiber-Reinforced Composites.” *Surface and Interface Analysis* 25 (2) (February): 53–63. doi:10.1002/(SICI)1096-9918(199702)25:2<53::AID-SIA222>3.3.CO;2-5.

Williams, J. G., M. E. Donnellan, M. R. James, and W. L. Morris. 1990. “Properties of the Interphase in Organic Matrix Composites.” *Materials Science and Engineering: A* 126 (1): 305–312.

Woldesenbet, Eyassu, Nikhil Gupta, and H. Dwayne Jerro. 2005. “Effect of Microballoon Radius Ratio on Syntactic Foam Core Sandwich Composites.” *Journal of Sandwich Structures and Materials* 7 (2): 95–111.

Wouterson, E. M., F. Y. C. Boey, X. Hu, and S. C. Wong. 2005. “Specific Properties and Fracture Toughness of Syntactic Foam: Effect of Foam Microstructures.” *Composites Science and Technology* 65 (11-12) (September): 1840–1850. doi:10.1016/j.compscitech.2005.03.012.

Wouterson, Erwin M., Freddy YC Boey, Xiao Hu, and Shing-Chung Wong. 2004. “Fracture and Impact Toughness of Syntactic Foam.” *Journal of Cellular Plastics* 40 (2): 145–154.

Wu, Hf, and Cm Claypool. 1991. “An Analytical Approach of the Microbond Test Method Used in Characterizing the Fiber Matrix Interface.” *Journal of Materials Science Letters* 10 (5) (March 1): 260–262. doi:10.1007/BF00735651.

Wu, Junxian, Yonathan S Thio, and Frank S. Bates. 2005. “Structure and Properties of PBO-PEO Diblock Copolymer Modified Epoxy.” *Journal of Polymer Science Part B: Polymer Physics* 43 (15) (August 1): 1950–1965. doi:10.1002/polb.20488.

Yilmaz, Y. I. 2002. “Analyzing Single Fiber Fragmentation Test Data by Using Stress Transfer Model.” *Journal of Composite Materials* 36 (5): 537–551. doi:10.1106/021998302021465.

Ying-long, Yuan, and Lu Zi-xing. 2004. “Modulus Prediction and Discussion of Reinforced Syntactic Foams with Coated Hollow Spherical Inclusions.” *Applied Mathematics and Mechanics* 25 (5): 528–535.

Yokoyama, H., and K. Sugiyama. 2005. “Nanocellular Structures in Block Copolymers with CO2-Philic Blocks Using CO2 as a Blowing Agent: Crossover from Micro- to Nanocellular Structures with Depressurization Temperature.” *Macromolecules* 38 (25) (December 13): 10516–10522. doi:10.1021/ma051757j.

Zettlemoyer, Albert C. 1969. *Nucleation,*. New York: M. Dekker.

Zhang, Fu-Hua, Rong-Guo Wang, Xiao-Dong He, Chao Wang, and Li-Ning Ren. 2009. "Interfacial Shearing Strength and Reinforcing Mechanisms of an Epoxy Composite Reinforced Using a Carbon Nanotube/carbon Fiber Hybrid." *Journal of Materials Science* 44 (13) (April 28): 3574–3577. doi:10.1007/s10853-009-3484-x.

Zhang, Yihe, Fengzhu Lv, Shaojian Ke, Li Yu, Haitao Huang, and H. L. W. Chan. 2011. "Effect of Hollow Structure and Covalent Bonding on the Mechanical Properties of Core–shell Silica Nanoparticles Modified Poly (methyl Acrylate) Composites." *Materials Chemistry and Physics* 129 (1): 77–82.

Zhao, S, L Schadler, R Duncan, H Hillborg, and T Auletta. 2008. "Mechanisms Leading to Improved Mechanical Performance in Nanoscale Alumina Filled Epoxy." *Composites Science and Technology* 68 (14) (November): 2965–2975. doi:10.1016/j.compscitech.2008.01.009.

Zhao, Z. G., L. J. Ci, H. M. Cheng, and J. B. Bai. 2005. "The Growth of Multi-Walled Carbon Nanotubes with Different Morphologies on Carbon Fibers." *Carbon* 43 (3): 663–665. doi:10.1016/j.carbon.2004.10.013.

Zhou, Lm, Jk Kim, C. Baillie, and Yw Mai. 1995. "Fracture-Mechanics Analysis of the Fiber Fragmentation Test." *Journal of Composite Materials* 29 (7): 881–902.

Zhou, Lm, Yw Mai, and C. Baillie. 1994. "Interfacial Debonding and Fiber Pull-Out Stresses .5. a Methodology for Evaluation of Interfacial Properties." *Journal of Materials Science* 29 (21) (November 1): 5541–5550. doi:10.1007/BF00349945.

Zhou, Yuanxin, Evert White, Mahesh Hosur, and Shaik Jeelani. 2010. "Effect of Particle Size and Weight Fraction on the Flexural Strength and Failure Mode of TiO2 Particles Reinforced Epoxy." *Materials Letters* 64 (7) (April): 806–809. doi:10.1016/j.matlet.2010.01.016.

Zinck, P., E. Mader, and J. F. Gerard. 2001. "Role of Silane Coupling Agent and Polymeric Film Former for Tailoring Glass Fiber Sizings from Tensile Strength Measurements." *Journal of Materials Science* 36 (21) (November): 5245–5252. doi:10.1023/A:1012410315601.

Zouari, R., A. Benhamida, and H. Dumontet. 2008. "A Micromechanical Iterative Approach for the Behavior of Polydispersed Composites." *International Journal of Solids and Structures* 45 (11): 3139–3152.

Appendix A – Matlab code for modeling normal stress at a pole in a particulate composite

The code for determining the stress concentration in the direction of applied stress, that is, normal to the pole each particulate, in a particulate composite is given here. The code was written for Matlab, but does not require any special functions, and could be easily ported to another language. The code is broken up into three "m-files". The first, *stressconc.m* calls the *makecomposite.m* file, which returns values for the center of each particulate, determined randomly, and the number of spheres, calculated from the volume fraction, which is the input for the file, *volfrac*. Then, it calculates the stress concentration in each Cartesian direction by calling *Goodiercartesianpoint.m*, which has inputs of the location of the pole for which the stress concentration is being calculated and the location of the center

stressconc.m

```
function [maxpersphere] = stressconc(volfrac)

[centers,numsphere] = makecomposite(volfrac);

poles=ones(2,numsphere,3);

for  i = 1:numsphere,
   poles(1,i,1) = centers(i,1)+325;
   poles(2,i,1) = centers(i,1)-325;
   poles(1,i,2) = centers(i,2);
   poles(2,i,2) = centers(i,2);
   poles(1,i,3) = centers(i,3);
   poles(2,i,3) = centers(i,3);
end

polestressconc = ones(2,numsphere);
for i = 1:numsphere,
   for j=1:numsphere,
      if (i ~= j),
```

```
        polestressconc(1,i) = polestressconc(1,i) +
Goodiercartesianpoint(poles(1,i,1),poles(1,i,2),poles(1,i,3),centers(j,1), centers(j,2), centers(j,3));
        polestressconc(2,i) = polestressconc(2,i) +
Goodiercartesianpoint(poles(2,i,1),poles(2,i,2),poles(2,i,3), centers(j,1), centers(j,2),
centers(j,3));
      end
   end
end

maxpersphere = sort(max(polestressconc(1,:),polestressconc(2,:)))';
```

make composite.m

```
function [centers,numsphere] = makecomposite(volfrac);

meshsize = 10000000;
length = 10000; %x
width = 10000;  %y
height = 3000;  %z
samplevol = width.*height.*length;
radius = 650./2;

numsphere = round(samplevol.*volfrac./((4./3).*pi.*radius.^3));

%celllength = (samplevol./meshsize).^(1./3);

loc = ones(numsphere,3);
for i = 1:numsphere,
   loc(i,1) = round(length.*rand(1));
   loc(i,2) = round(width.*rand(1));
   loc(i,3) = round(height.*rand(1));
end

overlapcheck = 1;
while(overlapcheck>0);
   overlapcheck = 0;
   for i = 1:numsphere,
      for j = i+1:numsphere,
         if sqrt((loc(j,1)-loc(i,1))^2+(loc(j,2)-loc(i,2))^2+(loc(j,3)-loc(i,3))^2)<650 ...
            || loc(j,1)-325<0 || loc(j,1)+325>length || loc(j,2)-325<0 ||loc(j,2)+325<width ...
            || loc(j,3)-325<0 || loc(j,3)+325<0
            loc(j,1) = round(length.*rand(1));
            loc(j,2) = round(width.*rand(1));
            loc(j,3) = round(height.*rand(1));
            overlapcheck = 1;
```

```
        end
      end
   end
end
hold off;

% for i = 1:numsphere,
%     [x,y,z] = sphere;
%     x=x.*325+loc(i,1);
%     y=y.*325+loc(i,2);
%     z=z.*325+loc(i,3);
%     colormap bone;
%     surf(x,y,z);
%     axis([0 length 0 width 0 height -.5 .5]);
%     pbaspect([length/height width/height height/height]);
%     hold on;
% end

%scatter3(loc(:,1),loc(:,2),loc(:,3))

centers = loc;
```

goodiercartesianpoint.m

```
function [sz]= Goodiercartesianpoint(x,y,z,m,n,o)

%xyz is the location of interest, mno is the point of

T = 1; %applied stress
a = 1; %inclusion radius
nu1 = .3; %possion's ratio of inclusion
nu2 = .4; %possion's ratio of matrix
G1 = 1; %bulk modulus of inclusion
G2 = 1000; %bulk modulus of matrix

%  distance
x = ((m-x).^2).^.5;
y = ((n-y).^2).^.5;
z = ((o-z).^2).^.5;


% finding the values for r, theta, and phi because the solution is in
% spherical coordinates.  r is nondimensionalized
r = sqrt(x.^2+y.^2+z.^2);
```

```
theta = acos(z./r);
phi = atan2(y,x);
r = r/325;


%solve for A, B, C, constansts found by Goodier
A = (-((a.^3).*T.*(G1-G2))./(8.*G1.*((7-5.*nu1).*G1+(8-10.*nu1).*G2))).*((1-2.*nu2).*(6-
5.*nu1)...
   .*2.*G1+(3+19.*nu2-20.*nu1.*nu2).*G2)./((1-2.*nu2).*2.*G1+(1+nu2).*G2)...
   +(a.^3).*(T.*(((1-nu1).*((1+nu2)./(1+nu1))-nu2).*G2)-((1-2.*nu2).*G1))./(4.*G1.*((1-
2.*nu2).*2.*G1+(1+nu2).*G2));
B = (((a.^5).*T.*(G1-G2))./(8.*G1.*((7-5.*nu1).*G1+(8-10.*nu1).*G2)));
C = (((a.^3).*T.*5.*(1-2.*nu1).*(G1-G2))./(8.*G1.*((7-5.*nu1).*G1+(8-10.*nu1).*G2)));

%solve for the stress vectors in spherical, using constants and A,B,C
rr = 2.*G1.*(2.*A./r.^3-(2.*nu1.*C./((1-2.*nu1).*r.^3)+12.*B./r.^5)+(-(2.*(5-nu1).*C)./((1-
2.*nu1).*r.^3)+36.*B./r.^5).*cos(2.*theta));
thetatheta = 2.*G1.*(-A./r.^3-(2.*nu1.*C)./((1-2.*nu1).*r.^3)-3.*B./r.^5)+((C./r.^3-
21.*B./r.^5).*cos(2.*theta));
phiphi = 2.*G1.*(-A./r.^3-(2.*(1-nu1).*C)./((1-2.*nu1).*r.^3)-9.*B./r.^5)+((3.*C./r.^3-
15.*B./r.^5).*cos(2.*theta));
%rtheta = 2.*G1.*(-(2.*(1+nu1).*C)./((1-2.*nu1).*a.^3)+24.*B./r.^5)+((3.*C./r.^3-
15.*B./r.^5).*cos(2.*theta));



transformmatrix= [sin(theta).*cos(phi) sin(theta).*sin(phi) cos(theta); cos(theta).*cos(phi)
cos(theta).*sin(phi) -sin(theta); -sin(theta) cos(phi) 0];
polarvector = [rr; thetatheta; phiphi];
%invtransfrommatrix = inv(transformmatrix);
cartvector = transformmatrix\polarvector;


%for i = 1:maxsize,
%    cartvector(:,:,i) = [sin(theta(i)).*cos(phi(i)) sin(theta(i)).*sin(phi(i)) cos(theta(i));
cos(theta(i)).*cos(phi(i)) cos(theta(i)).*sin(phi(i)) -sin(theta(i)); -sin(theta(i)) cos(phi(i)) 0];
%    polarvector(:,:,i) = [rr(i) thetatheta(i) phiphi(i)];
%end

%multiprod is an open source m-file for returning the mutltiplication of an
%nd array

%cartvector = permute(cartvector,[2 1 3]);
%polarvector = permute(polarvector,[2 1 3]);
%cartvector = multiprod(cartvector, polarvector);
```

```
%extract the cartesian stress vector

%sx = squeeze(cartvector(1,:,:,:)).*T;
%sy = squeeze(cartvector(2,:,:,:)).*T;
sz = squeeze(cartvector(3,:,:,:)).*T;
```

Appendix B - Other work on depositing nanoparticles on glass fibers

Chapter 4 discusses the published work on electrostatically depositing trimethoxysilane modified poly(ethylene imine) (SPEI) functionalized 16 – 100 nm silica nanoparticles on to glycidyloxypropyltrimethoxysilane (GPS) glass fibers to improve the interfacial shear strength. Prior to researching that specific system, a number of other topographical surface modifications were investigated including 175 nm polydisperse alumina, alumina adhered with a silica sol gel, triaminosilane functionalized alumina, high temperature sintered 100 nm silica particles, 250 nm and 100 nm triaminosilane and poly(ethyleneimine) (PEI) functionalized silica, 90 nm and 58 nm PEI functionalized silica, Ludox TMA 22 nm silica adhered with crosslinked GPS and electrostatically bound to a fiber functionalized with PEI. Although the end result, a roughened fiber surface, is the same for each of these systems, the sample preparation and performance varies widely. The methods and results for these systems are discussed here.

The single fiber fragmentation test is dependent on the fiber strength which can be significantly decreased by the extent of fiber handling, especially after the sizing has been removed. In this section, many IFSS values are higher than that reported in Chapter 4 due to differences in fiber handling. Thus, comparative conclusions can be made for the data presented in the following sections, but the absolute values of IFSS from this section and Chapter 4 should not be compared.

B.1 Experimental methods: methods general to all systems

In all cases the fibers used were E-glass (Fiberex, Inc., Leduc, Alberta, Canada), with a nominal diameter of 8.9 μm. The fibers were provided with a sizing which was removed by soaking the tow in a mixture of NoChromix and concentrated sulfuric acid overnight, and subsequently rinsed with deionized (DI) water. Processing of fibers after removing the protective sizing would reduce their strength. E-glass fibers are made from a mixture of mineral oxides including silica, calcium oxide, alumina, boron oxide, and magnesia. The acid treatment preferentially leaches aluminum and calcium, creating a silica rich surface.

The matrix was stoichiometric quantities of low molecular weight bisphenol A diglycidyl ether (BADGE) (EP-828, Miller-Stephenson, Danbury, CT) with m-phenylenediamine (mPDA) (Aldrich, St. Louis, MI). EP-828 was degassed under vacuum at 60°C with stirring for at least an hour, until off gassing stopped. The EP-828 and mPDA were mixed at 60°C until homogeneous immediately before use.

To prepare samples for the SFFT, first the mold was coated with a resin mold release, Frekote 55-NC (Henkel, Rocky Hill, CT) then heated to 100°C for one hour to remove adsorbed water and volatiles in the mold release. The use of a mold release agent with silicon molds was later found to be unnecessary, and may contaminate the fiber surface and should be avoided. Next, individual fibers were placed in silicone dog-bone shaped molds and were taped in place to keep them taught and straight. 0.8 ml of resin was placed in each dog-bone mold. The resin was cured at 75°C for two hours and post cured at 125°C for two hours. After curing the sample edges were sanded with 320 grit and 600 grit sand paper to ensure that the edges are defect free.

A dog-bone sample was placed in the miniature tensile test frame (St. John's Computer Machine, St. John's, MI), which is mounted to a microscope and was strained at 0.06 mm/mm min, a rate 20 times faster than what was used for the work discussed in Chapter 4. The slow strain rate used in Chapter 4 was necessary to prevent premature sample failure. Generally, fiber fragmentation starts at a strain of about 6% and reaches the final fragmentation length, or critical length, l_c, at 10%. The samples were strained to 12% to ensure that the l_c was obtained. A 25mm slide cover was placed on the sample to act as a consistent measure so the same portion of gauge length was examined each time.

B.2 Colloidal Alumina Modified particles

B.2.1 Methods

Alumina particles, NanoDur X1121W (Nanophase Technologies Corporation, Romeoville, IL) were provided with an undisclosed dispersant in water. The dispersant, assumed to be an organic surfactant, was removed by oxidizing with a NoChromix and concentrated sulfuric acid mixture. The resulting slurry was centrifuged and the supernatant was removed. The particles were re-suspended in DI H_2O and subsequently centrifuged repeatedly, until the supernatant was pH neutral, giving bare alumina particles in DI H_2O, which were diluted to 0.1 vol% solids. The point of zero charge (PZC) was determined by systematically varying the pH with KOH and HNO_3 and measuring the electrophoretic mobility using ZetaPALS (Brookhaven Instruments Corporation, Holtsville, NY).

The optimum pH for electrostatically depositing alumina on to E-glass fibers was determined by varying the pH of the alumina suspension with KOH and HNO_3 dipping the E-glass fiber into the suspension, and imaging the surfaces with SEM.

For single fiber fragmentation tests (SFFTs) desized E-glass fibers were dipped into a 0.1 wt% alumina dispersion with a pH of 4.1 and immediately removed. The coated fibers were then dried in a convection oven at 100°C or 200°C for one hour. Dog-bone test specimens were then made with the fibers using the methods described.

B.2.2 Results

The volume average particle diameter with no dispersant, as determined with dynamic light scattering, is 175 nm, but the colloid was very polydisperse and prone to aggregation. Based on scanning electron microscopy (SEM), the particle size the nominal primary particle size was between 10 and 100 nm. The point of zero charge (PZC), the pH at which there is no surface charge, is 6.1.

E-glass fibers have a PZC of 2.5 and the colloidal alumina has a PZC of 6.1, at a pH in that range the fiber would have a negative surface charge while the alumina would be positively charged, allowing for electrostatic deposition. Representative micrographs of surface coverages obtained with varying pH are shown in Fig. B.1. The optimum pH was found to be between 4 and 4.5. At a higher pH, the magnitude of surface charge on the alumina is diminished, reducing electrostatic stabilization, leading to aggregation. At a lower pH there is insufficient surface charge on the fiber to cause electrostatic deposition.

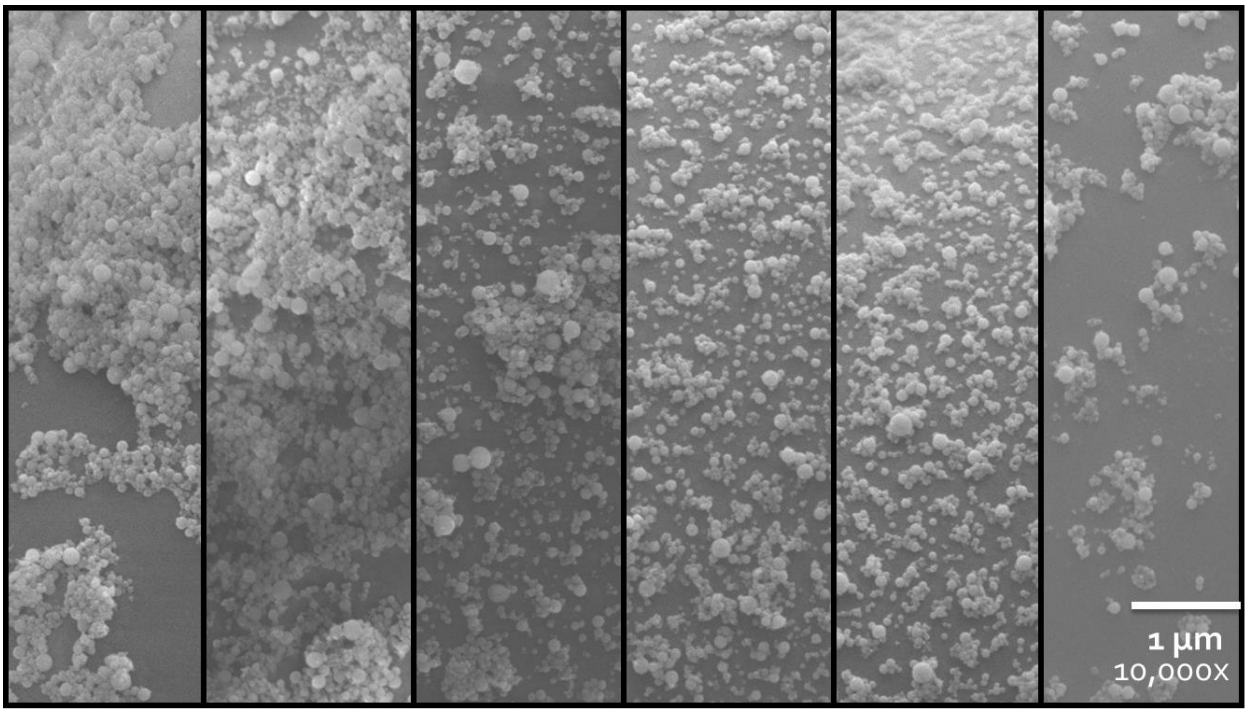

a) b) c) d) e) f)

Figure B.1. Colloidal alumina electrostatically deposited on an E-glass surface at a pH of a) 8.0, b) 7.0, c) 5.0, d) 4.5, e) 4.0, f) 3.5

An SEM micrograph of an alumina coated fiber, at lower magnification, is shown in Fig. B.2. Although surface coverage is uniform on the length scale of several microns, at smaller length scales there are regions of poor surface coverage and large aggregates.

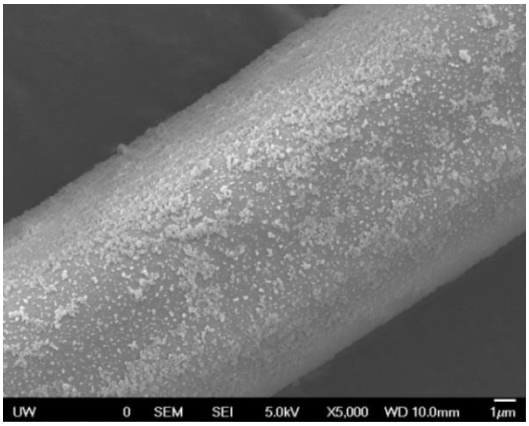

Figure B.2. E-glass fiber coated with alumina particles at a pH of 4.1

Using the determined optimum pH of 4.1 SFFT were performed. Two different drying temperatures were used, 100°C and 200°C. There was a very slight increase in IFSS with the addition with alumina particles when compared to a bare fiber, shown in Fig. B.3. The addition of colloidal alumina between the fiber/matrix interface would effectively increase the roughness of the matrix surface in contact with the fiber surface, leading to a slight increase in the apparent IFSS. However, the low level of adhesion (as no adhesion promoter was used) and the large number of aggregates limited the IFSS. There was no influence of drying temperature.

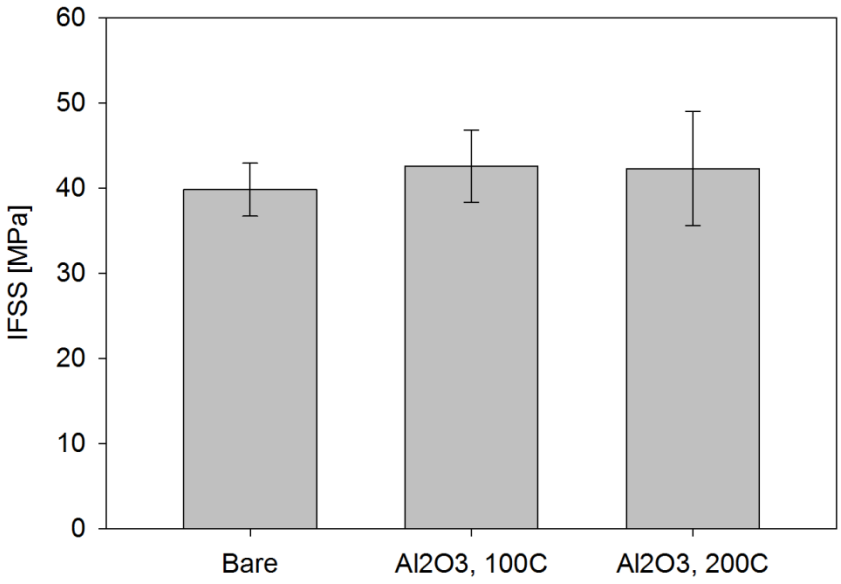

Figure B.3. The IFSS results for bare E-glass coated with alumina particles, dried at 100°C and 200°C

B.3 Colloidal Alumina with a silica sol film adhesive

Simply depositing alumina particles on to the fiber surface is not adequate to significantly increasing the IFSS of the system. Another method was employed; after depositing alumina particles on the fiber surface the fiber was then coated with a silica layer made using traditional sol gel thin film synthesis techniques. If the thin film were strong, and covalently bound to the fiber and alumina particles, it could approximately be considered an extension of fiber itself, in

the radial direction, creating a roughened fiber surface in a system made entirely from mineral oxides.

B.3.1 Methods

The sol preparation and thin film formation were outlined by Chan et al (C. M. Chan, G. Z. Cao, H. Fong, M. Sarikaya, T. Robinson, and L. Nelson, *J. Mater. Res.*, vol. 15, no. 1, pp. 148–154, Jan. 2000.) Tetraethylorthosilicate (TEOS), ethanol, water and nitric acid were combined to make a molar ratio of $1:3.8:5:4.8x10^{-3}$ respectively. The solution was mixed at 400 RPM at 60°C for 90 min with a water-cooled condenser at ambient pressure. The sol was then diluted with 200 proof ethanol to a 1:2 volume ratio, sol to ethanol.

Desized E-glass fibers were dipped in a 0.05 vol% Al_2O_3 suspension, with a pH of 4.31, depositing a layer of the particles on the surface. The alumina coated fibers were then were submerged in the sol and withdrawn at 35 or 10 mm/min. For one sample set, the fibers were withdrawn at 35 mm/min while being dried by flowing nitrogen over the surface as they were removed to increase the thin film thickness. Three different films were generated, in order of increasing thickness: 10 mm/min, 35 mm/min and 35 mm/min with N_2 drying. Finally, the sol and alumina coated fibers were heated at 150°C for 2 hours to encourage crosslinking in the film and to drive off any residual solvent. The prepared fibers were then made into SFFT specimens, as described above.

B.3.2 Results and discussion

The sol, or colloidal solution, was prepared via acid catalyzed hydrolysis, and subsequent condensation polymerization of TEOS, generating very small, reactive colloidal particles. If a flat surface is withdrawn from the sol, the subtended liquid will evaporate, leaving behind the colloidal particles. The thickness of the sol film is dependent on the rate the fiber is withdrawn,

solvent viscosity, and the rate of solvent evaporation, as illustrated in Fig. B.4. If this film of colloidal particles is adequately dried further, condensation between particles will occur, and if they are small enough and closely packed, they will bond into a film. Heating to higher temperatures, ~500°C and above, will sinter the particles generating a denser, more mechanically robust film.

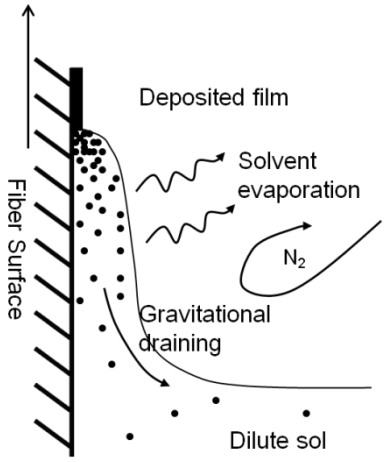

Figure B.4. A schematic of the physical phenomenon occurring during dip coating to generate a sol thin film

A SEM micrograph of the coated fiber is shown in Fig. B.5. No evidence of a thin film could be seen. The IFSS results of the thin film and alumina coated fibers are shown in Fig. B.5.

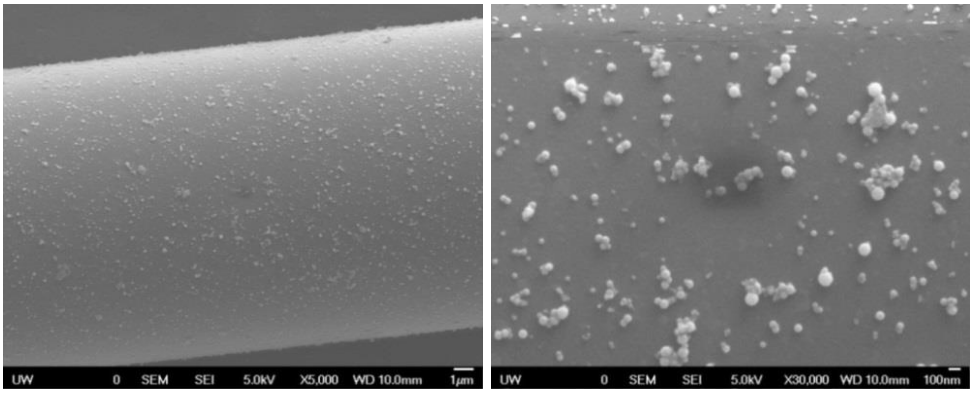

(a) (b)

Figure B.5. E-glass fiber coated with alumina particles, dipped and withdrawn from the silica sol at a) 35 mm/min with no drying at 5,000x and b) 30,000x

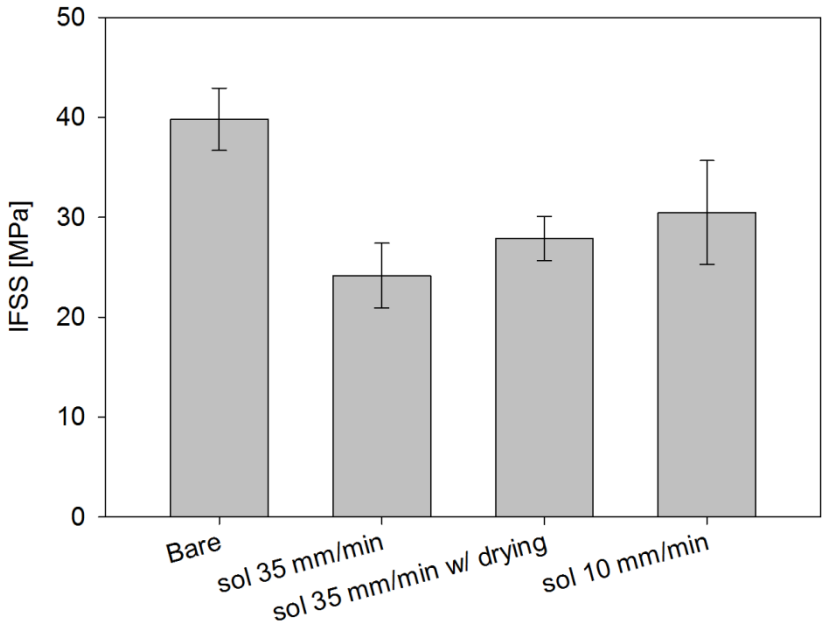

Figure B.6. A comparison of the IFSS of glass fibers surface treated with different methodologies. The meaning of the column descriptions are as follows: "bare", fibers just stripped of the sizing, "sol 35 mm/min", bare fibers coated with alumina particles withdrawn from the silica sol at 35 mm/min with no drying, "w/ drying", bare fibers coated with alumina particles withdrawn from the silica sol at 35 mm/min *with drying*, "sol 10 mm/min", bare fibers coated with alumina particles withdrawn from the silica sol at 10 mm/min with no drying.

There appears to be no IFSS dependence on the silica film thickness; it invariably reduces the strength of the fiber/matrix interface. This could be from poor film strength, poor film-fiber adhesion, or poor film-matrix adhesion.

B.4 Direct annealing of silica particles to the fiber surface

In another approach, silica particles were directly annealed to the fiber surface by coating the fiber with the particles and heating to 550°C to cause the fiber and particles to fuse, theoretically increasing the fiber roughness without depending on an adhesive.

B.4.1 Methods

100 nm silica particles (Fiber Optic Center, New Bedford, MA) were first functionalized with glycidyloxypropyltrimethoxysilane (GPS) (Sigma, St. Louis, MI). 0.37 vol% silica spheres were suspended in 190 proof ethanol, then the pH was reduced to 4.5 with glacial acetic acid. 0.5 vol% GPS was added, and the suspension was mixed for 90 min. The particles were centrifuged at 7,000 RPM for 5 min, the supernatant was discarded, and the particles were diluted to 0.1 vol% in DI H_2O with sonication, heated to 85°C and 0.5 vol% poly(ethyleneimine) (PEI) (Sigma, St. Louis, MI) MW = 750,000 g/mol, MN = 60,000 g/mol, the line drawing of the chemical formula is shown in Fig. B.7, was added while mixing at 400 RPM. The reaction was performed at elevated temperatures to increase the speed of reaction, and it was found that if the PEI was added at room temperature, flocs would form. The suspension was stirred for 90 min. The suspension was then centrifuged 7,000 RPM for 5 min, suspended in DI H_2O, then centrifuged and dispersed in water to 0.1 vol% to "rinse" the particles and the pH was reduced to 4.5 with nitric acid.

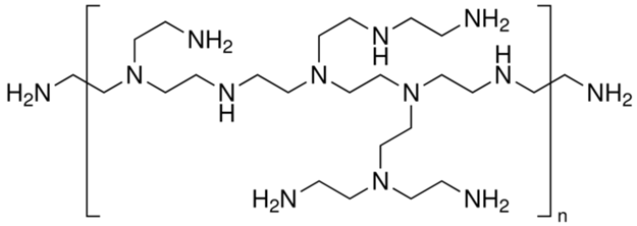

Figure B.7. The linear molecular formula of poly(ethyleneimine) (PEI)

Desized E-glass fibers were GPS functionalized. 0.5 vol% GPS was mixed with 190 proof ethanol, the pH was reduced to 4.5 with glacial acetic acid and mixed for 30 min, then the bare fibers were submerged for 60 min, rinsed with methanol and dried at 100°C for 5 min. The functionalized fibers were dipped in the PEI functionalized silica suspension and immediately removed. The particle coated fibers were placed on a ceramic tile and put a muffle furnace (Thermolyne F48025-60, Thermo Scientific, Waltham, MA), the temperature was ramped at 20°C/min to 830°C or 600°C for one hour, and 500°C or 550°C for 30 min.

To determine the IFSS the residual strength of the heat treated fibers needed to be determined. The fibers were subject to a constant displacement rate of 0.5 mm/min using an "inchworm" linear motor (Burleigh, Newton, NJ). The force was measured with a laboratory balance (AE200, Mettler, Columbus, OH).

B.4.2 Results

The particles were functionalized to achieve a positive surface charge, to take advantage of electrostatics to deposit the particles on the surface. At neutral pH the dynamic light scattering measured diameter of the bare silica was 160 nm and the diameter of the PEI functionalized silica particles was 234 nm. The bare particles were larger than the reported value because of aggregates that could not be broken up by sonication. The increase in measured diameter is likely a combination of an increase in hydrodynamic diameter from deposited PEI and an increase in aggregation.

The fibers, even after GPS functionalization, had a negative surface charge. Typical mobilities of bare silica, GPS functionalized silica, and PEI functionalized silica are given in Table B.1. The fibers were functionalized to promote particle adhesion via epoxide ring opening

of the GPS with the amines on the PEI functionalized particle. The particles needed to be well adhered to survive handling prior to fusing. Later, it was determined that PEI functionalized particles remained well adhered to fibers without GPS functionalization, likely from Van der Waal forces and acid-base interactions.

Table B.1. The mobilities of silica particles with no functionalization, GPS treatment, and PEI treatment

Material	**Mobility [(μm/cm)/(s V)]**	**pH**
Bare silica	-5.68	~7
GPS silica	-3.31	~7
PEI silica	+5.26	4.49

Initially the particle coated fibers were heated to 830°C for 1 hour, a reported typical softening temperature of E-glass, however, the fibers disintegrated. 600°C also caused fiber disintegration, while 500°C had no apparent effect on morphology, as determined by SEM. 30 min at 550°C appeared to fuse the silica particles to the surface of the glass, shown in Fig. B.8a. Some regions of the fibers show silica particles that had fused to themselves, shown in Fig. B.8b.

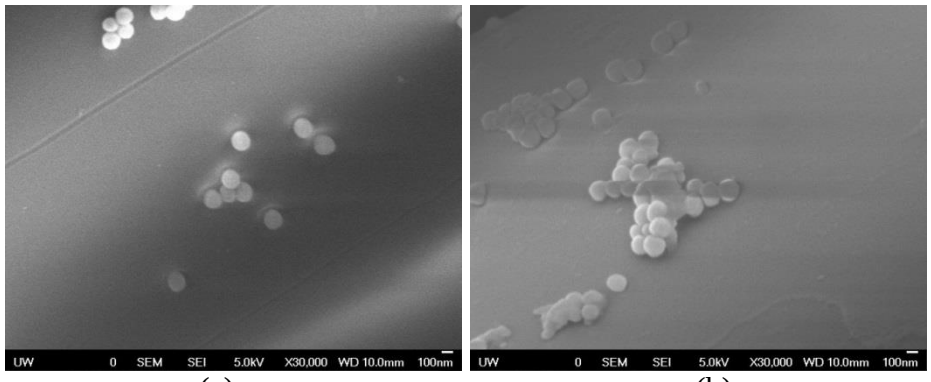

(a) (b)

Figure B.8. Silica particles a) fused to the E-glass surface and b) fused together

It is possible to fuse silica to E-glass fibers, but it has been shown in composite recycling that high temperature matrix removal significantly weakens the fiber (Feih et al. 2011). Thus it was necessary to test the residual strength of the fibers after heat treatment. The results of stress at failure versus the fiber length are shown in Fig. B.9. Strength is plotted against length because it is assumed that flaws act as stress concentrators, leading to a lower applied stress necessary to cause fiber failure. As the length of the fiber is reduced, the likelihood of having a major flaw is reduced, thus, by extrapolating to an infinitesimally small fiber length, the effect of inherent flaws is avoided.

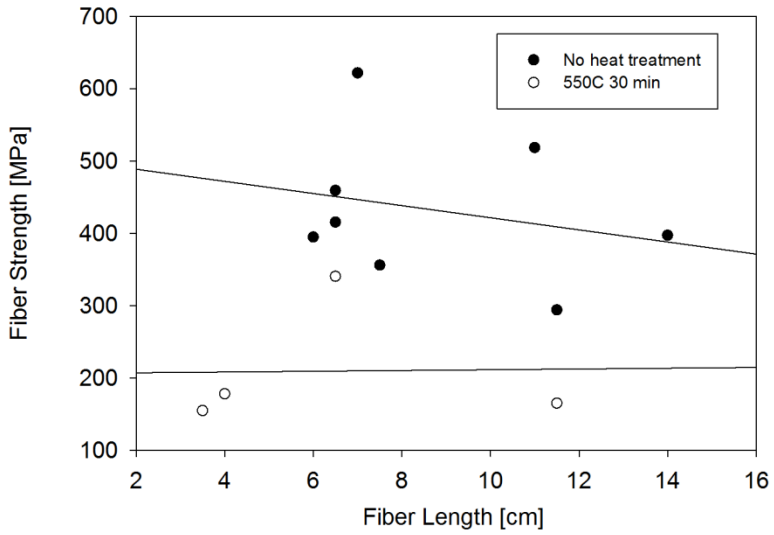

Figure B.9. The strength of bare fibers and fibers heat treated at 550°C for 30 min in air as a function of fiber length.

Although, the values are approximate, given the limited number data points that were gathered because of the difficulty in fiber preparation, it can be seen that the heat treatment reduces fiber strength by about half.

Taking into account the reduction in fiber strength the IFSS was found to be reduced after high temperature annealing, shown in Fig. B.10.

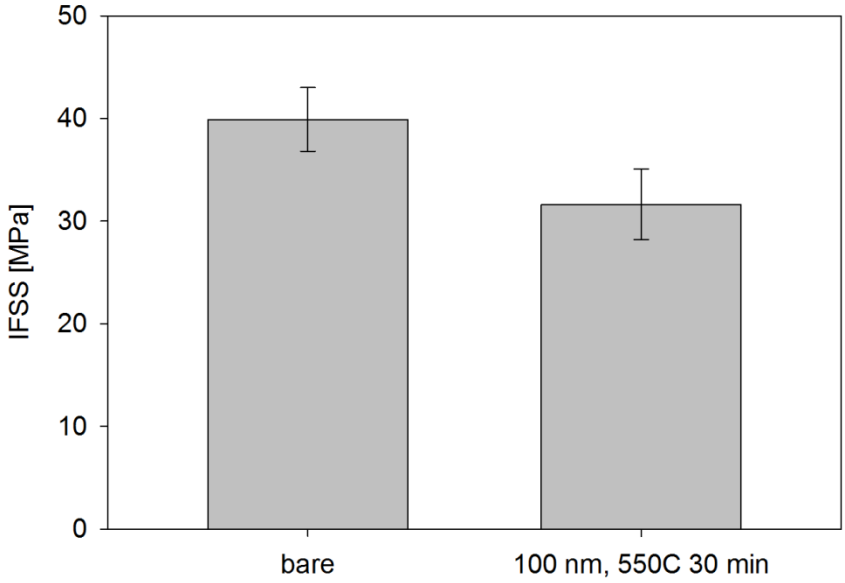

Figure B.10. IFSS of bare E-glass fibers and E-glass fibers electrostatically coated with 161 nm PEI coated silica heat treated at 550°C for 30 min

Although it is possible to use high temperature annealing to sinter colloidal silica to an E-glass fiber surface, doing so significantly reduces the fiber strength, without increasing the IFSS.

B.5 Triaminosilane functionalized 250 nm silica and alumina

Another approach to increasing the surface roughness of E-glass fibers is to covalently bond colloidal particles to the fiber surface. Functionalizing the fibers with GPS is often done to improve adhesion with the matrix by covalently bonding the fiber to the matrix. The epoxide rings on the surface are reactive with a number of different amine chemistries, offering a number of possibilities. 250 nm silica particles and 175 nm polydisperse alumina were functionalized with (3-trimethoxypropylsilane)diethylenetriamine (triaminosilane) (Aldrich, St. Louis, MI). It was postulated that the amino groups could then covalently bond to the epoxide groups on the fiber.

B.5.1 Methods

The functionalization was similar to the GPS functionalization of the 100 nm silica described above. 0.37 vol% mineral oxide was added to 190 proof ethanol, dispersed with stirring and sonication. 0.5 vol% of triaminosilane was added and the pH was adjusted to 4.5 with glacial acetic acid and stirred for 90 min. The particles were then centrifuged out of suspension, then dispersed in DI H_2O to 0.1 vol% solids, a processes that was repeated five times because a low speed centrifuge was used. The pH of the final solution was adjusted to 4.5 with nitric acid.

GPS functionalized fibers were coated with the colloidal suspension at room temperature for 10 s. One set of fibers were coated with triaminosilane 250 nm silica at 85°C for 60 s. The fiber surfaces were imaged with SEM and the IFSS was determined with the SFFT.

B.5.2 Results

The electrostatic depositions of triaminosilane functionalized alumina, shown in Fig. B.11, 250 nm PEI functionalized silica, shown in Fig. B.12 and 250 nm PEI functionalized silica dipped in an 85°C suspension, shown in Fig. B.13, on to GPS functionalized E-glass fibers was good, achieving a near monolayer in the silica samples and uniform coverage in the alumina samples.

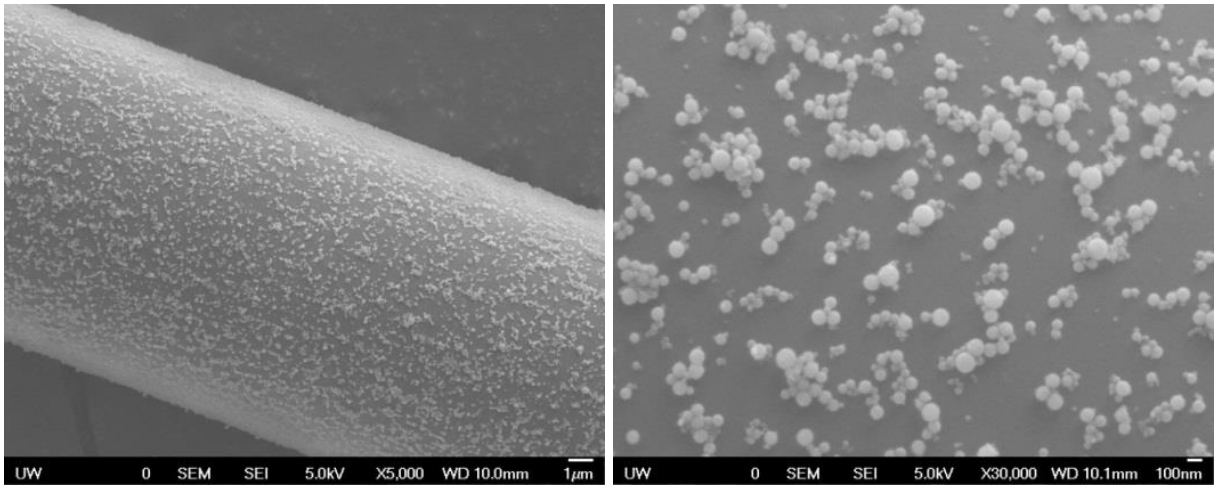

Figure B.11. Triaminosilane functionalized alumina coated particle on E-glass fibers

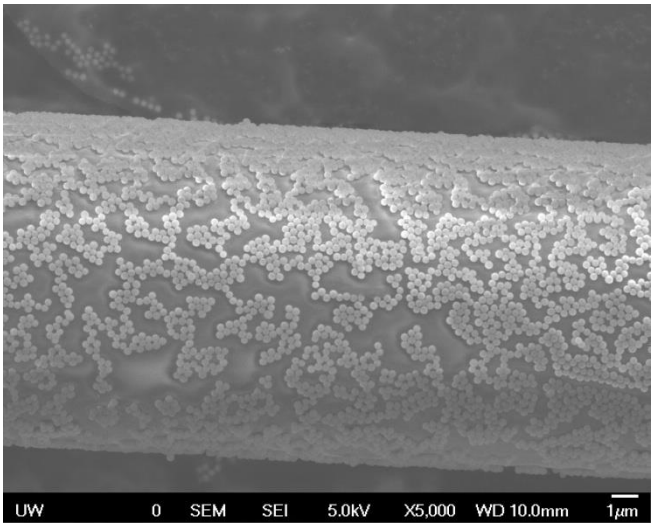

Figure B.12. A fiber dipped in a 0.1 vol% triaminosilane functionalized 250 nm silica suspension for 10 s at room temperature at pH = 4.58

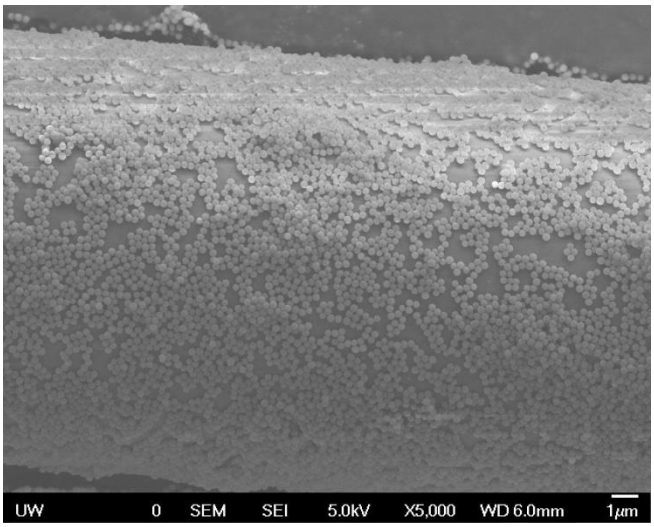

Figure B.13. A fiber dipped in a 0.1 vol% triamino functionalized (no drying step) silica suspension for 60 s at 85°C at pH = 3.79

Although surface coverage appeared good, as determined by SEM observations, none of the systems improved the IFSS, the results are shown in Fig. B.14.

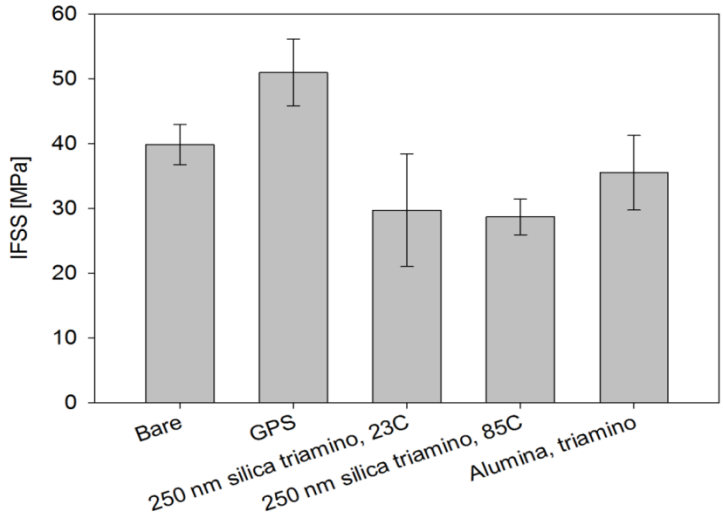

Figure B.14. The IFSS of E-glass fibers with no surface functionalization, functionalized with GPS, functionalized with GPS and coated with triaminosilane functionalized 250 nm silica, at room temperature and 85°C and functionalized with GPS and coated with triaminosilane functionalized alumina

It was concluded from work presented in Chapter 4 that particle size plays an important role in determining the IFSS in these systems. The 250 nm particles are too large to be well adhered to the fiber surface, reducing the interfacial strength. The alumina particles are smaller than the silica, and predictably they lead to a higher IFSS. Interestingly the triamino functionalized alumina reduced the IFSS, where the bare alumina increased the IFSS. This may be from variation in aggregation. Without any stabilizer the alumina nanoparticles tends to aggregate and depending on experimental variation such as the time between sonication and fiber coating and pH the level of aggregation may be different.

B.6 PEI functionalized 250 nm, 100 nm, 90 nm and 58 nm silica: synthesized silica and using a toughened matrix for the SFFTs

From the work done with polydisperse alumina and 250 nm silica it was seen that smaller particles gave a higher IFSS. To determine the size dependence varying sizes of silica particles were used. 250 nm and 100 nm were purchased, but 90 nm and 58 nm were synthesized using the Stöber process. PEI was used instead of aminosilane because it was postulated that covering the particles with a high molecular weight polymer would increase the likelihood of amine and epoxy achieving adequately small spatial separation to covalently bond. Moreover, the PEI would form a relatively soft polymer shell, increasing the contact area.

B.6.1 Methods

The modified Stöber process was used here, based on the work by Bogush et al (G. Bogush, M. Tracy, and C. Zukoski, *J. Non-Cryst. Solids*, vol. 104, no. 1, pp. 95–106, Aug. 1988.) Amorphous silica nanoparticles were synthesized by hydrolyzing tetraethylorthosilicate (TEOS) with excess water and ammonia in ethanol. By varying the concentrations of TEOS, water and ammonia the size of the silica particles can be controlled. In general, lower

concentrations of all reactants leads to smaller particles. The reactants were added to a round bottom flask and mixed at 25°C overnight.

Ammonia saturated ethanol was made by gently heating an ammonium hydroxide solution, passing the vapor through a 4°C chilled condenser, then through a bed of calcium sulfate to remove residual water, then finally bubbling the ammonia vapor through 200 proof ethanol. The resulting ammonia concentration was determined with acid titration and was typically about 3 M. The water concentration was determined with Karl Fisher titration and was typically about 0.01%.

The functionalization procedure here is similar to that described in section B.4, except 2,000 g/mol MW, 1,800 g/mol PEI was used instead of 60,000 g/mol to reduce flocculation of smaller particles.

Without using an ultracentrifuge it becomes difficult to centrifuge silica particles smaller than 100 nm out of the supernatant. Instead they were dialyzed using 28.6 mm diameter cellulose dialysis tubing, pore size of 4.8 nm (Fisher Science, Hanover Park, IL). Following synthesis or functionalization the solution was poured into dialysis tubing, and placed in a 4 l glass vessel filled with DI H_2O. DI H_2O was slowly flowed into the bottom of the vessel at ~ 1 l/h. At each step, the particles were dialyzed for at least 1 day.

The GPS functionalized fibers were submerged in 0.1 vol% colloidal suspensions at 85°C for 10 min.

It was observed that in the systems using 100 nm and smaller PEI functionalized particles cracks would form at fiber ends during SFFT. These cracks would often lead to specimen failure at relatively low strains, before the fiber was saturated with breaks. 5 wt% butadiene-acrylic

core-shell rubber (CSR) nanoparticles (MX156, Kaneka, Pasadena, TX) were mixed into the EP-828 and mPDA matrix improve the fracture toughness to prevent premature specimen failure, while still maintaining sufficient optical clarity and a high Young's modulus.

B.6.2 Results

By controlling the reactant concentration, it is possible to control the size of the particles made with the Stöber process. The particle sizes obtained, as measured with DLS, for various reactant concentrations are given in Table B.2. It was possible to make silica particles with diameters of around 100 nm and larger with little aggregation and monodisperse sizes. When particles smaller than 100 nm were made the reaction times became very long, on the order of several days, and macroscopic aggregates formed.

Table B.2. The DLS size of silica particles made via the Stöber processes, using various precursor concentrations

Sample	TEOS [M]	Ammonia [M]	Water [M]	Size [nm]
1	0.3	0.5	2	120
2	0.3	0.5	1	90
3	0.17	0.5	1	58

SEM micrographs of a fiber coated with 90 nm PEI functionalized particles is shown in Fig. B.15. Aggregation in both the 90 nm and 58 nm (not shown) particle systems was significant.

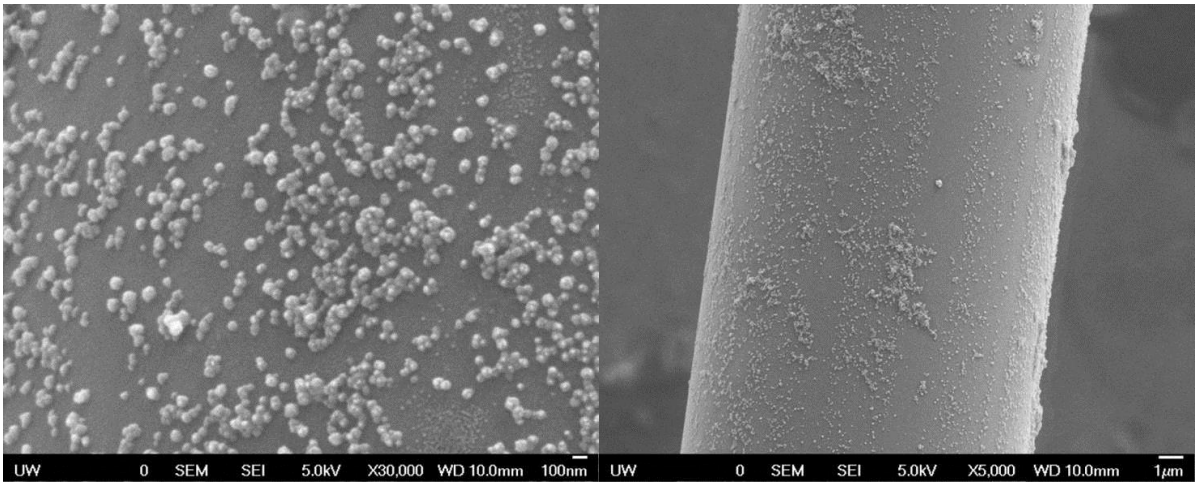

Figure B.15. A fiber coved in 90 nm PEI functionalized silica at two magnifications

There were significant challenges in applying sufficient strain to saturate the fiber with breaks during the SFFT. When a system with a high IFSS is subjected to the SFFT a matrix crack often forms at the fiber break, shown in Fig. B16b. These cracks would often grow rapidly with increasing strain, leading to specimen failure. To prevent these cracks from growing 5 wt% CSR nanoparticles, MX156, was added to toughen the matrix. The crack tip blunting is shown in Fig. B16c. Using 5 wt% MX156 had no significant change on IFSS, as determined by comparative studies done with and without MX156. Although these particles were found to be effective toughenners, their use was limited. It was found that reducing the strain rate was more effective at preventing premature failure.

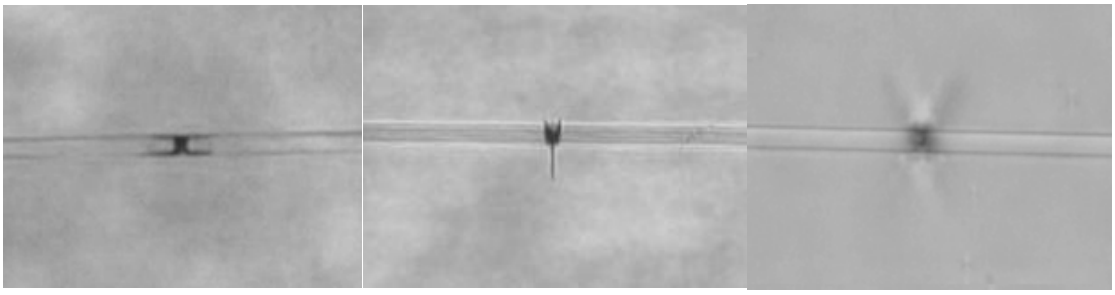

(a) (b) (c)

Figure B.16. Bright field micrograph following the SFFT of a) a fiber functionalized with GPS, b) a fiber functionalized with 90 nm PEI functionalized silica particle, and c) the same fiber as b) but with 5 wt% MX156

Decreasing the particle size the lead to increased IFSS. 100 nm and 90 nm improved the IFSS compared to not only the bare fiber, but also the GPS functionalized fiber; the results are summarized in Fig. B.17. A thorough discussion of an increase in IFSS with decreasing particle size can be found in Chapter 4. Summarizing, depositing particles on the surface can increase the surface roughness, increasing the mechanical interlock and surface area. However, these particles need to be well adhered to the surface to effectively transfer stress to the fiber. For large particles the ratio of contact area to height is small, preventing them being well adhered. Additionally, smaller particles have a larger ratio of PEI polymer to silica.

Not all systems have been studied with the CSR MX156, those that have are indicated with “CSR” in the tick label. Additionally, not all samples have been tested with the 2,000 g/mol MW PEI, those that have are labeled “low mw,” those labeled “high mw” were functionalized with the 750,000 g/mol MW PEI.

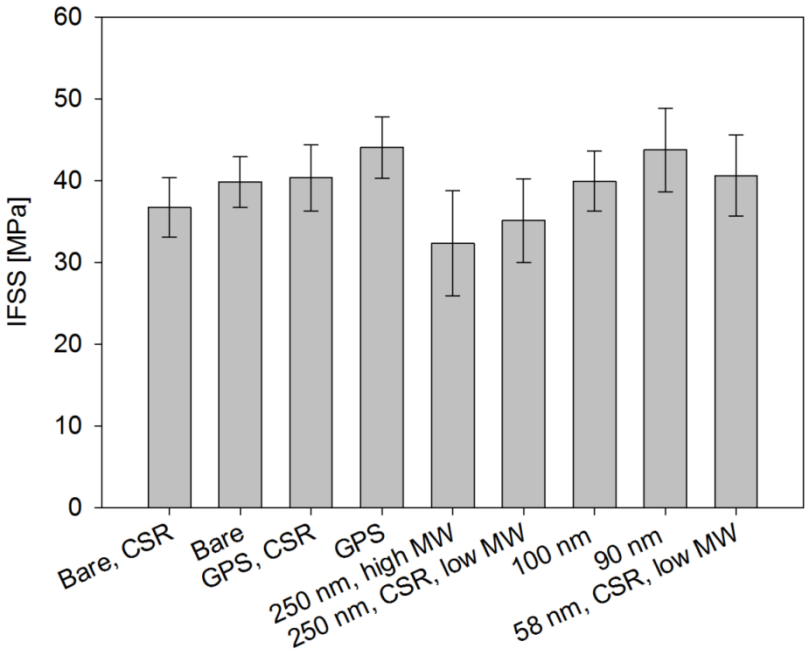

Figure B.17. The IFSS of fibers functionalized with GPS, 250 nm. 100 nm, 90 nm and 58 nm PEI functionalized silica particles

Based on these data, the addition of CSR particles and the molecular weight of PEI had no effect on the IFSS.

B.7 100 nm and 22 nm silica adhered using crosslinked GPS

Silanes that can hydrolyze to have multiple silanol groups can crosslink, and if an appropriate surface is present, such as silica, a thin film can form. Gao et al (Gao et al. 2011). took advantage of this phenomenon to adhere 22 nm silica particles (Ludox TMA, DuPont, Wilmington, DE) to E-glass fibers. They reported a DLS diameter of 22 nm for TMA Ludox, compared to a 26 nm diameter measured here. In a sizing containing film former, surfactant, antistatic agents, 0.5 wt% GPS, 0.5 wt% propyltrimethoxysilane (PTMO) and 1 wt% 22 nm silica they saw a 29% increase in IFSS, as measured with the microdroplet adhesion test, when

compared to a similar sizing that did not contain the 22 nm silica or the PTMO. Interesting, they also reported a 13% increase in IFSS in a fiber dip coated with 1 wt% 22 nm silica, with no adhesive.

Attempts were made to replicate the results using just GPS and silica, without any other sizing components, using the SFFT instead of the microdroplet adhesion test, but comparable increases in IFSS were not observed.

B.7.1 Methods

To functionalize desized E-glass fibers 1.0 wt% GPS and 1wt% 26 nm silica (Ludox TMA, DuPont, Wilmington, DE) were mixed in 75 vol% ethanol 25 vol% DI H_2O, the pH was reduced to 4.0 with glacial acetic acid and the mixture was mixed for 60 min, the fibers were then submerged for 15 min then removed and dried in the oven at 100°C for 1 hour. A similar fiber treatment was performed with 100 nm silica to compare the size effects.

B.7.2 Results

The effect of the fiber treatment on adhesion was determined by the SFFT. The improvement of IFSS using TMA and GPS as an adhesive was insignificant compared to the work of Gao et al; the results are summarized in Fig. B.18. Using 100 nm silica led to a decrease in IFSS, again confirming the importance of particle size. The quality of the fiber coatings would be dependent on the rate at which the fibers are withdrawn from the particle/GPS solution. Withdrawing the fibers more quickly would cause more of the solution to be subtended on the fiber, increasing the amount of GPS and particles. In this study the withdraw rate was not optimized and may be why the same improvements were not seen.

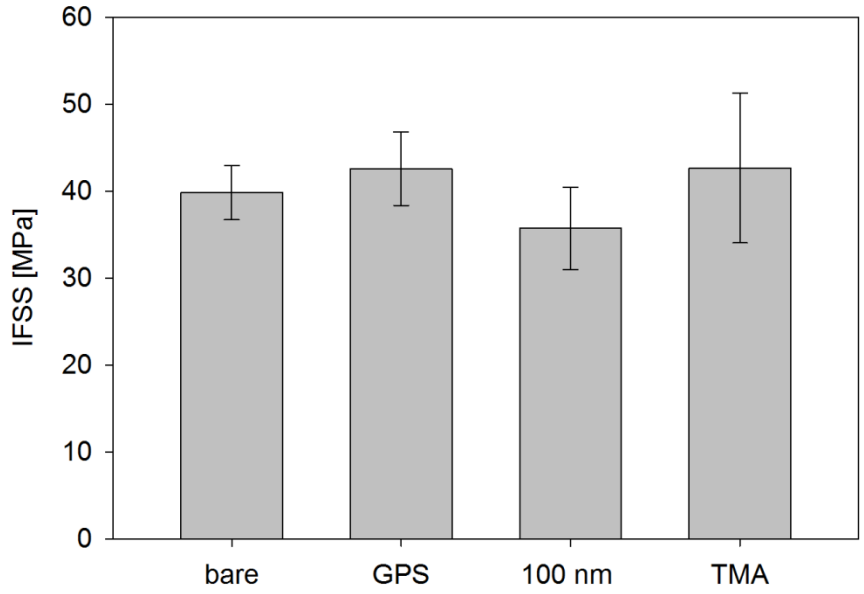

Figure B.18. The IFSS results of 100 nm and 26 nm silica adhered to E-glass using 1.0 wt% GPS as an adhesive.

B.8 PEI functionalized fibers with and without electrostatically deposited 26 nm silica

To determine if the chemical influence of PEI on IFSS without any particulate topography modifiers glass fibers were functionalized with PEI, and the IFSS was determined. SEM images were taken of this system to determine if PEI imparts any surface roughness. The PEI functionalized fibers were also coated with Ludox TMA 26 nm silica via electrostatic deposition.

B.8.1 Methods

Desized E-glass fibers were first functionalized with GPS, the procedure is outlined in section B.4, and were subsequently dipped in a 1 wt% PEI aqueous solution at 85°C and were rinsed with DI H_2O. Some specimens were then dipped in a 1 wt% silica solution, rinsed with DI H_2O, then dipped in the PEI solution again.

B.8.2 Results

Based on SEM observations, not shown here, the PEI did not impart any surface roughness on the fiber. The surfaces with electrostatically deposited silica showed regions of good, uniform surface coverage and other regions with large aggregates, shown in Fig. B.19a and B.19b, respectively.

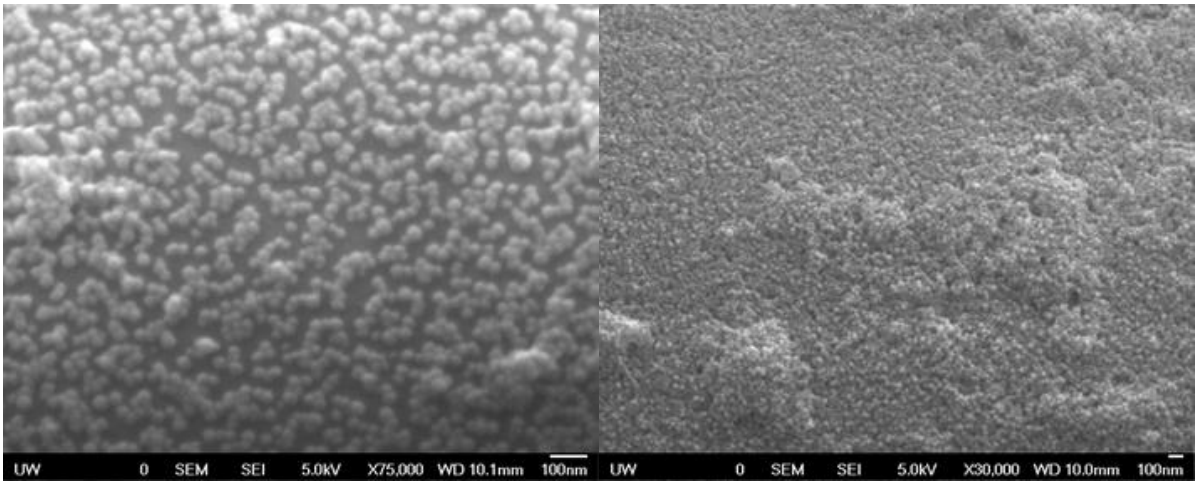

(a) (b)

Figure B.19. A PEI functionalized fiber with electrostatically deposited 26 nm silica showing a) good surface coverage and b) significant aggregates, note the difference in magnification

The PEI and PEI/TMA functionalized fibers had IFSS values similar to that of bare fibers. This is unexpected as PEI should covalently bond to both the GPS fiber surface and the matrix. Depositing the silica nanoparticles had little effect on the IFSS. The IFSS results are shown in Fig. B.20.

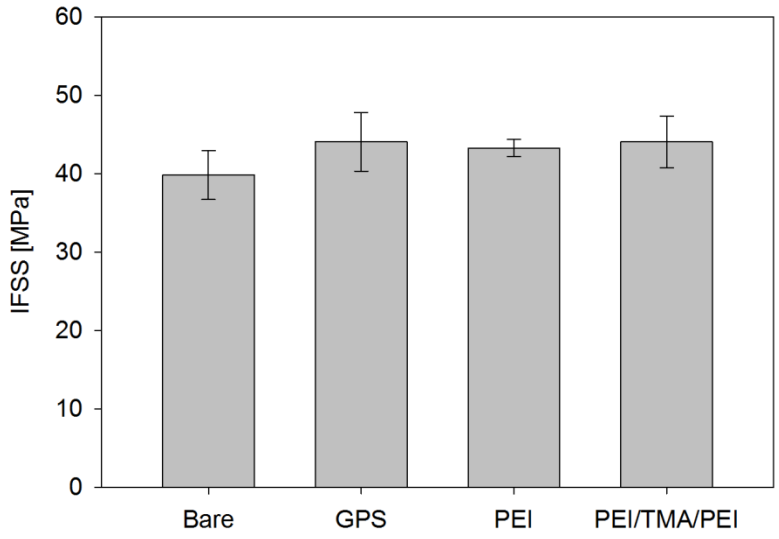

Figure B.20. IFSS of bare fibers, GPS fibers, fibers functionalized with PEI and fibers functionalized with PEI, coated with Ludox TMA and coated with another layer of PEI

Vita

Benjamin Rutz was born in Greene, New York and attended Greene Central High School. He entered the University of Rochester in Rochester, New York in 2004. For two semesters in 2006 he studied abroad at the University of Canterbury in Christchurch, New Zealand. In the summer of 2007 he participated in the National Science Foundation program "Research Experience for Undergraduates" at the University of Kansas, Lawrence, Kansas. He received his Bachelor of Science degree in Chemical Engineering from the University of Rochester in 2008. In 2008 he began his graduate studies in Chemical Engineering at the University of Washington, Seattle, Washington. In 2009 he joined the Professor John C. Berg research group, conducting research supported by Toray Composites (America). In 2010 he earned his Masters of Science in Chemical Engineering. During the summer of 2012 he was a research scientist intern at Toray Composites (America). He earned his Doctor of Philosophy degree in Chemical Engineering in 2014.